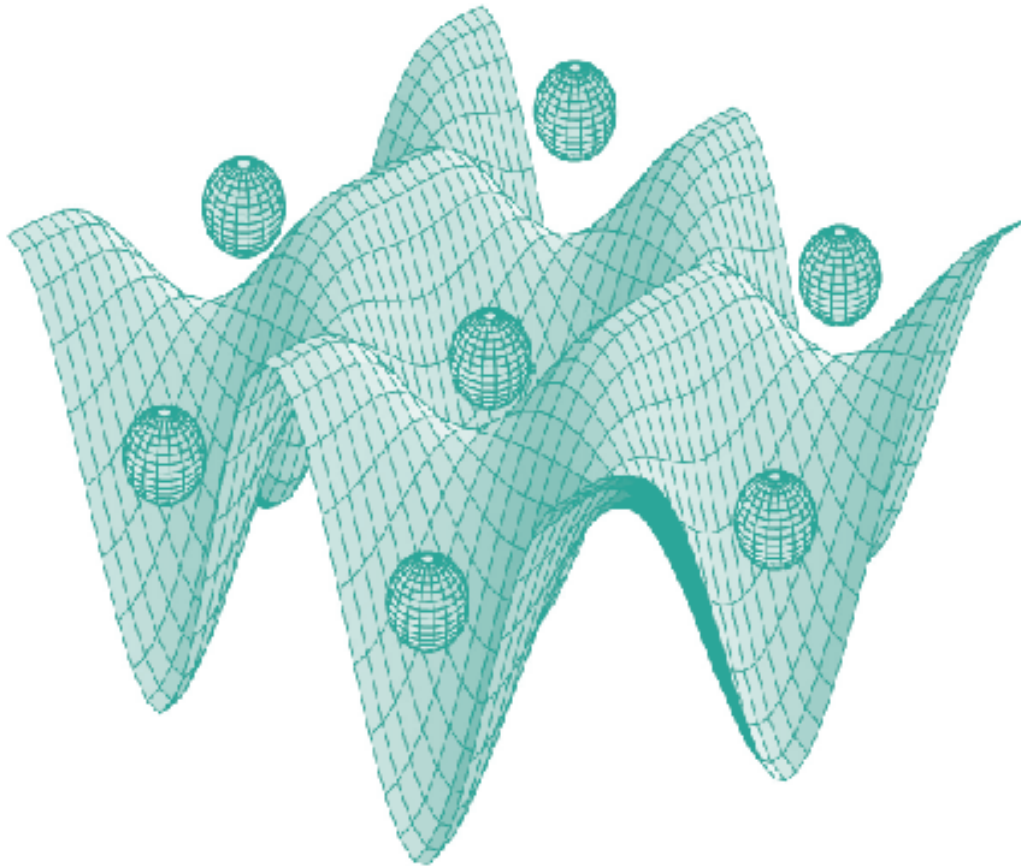




STUDIA UNIVERSITATIS
BABEȘ-BOLYAI



PHYSICA

1/2011

YEAR
MONTH
ISSUE

(LVI) 2011
JUNE
1

S T U D I A

UNIVERSITATIS BABEŞ–BOLYAI

PHYSICA

1

Desktop Editing Office: 51ST B.P. Hasdeu, Cluj-Napoca, Romania, Phone + 40 264-40.53.52

CUPRINS – CONTENT – SOMMAIRE – INHALT

DORINA CIOMOS, D. MARCONI, RADU REDAC, A. V. POP, Structural and Microstructural Characterization of Al and Gd doped ZnO Thin Films	3
C. CRĂCIUN, Comparison of the Potential Energy for Spherical Codes Used in CW EPR Powder Simulations	9
MARIA ILIUȚ, MONICA FOCȘAN, SIMION AȘTILEAN, Monitoring the Effects of Temperature on Milk by Fluorescence Spectroscopy of Riboflavin and Vitamin A.....	17
E. LASZLOFFI, I.P. FODOR, V. SIMON, Synthesis, Characterization and Protein Functionalisation of Calcinated Bioglasses.....	23
N. E. MIRCESCU, G. S. MILE, M. OLTEAN, V. CHIȘ, N. LEOPOLD, Surface-Enhanced Raman Detection of Melamine at Trace Level	31
A. NEDELUCU, V. CRISAN, The Ferromagnetic Onset in MnNi Alloy System ...	41

B. OPREA, T. RADU, S. SIMON, XPS Investigation of the Atomic Environment in Binary Boron-Bismuthate Glasses	47
A. SILAGHI, V. SIMON, Synthesis and Characterisation of the $55\text{SiO}_2 \cdot 41\text{CaO} \cdot 4\text{P}_2\text{O}_5$ Sol-Gel Derived Bioglass	57
V. SIMON, S. CAVALU, I. AKIN, O. YUCEL, G. GOLLER, XRD and FTIR Investigation of Zirconia-Toughened Alumina Composites.....	67
I. M. TAKACS, M. DRAGOTA, CRISTINA BISCHIN, LAURA BOLOJAN, G. DAMIAN, EPR Study of Molecular Oxygen Effect upon Nitroxide Radicals.....	73
L. UDRESCU, C. V. POP, T. STEFAN, M. TODICA, Observation of the Effects of UV Exposure of some PVA Membranes.....	81
R. VERES, C. CIUCE, V. SIMON, Synthesis and Characterization of Zinc Containing Phosphosilicate Glass-Ceramics	91

STRUCTURAL AND MICROSTRUCTURAL CHARACTERIZATION OF Al AND Gd DOPED ZnO THIN FILMS

DORINA CIOMOS¹, D. MARCONI¹,
RADU REDAC², A. V. POP¹

ABSTRACT. ZnO, Al-doped ZnO (Al:ZnO) and Gd/Al-doped ZnO (Gd:Al:ZnO) thin films were deposited on glass substrate using RF magnetron sputtering technique. The microstructure was studied by atomic force microscopy (AFM) and the crystallographic structure by X-Ray diffraction. XRD and AFM measurements shows that partial substitution of Zn with 2%Al and 2%(Al-Gd) lead to change of average grain size and surface morphology of thin films.

Keywords: ZnO thin films, RF magnetron sputtering, Structural properties

INTRODUCTION

Zinc oxide (ZnO) is one the most important II-VI semiconductor with large exciton binding energy ($E \sim 60$ meV), known for its many potential applications such as thin films transistors, window materials in solar cells, laser diodes, transparent conductive contacts, optoelectronic and piezoelectric applications and many others.[1,2] It has a wide and direct band gap ($E_g = 3.37$ eV) and good chemical and thermal stability. ZnO is found in nature in a material named zincite. Its color can vary from yellow to red, but due to its wide band gap, pure ZnO is colorless. [3] ZnO crystal has mainly a hexagonal wurtzite structure. It belongs to its space group $P6_3mc$ and the ratio of translational vectors $c/a = 1.633$ is really closed with the ratio for hexagonal cell. ZnO has an n-type electrical conductivity. ZnO is transparent to visible light. The undoped ZnO contains a various intrinsic defects which will influence the luminescence properties of ZnO. By introducing Al and Gd as dopants, it is expected that optical and electrical properties change.

Different techniques can be used in order to deposit thin films: chemical vapor deposition, metalorganic vapour phase epitaxy, electrodeposition, pulsed laser deposition, magnetron sputtering, sol-gel synthesis, spray pyrolysis, etc.[4-7] In this work, the RF sputtering technique deposition method will be used. On its advantage, it can count the increased purity, nanostructured features, homogeneity and rough surface. It is known that the quality of thin films depends on the conditions of growth. The characterization techniques include X-Ray diffraction and atomic force microscopy.

¹ Babes-Bolyai University, Physics Faculty, M. Kogalniceanu No. 1, 400084, Cluj-Napoca, Romania, dorina.ciomos@mail.ubbcluj.ro, Tel : +40264405300, Fax: +40264591906

² Aurel Vlaicu University, Faculty of Engineering, B-dul Revoluției nr. 77, 310130 Arad, România

EXPERIMENTAL

The ZnO, Al:ZnO and Gd:Al:ZnO thin films were deposited on glass substrates by RF magnetron sputtering technique using 99.999% pure ZnO. Ceramic targets with chemical formula $\text{Al}_{0.02}\text{Zn}_{0.98}\text{O}$ (sample AlZnO) and $\text{Gd}_{0.005}\text{Al}_{0.015}\text{Zn}_{0.98}\text{O}$ (sample GdAlZnO) were obtained by solid state reaction method. Films with thickness about 100 nm were deposited in an oxygen–argon atmosphere (O_2/Ar) on the glass substrate. The substrate temperature was 150°C .

The deposition pressure in the chamber was 2×10^{-2} mbar and the target-to-substrate distance was 40 mm.

The surface morphology was characterized by atomic force microscopy (AFM) in tapping mode using NT-MDT Ntegra Solaris atomic force microscope. X-ray diffraction (XRD) using a Bruker D8 diffractometer with CuK_α X-rays was done in order to determine the crystal structure of the deposited films.

RESULTS AND DISCUSSION

Figure 1 shows the XRD patterns of ZnO, AlZnO and GdAlZnO thin films. As shown in Fig. 1, the diffraction pattern shows only the maximum with Miller indices (002) indicating an epitaxial growths along c-axis (normal to substrate), with grains uniformly distributed, perpendicular to the substrate surface. Similar results were obtained from ZnO, AlZnO and GdZnO thin films, [8-14].

Because the position of (002) diffraction peak values for ZnO and ZnAlO samples is almost the same ($2\theta=34.109$, and 34.195 , respectively), the lattice constant c of the samples calculated by Bragg formula is almost unchanged ($c=0.549$ and 0.548 nm).

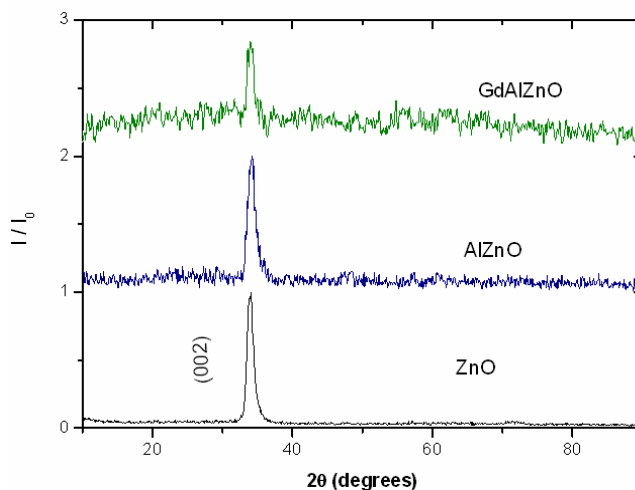


Fig. 1. XRD patterns of ZnO, AlZnO and GdAlZnO thin films.

The main effect of Zn substitution by 2%Al is the change of linewidth of (002) diffraction peak, suggesting changes in mean value of the grains size.[15] The crystallite sizes of the films were calculated using the Scherrer equation:

$$D = \frac{0,9\lambda}{B \cos \theta}$$

where λ , θ , and B are the X-ray wavelength ($\lambda_{\text{CuK}\alpha 1} = 0,15406$ nm), diffraction angle and FWHM (full width at half maximum) of the diffraction (002) peak.

In order to determine more precisely the position and FWHM of the linewidth, in fig. 2 the Lorentz fit of (002) peak for AlZnO film was performed. By using a corrected value for B (the instrumental broadening was deduced from the measured FWHM) and the position of maximum, the crystallite size D was obtained.

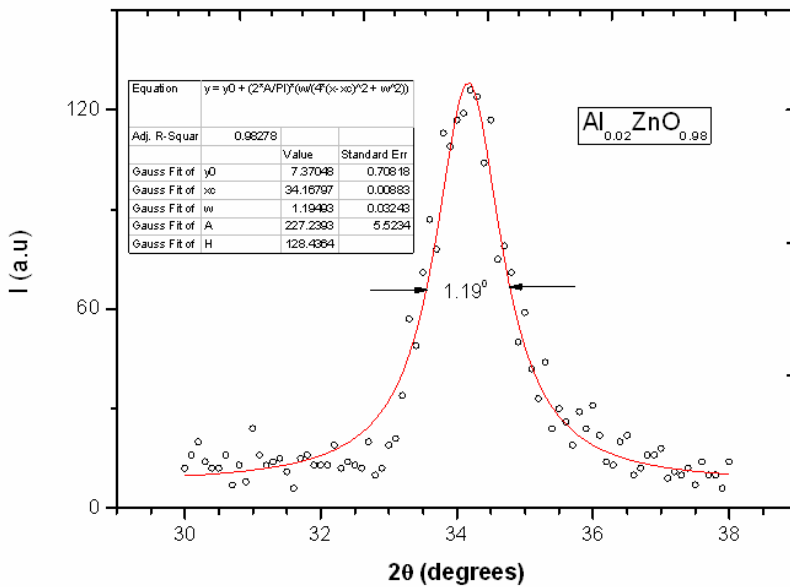


Fig.2. Lorentz fit of (002) peak for AlZnO film

The average crystallite size for ZnO film is around 12 nm. The partial substitution of Zn with 2%Al lead to the decrease of crystallite size around 9 nm. The small quantity of Gd in (GdAl)ZnO film lead only a small increase of crystallite size to 10 nm. The decrease of crystallite size reinforced the decrease of film cristalinity. This behaviour may be considered to be due to the moderate quantity of Al atoms that can exist at interstitial sites and Al together with Zn atoms share oxygen atoms. The preparation conditions determine the grain size and the crystallinity of the films, which reflects on the film physical properties.

Figure 3 shows that the surface morphology measured by AFM reveals a granular structure of films.

AFM characterization of the film surfaces revealed that grain size decrease after the partial substitution of Zn with Al and Al+Gd. For ZnO film, the surface morphology evidenced a not regulated shape of the grain and dimensional unhomogeneity as shown in figure 3a).

Films surfaces for AlZnO and GdAlZnO thin films revealed a similar morphology for both samples with similar grain size. It also shows the presence of columnar morphologies with increased roughness for 2% Al thin films and a decreased roughness when is then doped with Gd. The overall surfaces of AlZnO and GdAlZnO films are formed by more homogeneous grains compared to the one of ZnO.[16]

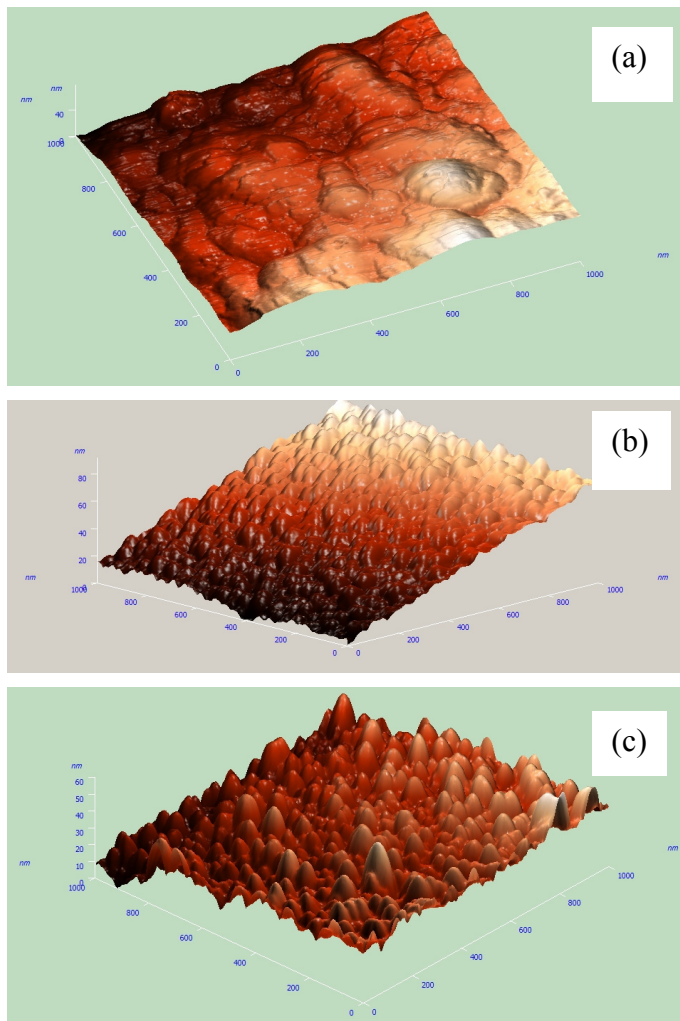


Fig. 3 AFM images of thin films: (a) pure ZnO, (b) AlZnO and (c) GdAlZnO.

CONCLUSIONS

ZnO, AlZnO and GdAlZnO thin films were deposited on a glass substrate using RF magnetron sputtering method. By substituting Zn with 2%Al, XRD showed an increase in linewidth of (002) diffraction peak and by doping this film with Gd, a decrease in the linewidth was observed. These changes suggested that there is a difference in the mean value of the grains size of these thin films from 12 nm for un-doped ZnO to 9 nm for Al doped ZnO and to 10 nm respectively for Zn doped with Al and Gd.

AFM characterization for the films deposited from a ceramic target suggested a morphology with grain agglomerations, which is influenced by the Al and Gd substitutions.

ACKNOWLEDGEMENTS

One of the authors (Dorina Ciomos) wishes to thank for the financial support provided from programs co-financed by The Sectoral Operational Programme Human Resources Development, Contract POSDRU 88/1.5/S/60185– „Doctoral and postdoctoral programs to support research".

REFERENCES

1. V.S. Khomchenko, T.G. Kryshab, A.K. Savin, L.V. Zavyalova, N.N. Roshchina, V.E. Rodionov, O.S. Lytvyn, V.I. Kushnirenko, V.B. Khachatryan, J.A. Andraca-Adame, *Superlattice Microstructures* **42**, (2007), 94-98
2. H.W. Lee, D.G. Khoi, K.B. Shim, Y.J. Oh, *Journal of Ceramic Processing Research* **6**, (2005), 880
3. C. Lingshirn, *ChemPhysChem*, **8**, (2007), 782-803
4. Hu J, Gordan R G, *Journal of Applied Physics* **72**, (1992), 5381
5. Reddy K T R, Gopaldaswamy H, Reddy P J and Miles R W, *J. Cryst. Growth* **210**, (2000), 516
6. Sato H, Minami T, Takata S, Miyata T, Ishii M, *Thin Solid Films* **236**, (1993), 14
7. Ma Jin, Ji Feng, De-Heng Z, Ma Hong-Li, Li Shu-Ying, *Thin Solid Films* **357**, (1999), 98
8. S. Flickyngerova, J. Skrinjarova, M. Netrvalova, J. Kovac Jr., I. Novotny, P. Sutta, V. Tvarozek, *Applied Surface Science* **256** (2010), 5606–5609
9. Shou-Yi Kuo, Kou-Chen Liu, Fang-I Lai, Jui-Fu Yang, Wei-Chun Chen, Ming-Yang Hsieh, Hsin-I Lin, Woei-Tyng Lin, *Microelectronics Reliability* **50** (2010), 730–733
10. W.W. Zhong, F.M. Liu, L.G. Cai, C.C. Zhou, P. Ding, H. Zhang, *Journal of Alloys and Compounds* **499** (2010), 265–268
11. L.M. Wong, S.J. Wang, W.K. Chim, *Thin Solid Films*, **518**, (2010), e93–e97

12. Jong-Pil Kim, Jong-Seong Bae, Tae-Eun Hong, Mi-Sook Won, Jang-Hee Yoon, Byoung-Seob Lee, Haeng-Jung Lee, *Thin Solid Films* **518** (2010), 6179–6183
13. Se Hun Park, Ji Bong Park, Pung Keun Song, Article in press, *Current Applied Physics*, (2010)
14. Viorica Musat, Elvira Fortunato, The annals of “Dunarea de jos” University of Galati, fascicle iX, *Metallurgy and materials science* N0. 2 – 2007, ISSN 1453 – 083X
15. J.J.Ding, S.Y.Ma, H.X.Chen,X.F.Shi, T.T.Zhou, L.M.Mao, *Physica B* **404** (2009), 2439–2443
16. M. Sucheá, S. Christoulakis, N. Katsarakis, T. Kitsopoulos, G. Kiriakidis, *Thin Solid Films* **515** (2007), 6562–6566

COMPARISON OF THE POTENTIAL ENERGY FOR SPHERICAL CODES USED IN CW EPR POWDER SIMULATIONS

C. CRĂCIUN*

ABSTRACT. The uniformity of some spherical codes used for the simulation of CW EPR powder spectra is assessed from the potential energy point of view. The Igloo, SOPHE and EasySpin analytically generated grids and the Repulsion and SCVT irregular spherical codes are compared using the Riesz s -energy and the Korevaar's modified Coulomb energy, if equal electric charges are placed at the points of the grids. Weighted forms of the energies, based on the areas of the Voronoi cells generated by the points spread on the unit sphere, are compared.

Keywords: CW EPR, simulation, powder spectra, spherical codes, Riesz s -energy

INTRODUCTION

The simulated continuous-wave electron paramagnetic resonance (CW EPR) spectra of the polycrystalline powders are computed as weighted sums of the randomly oriented single-crystal spectra. The orientation of the static magnetic field in the molecular reference frames of the single-crystals is modeled using a set of points distributed on the unit sphere [1]. The points of the orientation grids may be distributed either regularly, based on analytical expressions, or irregularly. Regular grids usually require a smaller number of points for the simulation of CW EPR powder spectra, due to the possibility of interpolating their spectral properties. From the category of regular grids, special attention have received the triangular type spherical codes, which divide the unit sphere in triangles (ASG [2], SOPHE [3], EasySpin [4]) and the spiral type grids [5], with better quality figures than the triangular grids but harder to interpolate. The irregular grids may be generated by distributing the points randomly on the unit sphere or by minimizing an energy-like function associated with the set of points [6]. Usually these grids have uniformity quality figures better than the regular grids, but require a higher number of points and are less suitable for interpolation [6,7].

The homogeneity of the spherical codes has been assessed based on the quality parameters related to the properties (areas, shape distortion) of the Voronoi cells defined by the points on the unit sphere, as well as based on the electrostatic potential energy. The energy criterion proposed in [6], using a $(d_a)^{-2}$ dependence of the energy on the surface point-to-point distance d_a , leads to similar results for the most used spherical codes for the simulation of magnetic resonance spectra.

* Babeş-Bolyai University, Faculty of Physics, 1 Kogălniceanu str., 400084 Cluj-Napoca, Romania

The present paper assesses different potential energy expressions as quality criteria for the grids used in modeling the CW EPR powder spectra. For this aim, the regular Igloo [8], SOPHE [3] and EasySpin [4,6] grids are compared energetically with the Repulsion [13] and SCVT (Spherical Centroidal Voronoi Tessellation) [9,10] irregular spherical codes. The energies are calculated for different forms of the Riesz, respectively Korevaar's modified Coulomb potentials.

COMPUTATIONAL DETAILS

Details regarding the generation of the spherical codes (θ, ϕ) are provided in the reference [7]. The Igloo regular grids [8] were obtained on the entire unit sphere based on the analytical expressions (1) [6]. The SOPHE codes [3] were generated by applying symmetry operations on the points of the first octant of the sphere given by (2). The EasySpin grids [4,6] were computed by averaging the three SOPHE spherical codes constructed around the x, y and z axes of the coordinate system.

$$\text{Igloo:} \quad \theta_{ij} = \frac{i}{n-1} \pi, \quad \phi_{ij} = \frac{j}{m_i} 2\pi, \quad 0 \leq i \leq n-1, 0 \leq j \leq m_i - 1 \quad (1)$$

$$m_i = \lceil 2(n-1)\sin\theta_i + 1/2 \rceil$$

$$\text{SOPHE:} \quad \theta_{ij} = \frac{i}{n} \cdot \frac{\pi}{2}, \quad \phi_{ij} = \frac{j}{i} \cdot \frac{\pi}{2}, \quad 0 \leq i \leq n, 0 \leq j \leq i \quad (2)$$

n - is the number of θ intervals in the $[0, \pi/2]$ range.

The energy minimization codes have been computed using the FORTRAN90 SCVT library (J. Burkardt) [9], respectively the Repulsion program, available in the SIMPSON package [11]. The Voronoi diagrams for different types of grids were produced using the STRIPACK package (R.J. Renka) [9,12] and were represented graphically on the unit sphere with the SXYZ_VORONOI program (J. Burkardt) [9]. Figure 1 presents the distribution of ~250 points on the unit sphere, obtained using the Igloo, SOPHE and SCVT methods.

RESULTS AND DISCUSSION

From currently compared grids from the potential energy point of view, only the irregular Repulsion and SCVT spherical codes are generated using energy minimization criteria.

The Repulsion grid [13] is obtained by adjusting the positions of a set of equal electric charges on the surface of the unit sphere, in order to minimize a Coulomb type electrostatic potential energy. At equilibrium, the surface distance d_a between the charges is maximal. The change of the electric repulsive forces ($\sim (d_a)^{-p}$, $1 \leq p \leq 3$) leads to similar grids [13].

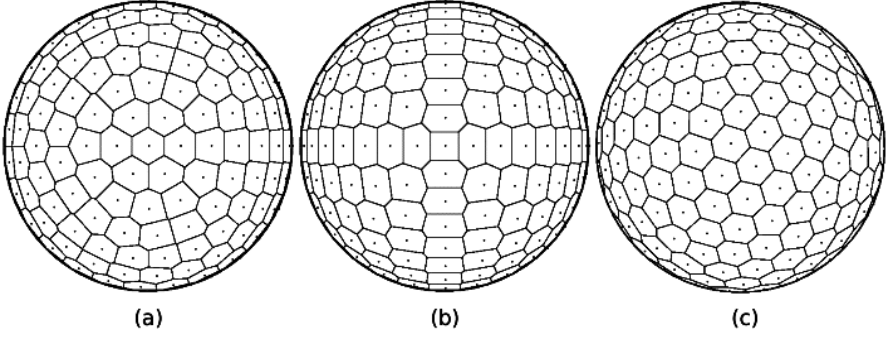


Fig. 1. The upper hemisphere of the grids: (a) Igloo for 248 points, (b) SOPHE for 258 points, (c) SCVT for 258 points

The SCVT method [10,14] generates points uniformly distributed on the surface of the unit sphere that coincide with the centroids (centers of mass) of their corresponding Voronoi cells. If $\{\mathbf{z}_i\}_{i=1}^N$ is the set of points of the SCVT code and $\{V_i\}_{i=1}^N$ are the surrounding Voronoi regions, the energy of the tessellation is defined by the variance [14]:

$$E(\{\mathbf{z}_i\}_{i=1}^N, \{V_i\}_{i=1}^N) = \sum_{i=1}^N \int_{V_i} \rho(\mathbf{z}) |\mathbf{z} - \mathbf{z}_i|^2 d\mathbf{z} \quad (3)$$

where $|\cdot|$ is the Euclidean norm and $\rho(\mathbf{z})$ is the distribution density function.

In order to establish if there is a potential energy form that could be used as a quality criterion for the spherical codes involved in the simulation of CW EPR powder spectra, the following aspects have been considered:

- the compared energies correspond to the Riesz's [15], respectively Korevaar's modified Coulomb [16] potentials, for different values of their parameters.
- the distance between the points of the grids is either the Euclidean distance or the surface (geodesic) distance, measured as the length of the arc connecting the points on the surface of the unit sphere.
- the electric charges associated with the points of the grids are either equal or proportional to the areas of the Voronoi cells surrounding the points.

Following the notations from [6], the Euclidean distance between the 3D points \mathbf{z}_i and \mathbf{z}_j of a spherical code is:

$$(d_{ij})_E = |\mathbf{z}_i - \mathbf{z}_j| \quad (4)$$

The point-to-point surface distance on the unit sphere equals the angle between the vectors from the center of the sphere to the points [17]:

$$(d_{ij})_a = \cos^{-1}(\mathbf{z}_i \cdot \mathbf{z}_j) \quad (5)$$

The relation between the Euclidean and surface (geodesic) distance is:

$$(d_{ij})_E = \sqrt{2 [1 - \cos(d_{ij})_a]} \quad (6)$$

1. The potential energies of the spherical codes

1.1 The Riesz s-energy

If S^d represents the unit sphere in the Euclidean space \mathbb{R}^{d+1} ($d \geq 1$) and $\omega_N = \{\mathbf{z}_1, \dots, \mathbf{z}_N\}$ is a collection of N distinct points ($N \geq 2$) on the surface of S^d , the discrete Riesz s -energy is given by [15]:

$$E_s(\omega_N) = \begin{cases} \sum_{i=1}^N \sum_{j=1, j \neq i}^N \frac{1}{(d_{ij})^s} & s > 0 \\ \sum_{i=1}^N \sum_{j=1, j \neq i}^N \log\left(\frac{1}{d_{ij}}\right) & s = 0 \end{cases} \quad (7)$$

where d_{ij} is the Euclidean or the surface distance between the \mathbf{z}_i and \mathbf{z}_j points.

The normalized energy is defined as [17]:

$$\varepsilon_s(\omega_N) = \frac{E_s(\omega_N)}{N^2} \quad (8)$$

The minimization of the energy for the case $s = 0$ (eq. 7) is equivalent to maximizing the product of the distances between the points of the grid, $\prod_{i \neq j} |\mathbf{z}_i - \mathbf{z}_j|$ [16].

The case $s = 1$ (eq. 7) corresponds to equal electric charges interacting through a Coulomb potential [16]. When $s \rightarrow \infty$, the energy is dominated by the interaction between the closest points, and corresponds to the best packing problem on the sphere [18].

The weighted Riesz s -energy for the case $s > 0$ is defined by [18]:

$$E_s(\omega_N) = \sum_{i=1}^N \sum_{j=1, j \neq i}^N \frac{w(\mathbf{z}_i, \mathbf{z}_j)}{(d_{ij})^s} \quad (9)$$

where $w(\mathbf{z}_i, \mathbf{z}_j)$ is the weight function. The weighted minimal Riesz energy problem has been addressed previously in order to obtain sets of points distributed on the unit sphere according to a specified density function [18].

Owing to the fact that the spherical codes used for the simulation of CW EPR powder spectra are not all uniform, one possibility is to consider that the electric charges associated with the points of the grids are proportional to the areas of their Voronoi cells. Therefore, for a total charge on the unit sphere proportional to the number of points of the grid N , the weight function from eq. 9 becomes:

$$w(\mathbf{z}_i, \mathbf{z}_j) = \rho_e(\mathbf{z}_i) \cdot \rho_e(\mathbf{z}_j) \quad (10)$$

where $\rho_e(\mathbf{z}_i)$, $1 \leq i \leq N$, are the electric charge densities at the points \mathbf{z}_i :

$$\rho_e(\mathbf{z}_i) = \frac{\text{area}(V_i)}{\text{area}(S^2)} \cdot N \quad (11)$$

$\text{area}(V_i)$ is the area of the Voronoi cell V_i of the point \mathbf{z}_i and $\text{area}(S^2)$ is the area of the 3D unit sphere.

1.2 The Korevaar's modified Coulomb energy

Korevaar proposed the following modified form of the Coulomb energy [16]:

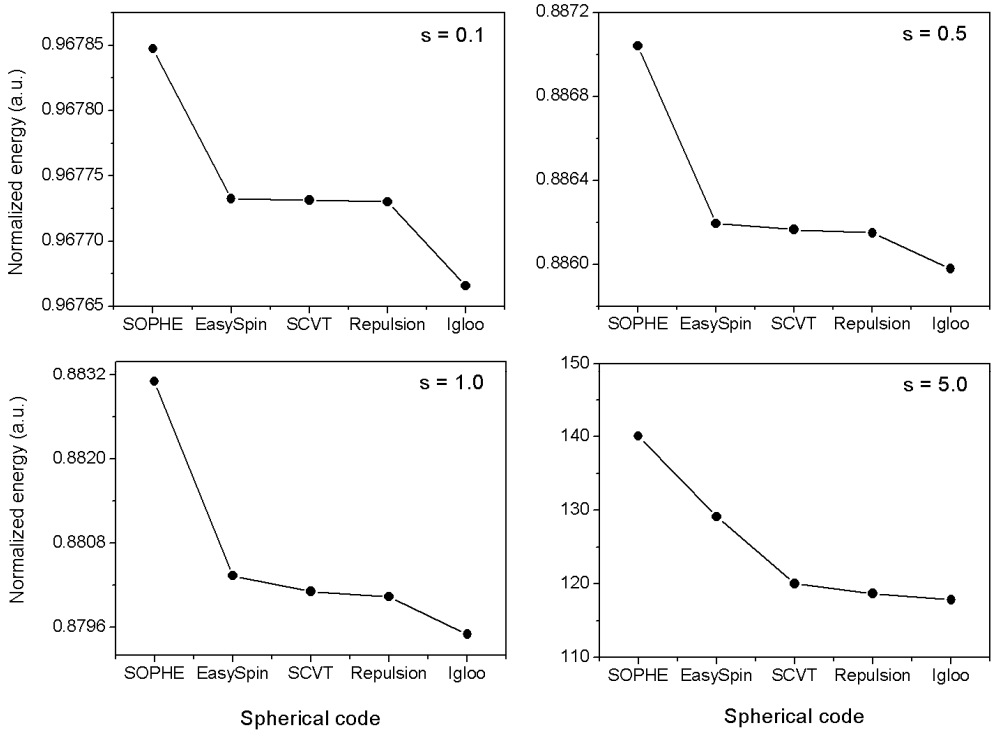


Fig. 2. Normalized Riesz s -energy for different values of the s parameter. Grid size: 562 points (Igloo), 578 points (SOPHE, EasySpin, Repulsion, SCVT). The point-to-point distance was computed as the surface distance on the unit sphere.

$$E_r(\omega_N) = \sum_{i=1}^N \sum_{j=1, j \neq i}^N \frac{1}{|\mathbf{z}_i - r \mathbf{z}_j|} \quad (12)$$

where r is a parameter belonging to the $(0,1)$ interval.

2. Comparison of the potential energies of the grids used in CW EPR

The energies of the spherical codes discussed in this paper have the same relative behavior regardless of the type of the point-to-point distance (Euclidean or geodesic) used in the computation (eq. 4-6).

2.1 Normalized Riesz s-energy

Figure 2 presents the normalized Riesz energies computed with the relations (7-8) for grids with 562-578 points. While the s exponential parameter increases from 0.1 to 5.0, the relative ratios:

$$\frac{\varepsilon_s [\text{EasySpin}] - \varepsilon_s [\text{Repulsion}]}{\varepsilon_s [\text{SOPHE}] - \varepsilon_s [\text{Iglloo}]} \quad \text{and} \quad \frac{\varepsilon_s [\text{SCVT}] - \varepsilon_s [\text{Repulsion}]}{\varepsilon_s [\text{SOPHE}] - \varepsilon_s [\text{Iglloo}]}$$

increase by ~ 35 , respectively ~ 7 times, which enables better separation between the energies of the spherical codes.

2.2 Coulomb energy

(a) Dependence on the charge density

If the equal electric charges in the Coulomb potential (Riesz s -energy for $s = 1$) (eq. 7) are replaced by a uniform density distributed on the unit sphere, the charges at the points of the grid may be considered proportional to the areas of Voronoi cells around these points (eq. 9-11). The values of the normalized energies are presented in Figure 3. Their relative behavior (for Euclidean as well as surface point-to-point distances) preserves when considering spherical codes with the size in the 200-1100 range.

(b) The influence of the size of the grid

The increase of the number of points in the grids (for $N > 200$) determines the decrease of the energies of the spherical codes relative to the Iglloo grid. Therefore, for ~ 1000 points, the energy minimization grids (Repulsion, SCVT) and the regular EasySpin spherical code have the smallest energies.

2.3 Logarithmic and Korevaar's energies

The use of the logarithmic (Riesz s -energy for $s = 0$) (eq. 7) or Korevaar's modified Coulomb energy ($r = 0.2, 0.4, 0.8$) (eq. 12) does not differentiate between the EasySpin, Repulsion and SCVT spherical codes,

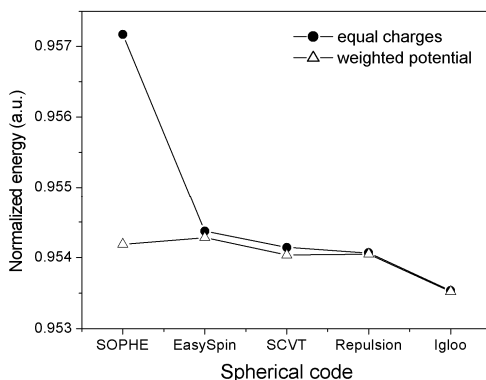


Fig. 3. Normalized Riesz s -energy ($s = 1$) for equal electric charges, respectively for a weighted Coulomb potential ($N = 562$ - 578 points, Euclidean point-to-point distance)

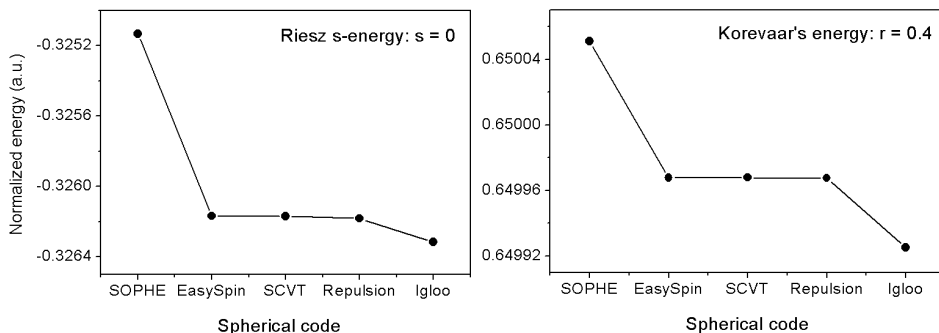


Fig. 4. Normalized Riesz s -energy ($s = 0$) and Korevaar's energy ($r = 0.4$) (Igloo with 562 points, the other grids with 578 points; geodesic point-to-point distance)

as illustrated in Figure 4. When the r factor in the normalized Korevaar's energy increases from 0.2 to 0.8, the relative ratio:

$$\frac{\epsilon_s [\text{EasySpin, Repulsion, SCVT}] - \epsilon_s [\text{Igloo}]}{\epsilon_s [\text{SOPHE}] - \epsilon_s [\text{Igloo}]}$$

decreases about five times.

2.4 The energy of the spherical codes and the simulation noise in CW EPR spectra

Previous studies regarding the use of the presently investigated spherical codes for the simulation of CW EPR powder spectra have shown the following order of the grids with respect to the signal to simulation noise ratio [7]:

$$\text{EasySpin} > \text{Repulsion} \geq \text{SCVT} > \text{SOPHE} > \text{Igloo}$$

The energy values computed for the spherical codes show the same relative behavior for the EasySpin, Repulsion and SCVT grids when changing the form and the parameters of the point-to-point interaction potential. Better energy separation within this group of grids is obtained when considering Riesz s -energies with higher values of the s parameter, which correspond to shorter-range point-to-point interactions.

CONCLUSION

The regular Igloo, SOPHE and EasySpin and the irregular Repulsion and SCVT spherical codes, used for the simulation of CW EPR powder spectra, have been compared energetically by considering Riesz, respectively Korevaar's modified Coulomb potentials. The EasySpin, Repulsion and SCVT spherical codes tend to behave similarly for different potential energies. However, the Riesz s -energy with higher values of the s parameter better differentiate energetically these spherical codes.

ACKNOWLEDGMENTS

The author is grateful to Lector Lavinia Cociu, Faculty of Physics, Babeş-Bolyai University, for introducing to a program of simulation of EPR spectra.

REFERENCES

1. Ponti, *J. Magn. Reson.*, 138, 288 (1999).
2. D.W. Alderman, M.S. Solum, D.M. Grant, *J. Chem. Phys.*, 84, 3717 (1986).
3. D. Wang, G.R. Hanson, *J. Magn. Reson. A*, 117, 1 (1995).
4. S. Stoll, A. Schweiger, *J. Magn. Reson.*, 178, 42 (2006).
5. M.J. Mombourquette, J.A. Weil, *J. Magn. Reson.*, 99, 37 (1992).
6. S. Stoll, Ph.D. Thesis, ETH Zurich, Switzerland, 2003.
7. C. Craciun, *Appl. Magn. Reson.*, 38, 279 (2010).
8. M.J. Nilges, Ph.D. Thesis, University of Illinois, Urbana, Illinois, 1979.
9. http://people.sc.fsu.edu/~burkardt/f_src/f_src.html
10. Q. Du, V. Faber, M. Gunzburger, *SIAM Rev.*, 41, 637 (1999).
11. M. Bak, J.T. Rasmussen, N.C. Nielsen, *J. Magn. Reson.*, 147, 296 (2000).
12. R. Renka, *ACM Trans. Math. Soft.*, 23, 416 (1997).
13. M. Bak, N.C. Nielsen, *J. Magn. Reson.*, 125, 181 (1997).
14. J. Burkardt, M. Gunzburger, J. Peterson, R. Brannon, Technical Report: SAND2002-0099, Sandia National Laboratories, February 2002.
15. A.B.J. Kuijlaars, E.B. Saff, X. Sun, *Journal Comp. & Applied Math.*, 199(1), 172 (2007).
16. E.B. Saff, A.B.J. Kuijlaars, *The Mathematical Intelligencer*, 19(1), 5 (1997).
17. P. Leopardi, Ph.D. Thesis, University of New South Wales, 2007.
18. S.V. Borodachov, D.P. Hardin, E.B. Saff, *Trans. Amer. Math. Soc.*, 360, 1559 (2008).

MONITORING THE EFFECTS OF TEMPERATURE ON MILK BY FLUORESCENCE SPECTROSCOPY OF RIBOFLAVIN AND VITAMIN A

MARIA ILIUȚ^{*1}, MONICA FOCȘAN¹, SIMION AȘTILEAN¹

ABSTRACT. In this study we investigated the structural and chemical changes induced by temperature in UHT processed milk by monitoring the fluorescence of riboflavin and vitamin A. Despite the thermal stability of pure riboflavin and vitamin A in different solvents, in milk we measured important spectroscopic changes as a consequence of the complex environment in which the vitamins are located. We established that Riboflavin was degraded irreversibly and its degradation might be initiated by light and catalyzed by the environment under the action of temperature. We also found that temperature can induce conformational changes in Vitamin A and its close vicinity environment (triglycerides).

Keywords: Fluorescence spectroscopy, Milk, Riboflavin, Vitamin A.

INTRODUCTION

Milk is the only source of nutrients for the neonatal, providing macronutrients, water, vitamins and minerals to support the growth [1]. Thus it is important to consider the influence of processing and the effects of various external factors on the vitamins and nutrients of milk and dairy products. Although milk is a very complex fluid, it is a very heat-stable system, which allows it to be subjected to severe heat treatments with relatively minor changes [1]. It is well known that dairy products content fluorescence components which are extremely sensitive to their environment, and therefore fluorescence spectroscopy is ideal to monitor induced structural changes of different food products. Visible/UV light can be absorbed by a variety of molecular structures and therefore has the potential for the most severe effects [2]: degradation of proteins, vitamins and lipids, as well as formation of toxic compounds and off-flavors. Milk and milk products are very sensitive to light oxidation due to the presence of riboflavin (aqueous soluble vitamin), a strong photosensitizer [3], the most light-absorbing constituent of milk [2]. Riboflavin is stable in the presence of oxygen, heat and at acid pH, while

* E-mail: mariailiut@yahoo.com

¹ Babes-Bolyai University, Faculty of Physics and Institute for Interdisciplinary Research in Bio-Nano-science, Nanobiophotonics Center, Treboniu Laurian 42, 400271, Cluj-Napoca, Romania
Tel.: +40 264454554/119

vitamin A (fat-soluble vitamin generally found in milk as retinol and esters) is sensitive to oxidation and exposure to light and relatively stable to heat [1].

EXPERIMENTAL SECTION

Riboflavin ($C_{17}H_{20}N_4O_6$) was purchased from Aldrich and UHT-milk 3,5% fat was purchased from commercial sources.

The absorption spectrum of pure Riboflavin in water ($10^{-4}M$) was recorded using a Jasco V-670 UV-Vis-NIR spectrophotometer. All fluorescence measurements were performed using a Jasco LP-6500 spectrofluorimeter coupled with a Jasco ADP-303T temperature controller ($-10 - 110^{\circ}C$). The emission spectra of riboflavin in milk were recorded with the excitation wavelengths set at 445 nm. The excitation spectra of vitamin A were recorded by setting emission wavelength at 410 nm (according to literature). The emission spectra of vitamin A in milk were measured with excitation wavelength at 322 nm. Slit widths of 3 nm and quartz cells with 1.0 cm path length were used for all measurements.

RESULTS AND DISCUSSION

Riboflavin in water exhibits three absorption bands in the UV-Vis wavelength region, at 270, 375 and 445 nm and only one emission band centered at 530 nm (see Fig.1).

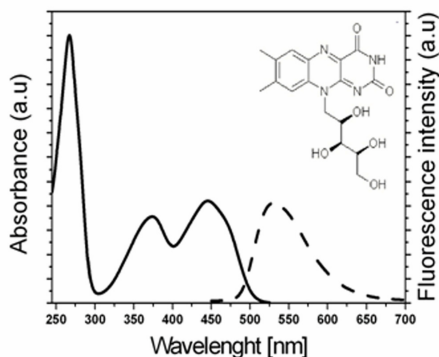


Figure 1. Absorption (solid line) and fluorescence (dashed line) spectra of riboflavin in water ($10^{-4} M$). The fluorescence spectra were recorded using 445 nm excitation wavelength. The inset shows the molecular structure of riboflavin.

Figure 2 a) shows fluorescence emission spectra of riboflavin in milk subjected to heating (from 20 to $100^{\circ}C$). The emission spectra were recorded using 445 nm excitation wavelength. As expected, the emission band of riboflavin in milk exhibits a small blue-shift to 528 nm (relative to the reference spectrum recorded in water) due to changes of the surrounding environment [4]. We noticed a progressive

decrease in the intensity of the emission band of riboflavin with temperature increasing (Fig. 2 a)). The intensity of emission band decreases almost twice but does not disappear completely, and remained constant during the cooling (as is suggested in Figure 2 b)). This effect can be partially assigned to vitamin photodegradation and fluorescence quenching after local environmental changes.

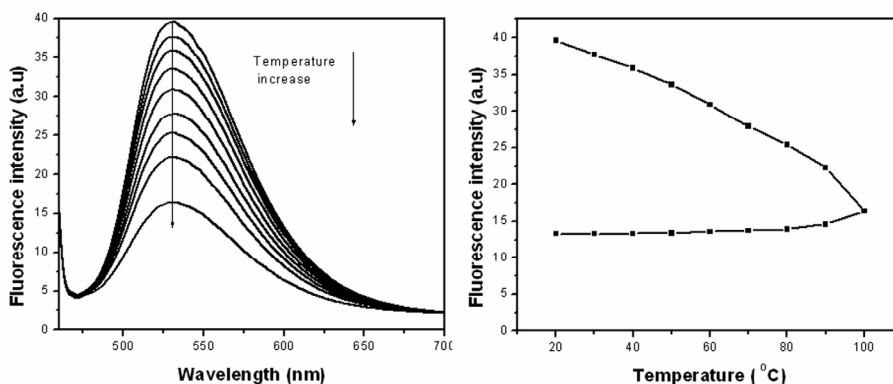


Figure 2. (a) Time evolution of fluorescence emission spectra of riboflavin in milk; (b) Variation of fluorescence intensity as function of temperature during heating-cooling cycle between 20 to 100°C. The arrow in (a) depicts the decrease of the band intensity with increasing temperature.

Data in literature show that the riboflavin retention in feeding products during the thermal processing is good enough, especially in acid conditions [5][6]. However, it is known that riboflavin excited state can induce the photosensitized oxidation of food components (e.g lipids, proteins). Thus, in our case under irradiation at 445 nm riboflavin is excited and, by reverting to its ground state, riboflavin produce either free radicals (Type I reaction) and/or reactive oxygen species (Type II reaction) [7].

Generally, photochemical processes have a low energy of activation and the increasing temperature seems not to have a significant impact on photooxidation. However, the autooxidative processes of unsaturated lipids which proceed ones the oxidation started, are affected by temperature [8]. Even the shortest exposure on the light may have a harmful effect and the process which follows the formation of hydroperoxides (ROOH) is their thermal decomposition which generate a new chain of radicals and reactive species (e.g. OH \cdot) which extend autoxidative process [9]. Thus, in our case the increasing temperature during irradiation could have a decisive impact in autoxidative process as previously reported [10].

Some of the authors assigned the temperature effect to initiating process: the unsaturated fatty acids have their bounds disposed in allyl systems, more stable than in the conjugated systems or, in this form the interaction with singlet oxygen becomes slower. Therefore, even mild heat treatment can affect double bond rearrangement (isomer formation), with an increase in reactivity to singlet oxygen [11].

Thus, riboflavin fluorescence quenching may be due to vitamin reaction with singlet oxygen and hydroxyl radical, formed by photosensitized riboflavin [12] and reactive species formed as a result of peroxide decomposition ($\approx 77^\circ\text{C}$) [13]. Moreover, riboflavin can react with methionine and cysteine resulted by heat ($65\text{-}70^\circ\text{C}$) denaturation of whey proteins [1][12]. On the other hand, lower solubility of oxygen with temperature increasing [9] lead to an oxygen deficiency in sample, therefore the chemical equilibrium moves to the I Type of reaction, where riboflavin degrades forming free radicals which will continue the reaction chain, in this way degradation becomes irreversible [12].

Figures 3 (a) and (b) present the excitation and emission spectra of Vitamin A in milk measured under the heating and cooling. The excitation spectrum (Figure 3 a)) was recorded setting the emission wavelength at 410 nm. As seen, vitamin A exhibits a maximum absorption at 322 nm and two shoulders at 307 and 295 nm. The emission spectrum (Figure 3 b)) were recorded using 322 nm excitation wavelength. In the 530 nm region of emission spectra, it can see a small extension which can be assigned to riboflavin emission. Both the intensity and shape of spectra change when the temperature increased between 20°C and 100°C (see Figure 3 (a)). On the other hand we noticed that the emission spectrum of vitamin A show a progressive fluorescence intensity decrease with increasing temperature from 20 to 100°C which is partially reversible by gradual return to the initial temperature from 100 to 20°C (see Figure.3 b)). On the contrary, the maximum extinction band correlated to absorption at 322 nm evolves irreversibly under the thermal process (Fig.3 (a)). We noticed also that the 307 nm absorption band disappears with increasing temperature (see Figure 3 a) and that there is a clear variation of the ratio between the intensity of 322 nm and 293 nm bands.

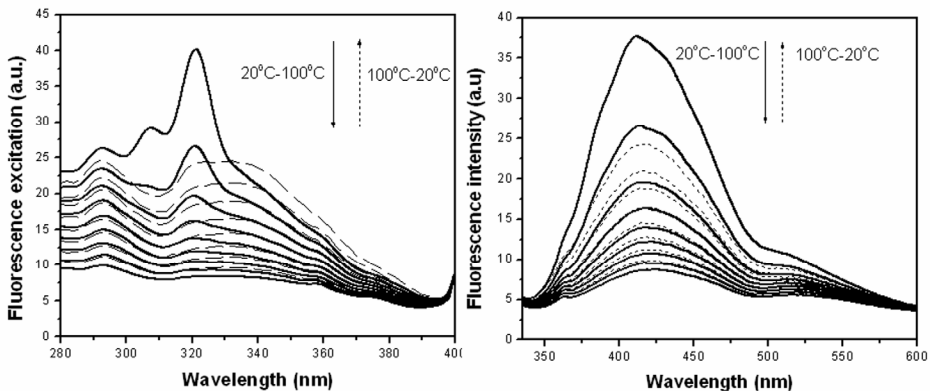


Figure 3. Excitation (a) and fluorescence (b) spectra of Vitamin A in milk measured under the heating (from 20 to 100°C temperature -solid lines) and cooling (from 100 to 20°C temperature -dotted lines). The spectra were recorded using a) 410 nm emission wavelength and b) 322 nm excitation wavelength.

Using vitamin A as an intrinsic fluorescent probe, as was shown previously, the vitamin's excitation spectrum (Figure 3 a)) bring important information about the physical state of the tryglicerides in the fat globule and the extend of modification strongly depend on the melting point of the triglycerides [14]. According to literature, Vitamin A remains chemical unchanged during the thermal process (if there is no oxygen), but it is exposed to isomerisation which leads to losing vitamin A's activities [9]. On the other hand it can be consistent with the conversion of all-trans isomer form in cis-isomer form which exhibits small Vitamin A's activity. The partial reversible feature of spectral shape is, probably, because of a part of Vitamin A reappeared in all-trans isomer form (Fig. 3 dotted lines). If the oxygen is present (like in this case), probably, there is some losses of vitamin A because of direct oxidation.

CONCLUSION

Using temperature as an environmental parameter under control, we observed that, despite of standard riboflavin and vitamin A stability, their fluorescence spectra are modified in milk with the temperature increase. This is because a part of riboflavin molecules can degrade irreversibly, the degradation being the result of photosensitized riboflavin accompanied by several chemical transformations in the nearby environment as hydroperoxide decomposition and whey protein degradation. On the other hand the spectroscopic changes of Vitamin A when the temperature increases, can be mainly related to Vitamin A conformational changes with some contribution from nearby environment changes (tryglicerides).

These results exhibit potential applicability in studying the quality of dairy products, with great importance in food safety.

ACKNOWLEDGMENTS

This work was supported by The National University Research Council from Romania (CNCSIS) in the frame of the PN-II research programs under the project PCCE No 129/2009.

REFERENCES

1. P. F. Fox, P. L. H. McSweeney, "Dairy Chemistry and Biochemistry", 1st edn., London: Blackie Academic & Professional, 1998, 265, 266, 279.
2. G. Mortensen, G. Bertelsen, B. K. Mortensen, H. Stapelfeldt, Journal of Dairy Science, 2004, 14, 85-102.
3. F. Mestdagh, B. De Meulenaer, J. De Clippeleer, Journal of Dairy Science, 2005, 88, 499-510

4. J. P. Wold, A. Veberg, A. Nilsen, V. Iani, P. Juzenasn, J. Moan, *International Dairy Journal*, 2005, 15, 343-353.
5. T. P. Coultate, "Food, the chemistry of its components", 4th edn., UK: The Royal Society of Chemistry, 2002, 292.
6. J. M. De Man, "Principles of Food Chemistry", 3rd edn., USA: Aspen Publication, 1999, 376.
7. L. H. Skibsted, *Bulletin of the International Dairy Federation*, 2000, 346, 3-9.
8. C. M. Andersen, J. P. Wold, G. Mortensen, *International Dairy Journal*, 2006, 16, 1483-1489.
9. O. R. Fennema, "Food Chemistry", 3rd edn., New York: Marcel Dekker, 1996, 577.
10. D. Kristensen, L. H. Skibsted, *Journal of Agricultural and Food Chemistry*, 1999, 47, 3099-3104.
11. W. Aurand, H. Boone, G. Giddings, *Journal of Dairy Science*, 1977, 60, 363-369.
12. E. Choe, R. Huang, D. B. Min, *Journal of Food Science*, 2005, 70, 20-28.
13. <http://www.cem.msu.edu/~reusch/OrgPage/bndenrgy.htm>
14. R. Karoui, G. Mazerolles, E. Dufour, *International Dairy Journal*, 2003, 13, 607-620.

SYNTHESIS, CHARACTERIZATION AND PROTEIN FUNCTIONALISATION OF CALCINATED BIOGLASSES

E. LASZLOFFI*, I.P. FODOR*, V. SIMON*

ABSTRACT. The protein attachment onto surface of powdered bioactive glasses and glass-ceramics was studied in simulated body fluid enriched with bovine serum albumin. The particles size distribution showed that size of the particles cover a range between 10 nm and 37 nm, with a maximum around 25 nm. The structure of the samples was analyzed using X-ray diffraction. Steady-state fluorescence analysis showed that tryptophan fluorescence in the investigated SBF/BSA solutions depend on the surface structure, and implicitly on the calcination temperature of the samples.

Keywords: Bioglass; calcination; BSA; tryptophan fluorescence.

INTRODUCTION

Glasses of SiO₂-CaO-Na₂O-P₂O₅ system proved to be bioactive and proper for tight attachment to the bone tissue, that determined the investigation of several glass compositions and elaboration of models concerning the tissue-bonding mechanisms [1–3].

The bone typically consists, by weight, of 25% water, 15% organic materials and 60% mineral phases. The mineral phase consists primarily of calcium and phosphate ions, with traces of magnesium, carbonate, hydroxyl, chloride, fluoride, and citrate ions [4].

An alternative synthesis process used to obtain bioactive glasses production is based on the sol-gel method [2, 5]. This method allows the synthesis of highly microporous materials with high surface area. The sol-gel route is based on the controlled hydrolysis and condensation of metal alkoxides that lead to a suspension of colloidal particles (sol), which upon polycondensation forms an interconnected network structure, the gel. Heat treatment stages (aging, drying, and stabilization) are then conducted, leading to a final glass structure [6].

Adsorption of proteins at solid/liquid interfaces plays an major role in the behavior of biomaterials in biological media. It is generally recognized that proteins undergo conformational changes upon adsorption [7].

* Babes-Bolyai University, Faculty of Physics & Institute of Interdisciplinary Research in Bio-Nano-Sciences, 400084

The aim of this work was to synthesize a SiO₂-CaO-Na₂O-P₂O₅ bioactive glass using the sol-gel method, to obtain glass-ceramic samples after partial crystallization induced by heat treatments, and to study the protein functionalization of samples treated at different temperatures.

EXPERIMENTAL

The composition of the bioactive glass belonging to SiO₂-CaO-Na₂O-P₂O₅ system was 56SiO₂·20CaO·20Na₂O·4P₂O₅, in molar percentage. The reagents used for the preparation were tetraethoxysilan (TEOS) as precursor for SiO₂, calcium nitrate tetrahydrate, as precursor for CaO, anhydric sodium carbonate, precursor for Na₂O and ammonium dibasic phosphate as precursor for P₂O₅, where SiO₂ and P₂O₅ are network formers, while CaO and Na₂O act as network modifiers. The resulting solution was gelled and aged at 36 °C for 5 day, dried at 110°C, and heat treated at three different temperature chosen based on the results obtained by thermogravimetric and differential thermal analyses (TG/DTA).

Thermal analyses were performed from room temperature to 1000°C, with heating rate of 10 °C/min in air, on Shimadzu analyzer DTG-60H which simultaneously registers the thermogravimetric (TG) and differential thermal analysis (DTA) curves. Parts of the sample dried at 110°C were thereafter calcinated at 300, 700 and 850°C.

The structure of the treated samples was investigated using X-ray diffraction (XRD), with a Shimadzu XRD- 6000 diffractometer, using CuK α radiation ($\lambda = 1.5418 \text{ \AA}$), with Ni-filter.

The particle size distribution of the thermally treated samples was investigated with SALD-7101 particle size analyzer. The analyzed samples were ground to a fine powder using Retsch MM 200 Mill Mixer, for 10 minutes at the frequency of 30 Hz.

Protein attachment on samples was accomplished in simulated body fluid (SBF) enriched with bovine serum albumin (BSA). The SBF was prepared according to Kokubo's protocol [8], by dissolving the following chemical reagents one by one: NaCl, NaHCO₃, KCl, K₂HPO₄·3H₂O, MgCl₂·6H₂O, CaCl₂, Na₂SO₄ and (CH₂OH)₃CNH₂ (Tris) into deionized water. The pH of the solution was adjusted at 7.4 at 36.5 °C, the normal body temperature. The concentrations of inorganic ions in SBF are similar to those of human blood plasma. The samples were soaked in SBF enriched with BSA for different time periods at the constant temperature 36,5°C. The SBF/BSA solution was prepared by adding 0.3 mg BSA to 30 ml SBF.

Steady-state fluorescence measurements were performed on Jasco spectrofluorimeter FP-6300. The excitation wavelength was 295 nm and fluorescence spectra were recorded from 250 to 500 nm.

RESULT AND DISCUSSION

The DTA curve (Fig 1.) shows two endothermic peaks, a first one at 77.7oC and a second one around of 236oC, and they are accompanied by two weight losses evidenced in TG run, corresponding to ethanol and water removal. An exothermic peak at 284,5oC can be related to residual salts decomposition, and an endothermic peak at 673,2oC to a desorption process, very probably of intraporous adsorbed hydroxyl groups. According to these thermal analysis results, the heat treatment temperature were choosed at 300oC, at 700oC and at 850oC.

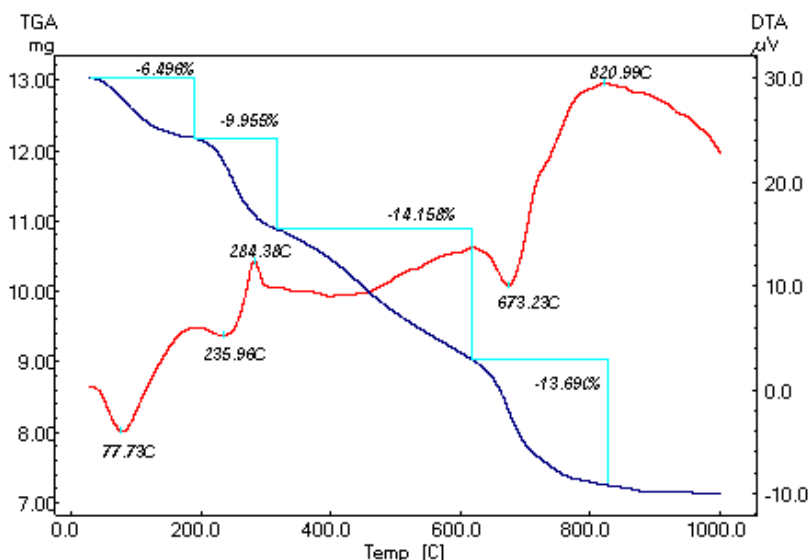


Fig.1. TG/DTA curves of the dried gel.

The structure of the treated samples was identified using X-ray diffraction. By inspecting the XRD patterns (Fig. 2) it can be noticed that the sample calcinated at 300oC is still preponderantly amorphous, while after 700oC and 850oC treatments the samples contain crystalline phases pointed out by diffracton lines recorded at $2\theta = 22.9, 26.6, 29.3, 32.2, 33.42, 34.1, 41, 44.4, 46.9$ and 48.4θ , and at $2\theta = 21.3, 22.7, 23.3, 26.4, 28.5, 32.2, 32.8, 35.7, 40.4, 44.5, 46.9$ and 48.3θ , respectively. Diffraction lines close to $23.3, 33.4, 34.1$ and 48.3θ are assigned to $\text{Na}_2\text{CaSi}_3\text{O}_8$ (JCPDS 12–671), but the last two ones, as a diffraction lines occurs at 26.4θ , can be related to $\text{Na}_2\text{Ca}_2(\text{SiO}_3)_3$ crystalline phase (JCPDS 1–1078) [9–11]. The sample treated at 850oC presents an intense peak that could arise from a surprising low temperature development of SiO_2 β -cristobalite (JCPDS 83-2469) [12].

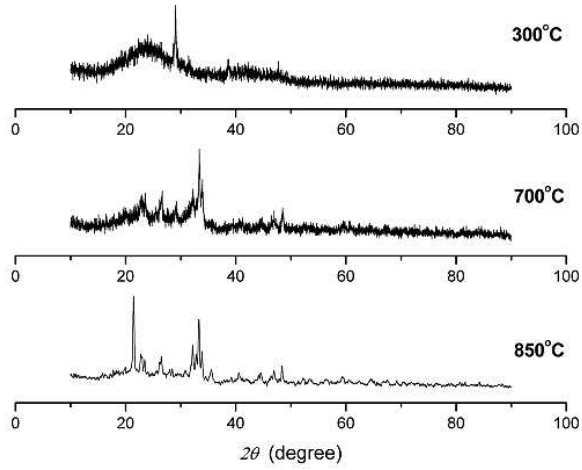


Fig.2. X-ray diffraction patterns of the calcinated samples.

The particle size distribution of the calcinated samples (Fig. 3) shows that with increasing the treatment temperature, only small changes in the distribution of the particle size occur. The particle sizes are between 10 nm and 37 nm, with a maximum around 25 nm. Small difference can be observed for the sample treated at 300oC, where the distribution is slight higher around 30 nm and 35 nm, comparatively with the samples treated at 700oC and 850oC

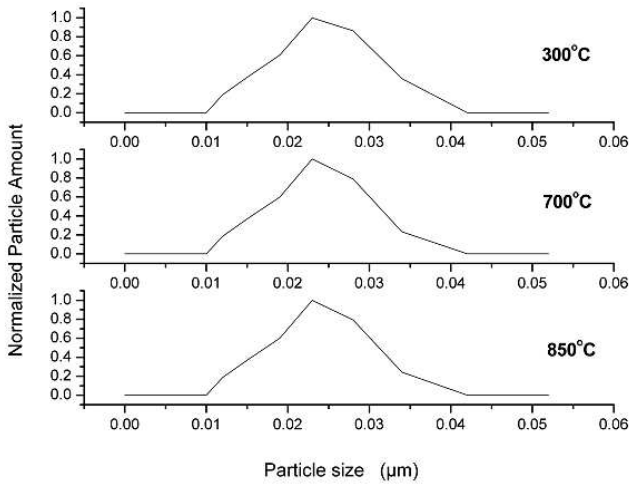


Fig. 3. Particle size distribution.

A biomaterial inserted into the body will immediately encounter proteins. In this study we evaluated the albumin attachment using fluorescence spectroscopy, and this was indirectly a first biocompatibility test. It is known that in case of proteins there are three amino acids with intrinsic fluorescence properties, phenylalanine, tyrosine and tryptophan, but only tyrosine and tryptophan are used experimentally because their quantum yields (emitted photons/ excited photons) is high enough to give a good fluorescence signal, so the advantage of the fluorescence of tryptophan is that it is very sensitive to the polarity of the local environment, the emission peak will shift depending on the dielectric constant of the local environment. If the conformation of a protein changes, due to the local environment around the tryptophan, this will be reported by a change in the position of the fluorescence peak [13]. The fluorescence spectrum of BSA presents strong emission with maximum at 345 nm, when excited at 295 nm [14].

The effect of the investigated samples on BSA fluorescence intensity after few hours after immersion is shown in Fig. 4, and after longer time in Fig. 5. For the solution with BSA, but without sample (Fig. 4a), a small decrease of the fluorescence intensity is observed, due to the protein interaction with the ions from SBF solution. The intensity seems to be very stable in the next 7 days (Fig 5.a). As in the protein solution was soaked the sample calcinated at 300oC, an increase of fluorescence intensity was observed in first 24 hours (Fig 4d). In the next 7 days the intensity of the fluorescence signal is fluctuant (Fig 5d), with a minimum after 72 hours and a maximum after 120 hours. For the sample calcinated at 700oC, the fluorescence intensity measured in the first hours decreases (Fig. 4b), and after 72 hours remains unchanged (Fig. 5b). In the case of the sample calcinated at 850oC, a pronounced decrease of the fluorescence intensity is observed in the first hours (Fig. 4c), followed by an increase up to the third day, and thereafter a progressive extinction takes place (Fig. 5c).

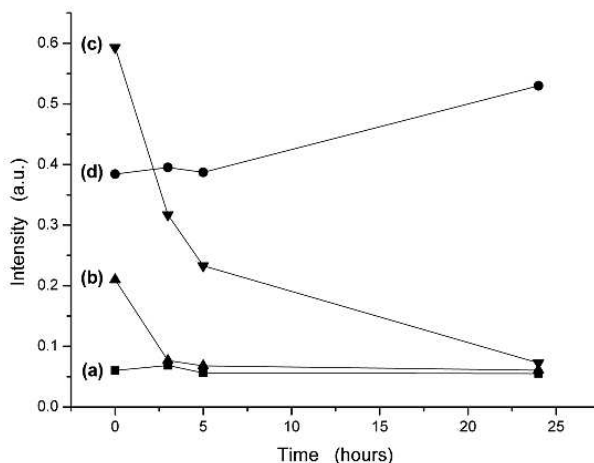


Fig. 4. The time dependence of BSA fluorescence intensity during the first 24 hours in (a) SBF/BSA reference solution; (b) SBF/BSA solution with 700°C calcinated sample; (c) SBF/BSA solution with 850°C calcinated sample; (d) SBF/BSA solution with 300°C calcinated sample.

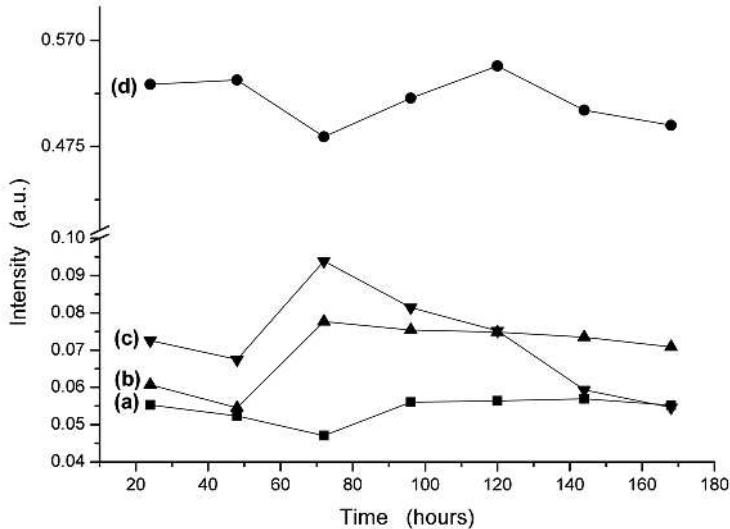


Fig. 5. The time dependence of BSA fluorescence intensity during a week in (a) SBF/BSA reference solution; (b) SBF/BSA solution with 700°C calcinated sample; (c) SBF/BSA solution with 850°C calcinated sample; (d) SBF/BSA solution with 300°C calcinated sample.

With respect to the position of the fluorescence peak, a shift of λ_{\max} to higher wavelengths is noticed immediately after immersion of the sample in the protein solution (Fig. 6), that is not more observed after 4 days for the samples calcinated at 700°C and 850°C. Further analysis of these results is necessary to evaluate the changes of the polarity around the fluorophore. A blue shift of λ_{\max} means that the amino acid residues are located in a more hydrophobic environment, and are less exposed to the solvent, while a red shift of λ_{\max} implies that the amino acid residues are in a polar environment and are more exposed to the solvent [15, 16]. The red shifts of the maximum emission wavelength suggest that immediately after the immersion of the samples the protein is exposed to a more polar environment.

CONCLUSION

The structure of 56SiO₂·20CaO·20Na₂O·4P₂O₅ sol-gel derived bioglass is preponderantly amorphous after calcination at 300°C. The 700°C and 850°C calcination led to glass-ceramic samples wherein Na₂CaSi₃O₈ and Na₂Ca₂(SiO₃)₃ are the main crystalline phase.

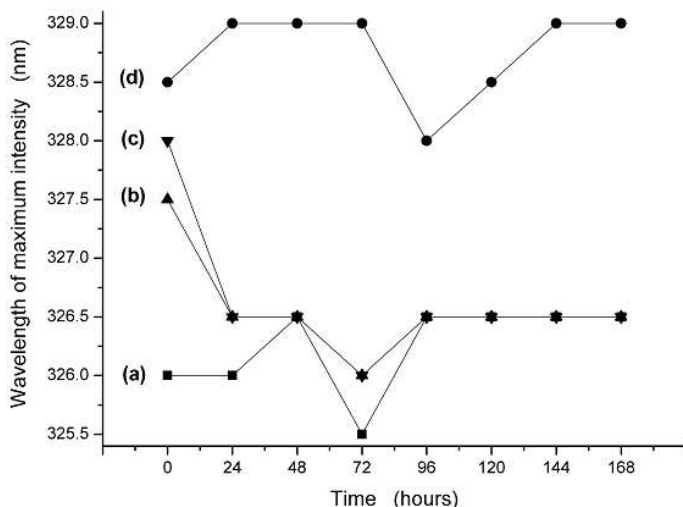


Fig. 6. Dependence of fluorescence emission maxima of BSA as a function of samples residence time in SBF/BSA solution.

After functionalization of the powdered samples with BSA protein, the fluorescence results indicate that the tryptophan fluorophore perceives changes in the polarity of the local environment, which are related to the surface structure changes of the bioactive glass and glass-ceramic samples. The red shift noticed immediately after immersion of the samples in the SBF/BSA solution indicates that the tryptophan is subjected to a more polar environment.

ACKNOWLEDGEMENT

This work was possible with the financial support of the Sectoral Operational Programme for Human Resources Development 2007-2013, co-financed by the European Social Fund, under the project number POSDRU/107/1.5/S/76841 with the title „Modern Doctoral Studies: Internationalization and Interdisciplinarity”.

REFERENCES

1. G. Pezzotti, M. C. Munisso, A. A. Porporati, K. Lessnau, *Biomaterials*, 31, 6901 (2010).
2. R.F. Bartholomeu, B.L. Butler, H.L. Hoover, C.K. Wu, *J. Am. Ceram. Soc.*, 63 (1980) 481
3. T. Yamamuro, L. Hench, J. Wilson, *Handbook of Bioactive Ceramics*; vol. 1, CRC Press: Boca Raton, 1990.

4. L.L. Hench, J. Wilson, *An Introduction to Bioceramics*; World Scientific, London, 1993.
5. L.L. Hench, *J. Am. Ceram. Soc.*, 81, 1705 (1998).
6. *Biomaterials Science: An Introduction to Materials in Medicine*; Eds. B.D. Ratner, A.S. Hoffmsn, F.J. Schoen, J.E. Lemons, Academic Press, San Diego, 1996.
7. R. Li, A.E. Clark, L. Hench, *J. Appl. Biomater.*, 2, 231 (1991).
8. *Encyclopedia of Biomaterials and Biomedical Engineering*, Eds. G.E. Wnek, G.L. Bowlin, Marcel Decker, New York, 2005.
9. M.F.M. Engel, C.P.M. van Mierlo, A.J.W.G. Visser, *J. Biol. Chem.* 277, 10922 (2002).
10. *Bioceramics and Their Clinical Applications*, Ed. T Kokubo, CRC Press, New York, 2008.
11. H.A. ElBatal, M.A. Azooz, E.M.A. Khalil, A.S. Monem, and Y.M. Hamdy, *Mater. Chem.Phys.*, 2003, 80, 599-609
12. R.L. Siqueira, O. Peitl, E.D. Zanotto, *Mat. Sci. Eng. C*, doi:10.1016/j.msec.2011.02.018 (2011)
13. F.H. ElBatal, A. ElKheshen, *Mater. Chem. Phys.*, 110, 352 (2008).
14. J. Li, H. Ma, Q. Fang, *Ceram. Int.*, 34, 1791 (2008).
15. J. Benesch, G. Hungerford, K. Suhling, C. Tregidgo, J.F. Mano, R.L. Reis, *J. Colloid Interf. Sci.*, 312, 193 (2007).
16. B. Ojha, G. Das, *Chem. Phys. Lipids*, 164, 144 (2011).
17. A.Varlan, M. Hillebrand, *Molecules*, 15, 3905 (2010).
18. G. Zhang, Y. Wang, H. Zhang, S. Tang, W. Tao, *Pestic. Biochem. Physiol.*, 87, 23 (2007).

SURFACE-ENHANCED RAMAN DETECTION OF MELAMINE AT TRACE LEVEL

N. E. MIRCESCU*, G. S. MILE, M. OLTEAN, V. CHIȘ, N. LEOPOLD

ABSTRACT. Reliable, fast detection and quantification of melamine residues in food became a very important safety issue. In this work, we report a joint experimental and theoretical study performed on neutral and protonated forms of melamine, in order to determine valuable physico-chemical properties of the molecule. Surface-enhanced Raman scattering (SERS) spectroscopy was used in conjunction with quantum chemical calculations in order to characterize the structural and vibrational properties of this molecule. SERS spectra of melamine have been assigned based on Density Functional Theory (DFT) calculations at B3LYP/6-311G++(d,p) level of theory. The possibility of melamine SERS detection at 32.4 $\mu\text{g/ml}$ level is shown.

Keywords: melamine, SERS, DFT, pH-dependence.

INTRODUCTION

This work deals with a new approach able to detect and quantify melamine at trace level using surface-enhanced Raman spectroscopy. The general objective of this research is to describe the monitoring of the ingredients of different foods for avoiding chemical contamination. The maximum limits for a number of chemical residues in foods of animal origin are imposed by different regulators¹. National monitoring programs for chemical residues in different foods, including dairy products, are also mandatory in all EU states².

Although strict regulations regarding the maximum limits of melamine in food products, violations of law are well known. In September 2008, over 1.500 tons of milk powder contaminated with melamine has been sold, particularly in China. As a result, six children have died and more than 300.000 were hospitalized. The investigation revealed that the manufacturers have added melamine to milk in order to fraud the protein level of the product. Following this scandal, the European Commission decided that all products containing milk imported from China must undergo laboratory analysis, and products containing over 2.5 $\mu\text{g/ml}$ melamine will

* Faculty of Physics, Babeș-Bolyai University, Kogălniceanu 1, 400084, Cluj-Napoca, Romania

be destroyed immediately³. Recently, the European Commission assessed the potential for detection of melamine in food⁴.

Melamine (2,4,6-triamino-1,3,5-triazine), with the chemical structure for the neutral form shown in Figure 1(a), is a relatively cheap industrial chemical, mostly used in the production of plastics and glues. It contains 67% nitrogen per mass unit and has been used to fraudulently increase the apparent protein content, as protein level in agricultural products is typically measured by analysis of total nitrogen⁴.

Standard methods for melamine residues analysis are chromatographic methods coupled with mass spectrometry (HPLC-MS, GC-MS), such methods being complex, laborious and requiring a dedicated and pretentious laboratory environment⁵. Limit of detection (LOD) of the HPLC method to measure melamine standard solution was obtained at 1 $\mu\text{g/ml}$ ⁶.

The infestation of melamine in milk powder, sold in Canada, was previously studied by Tittlemier et al⁷. Melamine was detected in 71 of the 94 analyzed products, at concentrations from 4.31 to 346 $\mu\text{g/kg}$. Even if the values are below the maximum allowed limit (2.5 mg/kg), the presence of melamine in the large number of samples suggests the necessity of a close monitoring^{8,9}.

Furthermore, a surface-enhanced Raman scattering (SERS) study on melamine detection in gluten, chicken feed, and processed foods was published, the results being correlated with standard HPLC analysis¹⁰. These authors used KlariteTM as SERS-active substrates, fabricated on silicon wafers coated with gold.

Previously reported works on the detection of melamine generally used gold substrates for SERS measurements¹⁰ or the detection was made indirectly using mercaptopyridine as Raman reporters¹¹. Detection of melamine at trace level in raw materials used for protein pharmaceutical manufacturing by SERS was also very recently reported by Wen et al¹². On the other hand, silver substrates for SERS studies were used by Zhang et al.¹³ for detection of melamine sandwiched between silver nanoparticles and silver nanoarrays and by Du et al.¹⁴ which detected melamine using a silver nanorods array substrate.

In the present study, ultrasensitive Raman (SERS) spectroscopy is proposed as a fast and reliable detection method of melamine in liquid samples. Our results show that SERS based on silver colloids is a simple detection method which compares favorably with the more time consuming and tedious Food and Drug Administration (FDA) standard protocol for quantitative estimation of melamine in foods¹⁵. Moreover, using this method we were able to discriminate between the neutral and protonated forms of melamine. To the best of our knowledge no such study has been reported in the literature so far.

EXPERIMENTAL

Instrumentation Raman spectra were recorded using an Advantage 532 spectrometer (DeltaNu, Laramie, WY). The frequency doubled NdYAG laser emitted at 532 nm with a power of 20 mW. The spectral resolution of the recorded

spectra was $\sim 10 \text{ cm}^{-1}$. The monochromator detection system allowed the simultaneous recording of the whole spectral range between 200 and 3400 cm^{-1} . The SERS spectra were recorded by averaging 4 accumulations, each of 10 seconds exposure time.

Chemicals Hydroxylamine hydrochloride (Sigma-Aldrich, Steinheim, Germany), sodium hydroxide (Sigma-Aldrich, Steinheim, Germany), silver nitrate (Penta, Prague, Czech Republic), and melamine (Merck, Hohenbrunn, Germany) were of analytical reagent grade. Double distilled water was used as solvent.

Preparation of the silver colloid A silver colloidal solution was prepared by reducing Ag^+ with hydroxylamine. For this, 17 mg AgNO_3 were solved in 90 ml distilled water. 17 mg $\text{H}_2\text{NOH} \times \text{HCl}$ ($0.96 \times 10^{-1} \text{ M}$) and 0.25 ml NaOH solution (2M) were added to 10 ml distilled water. The silver colloid was obtained by mixing these solutions under vigorous stirring for 5 minutes. The obtained colloid had a greenish gray color, and the pH of this composition was 9.5. However, during the experiment, a decrease in pH was observed which indicates the release of protons during the reaction, so after 1 day the colloid was stabilized at $\text{pH}=8.5$. The final pH of the colloidal solution can be adjusted by varying the amount of sodium hydroxide added to the hydroxylamine solution.

For the pH dependence SERS study, melamine saturated aqueous solutions at different acid or basic pH values were prepared¹⁶. The standard colloid-melamine solution was obtained at pH 7 and then we added HCl ($0.96 \times 10^{-1} \text{ M}$) or NaOH (2M) solutions to produce an acid or alkaline environment, respectively. pH 12 was obtained by increasing the amount of NaOH solution in the preparation process of the silver colloid from 0.25 ml to 0.32 ml 2M NaOH.

Quantum Chemical Calculations For DFT calculations we used the B3LYP exchange-correlation functional, in conjunction with the 6-311++G(d,p) basis set. The molecular geometry optimization and vibrational wavenumber calculations were performed with the Gaussian 03W software package¹⁷ by using the DFT approach. No imaginary frequencies were obtained for optimized geometries and thus, all the optimized structures represent true minima on the potential energy surface.

The pK_a values and the micro species distribution for melamine were obtained using the dedicated program, MarvinSketch¹⁸.

RESULTS AND DISCUSSION

The B3LYP/6-311++G(d,p) optimized molecular structures of the neutral and protonated melamine are shown in Figure 1. As starting geometries for the optimization processes we used the X-ray structure of the neutral melamine reported by Varghese et al¹⁹.

In Figure 1(a) is shown the neutral species, mostly present in the alkaline solutions, for pH values higher than 8. According to calculations, the chemical structure shown Figure 1(b) is for the simple protonated species, present mostly in acis solutions,

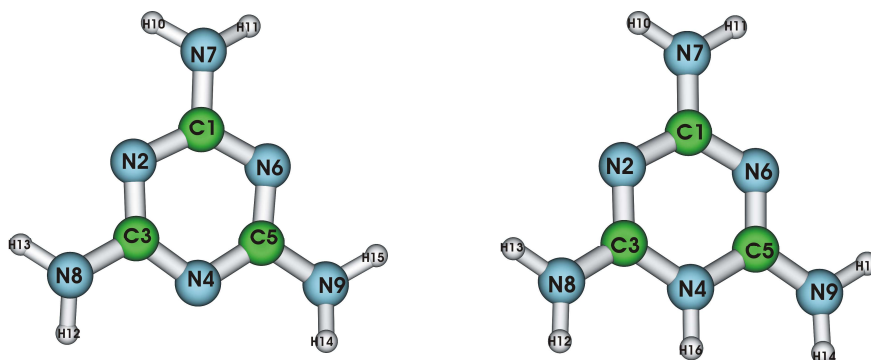
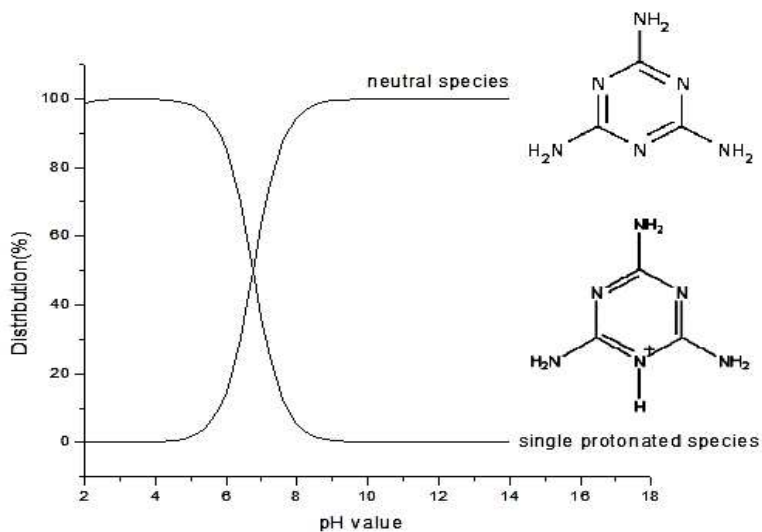


Fig. 1. B3LYP/6-311++G(d,p) optimized molecular structures of the neutral (a) and protonated (b) melamine.

at 5.5-2 pH values. The distribution of these molecular species is shown in Figure 2. Our calculated pKa value is in satisfactory agreement with that recently reported by Jang et al.²⁰ calculated by using the DFT methodology.



At pH=7, both species are present, with equal contributions.

Fig. 2. Distribution of neutral and protonated melamine molecular species.

As resulted from our calculations, the structure of the neutral species is non-planar, while that of the protonated species is planar. The non-planar structure

of the neutral form is mainly due to the non-planarity of the three amino groups of the molecule, the dihedral angle between the triazine ring and the C-NH₂ bond being 1.9°. According to calculations, the NH bonds are between 10.5° and 12° out of the triazine ring plane. Dihedral angles defined by the atoms in the triazine rings are less than 0.5°. Thus, the non-planarity of the molecule is mainly due to the NH bonds in the amino groups, even if small deviations from planarity are noted also for the C and N atoms forming the triazine ring.

It is worth to mention that Drozd and Marchewka²¹ found a planar structure of the neutral and protonated forms of melamine, as the result of performing HF and DFT calculations in conjunction with the 6-311++G(d,p) basis set. Most probably, the planar structure obtained in reference [16] is caused by the use of a planar structure of melamine as a starting geometry. However, our calculations performed at B3LYP/6-311++G(d,p) level of theory, without imposing any symmetry, lead to a C1 structure of neutral melamine which revealed the non-planar structure to be the most stable one, with two pairs of NH₂ groups pointing out to one side of the triazine ring, the other one pointing towards the opposite direction. Our results are in perfect agreement with those reported by Meier²² and also in line with X-ray and neutron diffraction experimental data¹⁹. Furthermore, frequency calculations performed on the optimized geometry, predict it as a local minimum on the potential energy surface (PES).

Contrary to the neutral form, in the case of the protonated species, at B3LYP/6-311++G(d,p) level of theory, we found a completely planar structure, even if we used as a starting geometry a structure significantly distorted from planarity. Once again, the frequency calculations confirmed the optimized planar structure as a local minimum on the PES. The single protonated form of melamine can occur by protonation on either one of the nitrogens of the triazine ring, the three protonation sites being, however, equivalent.

Excepting the planarity of the protonated structure, other major differences between the geometries of the two species resulted. For example, the lengths of the bonds for the triazine ring atoms are increasing in the case of the two C-N₄ bonds from 1.34 Å (for the neutral species) to 1.38 Å (for the protonated species). Also, a decrease in bond length is noticed for the C₁-N bond lengths which are reduced from 1.34 Å to 1.31 Å. The value for N(4)-C(5)-N(6) and N(4)-C(3)-N(2) angles is 121° in the case of neutral melamine and 126° for the protonated species. On the other hand, the value for N(4)-C(5)-N(9) and N(4)-C(3)-N(8) angles is increasing from 117° for the neutral species to 120° for the protonated one. Thus, the major structural differences are noticed in the proximity of the protonated nitrogen, while the other parameters remain almost unchanged.

Molecular structure and vibrational spectra of melaminium acetate acetic acid solvate monohydrate have been reported by Pekparlak et al.²³. In this complex, the melamine molecule exists in its protonated form. Our calculated geometrical parameters of the protonated melamine are in very good agreement with the

corresponding results reported²³⁻²⁴. Also, the experimental IR and Raman spectra reported in the above mentioned references fully support the assignments of the most important bands observed in our SERS spectra.

Vibrational mode assignments were made by visual inspection of modes animated by using the Gaussview program by considering both, the band positions and the intensity pattern.

Melamine is slightly water soluble (3.24 mg/ml), thus the achieved concentration in water was not high enough to record the conventional Raman spectra. In order to overcome this inconvenience, SERS spectroscopy was employed.

Physical properties, like solubility, are often very sensitive to the concentration of the hydrogen ions of the medium. Also, due to structural change by protonation/deprotonation the SERS spectra differ, depending on the molecular species adsorbed on the metal surface²⁵. Thus, the SERS spectra of melamine at different pH values (pH 3, 7, 12) were recorded using silver colloids and the sensitivity (detection limit) of the SERS method was evaluated. Typical spectra are shown in Figure 3.

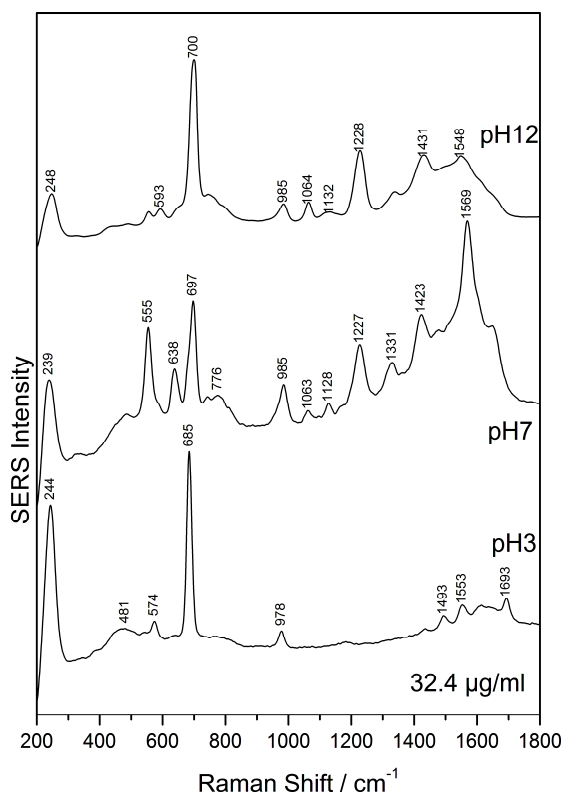


Fig. 3. SERS spectra (from top to bottom) of melamine at pH 12 (neutral molecular form), pH 7, pH 3 (protonated molecular form) recorded at a concentration of melamine of 32.4 $\mu\text{g/ml}$.

The difference in wavenumbers is determined by the structural changes of melamine and the response of the two different species present in the colloid solution at the SERS chemical and electromagnetic enhancement. As presented in Figure 3, in acidic solution, where the single protonated form of melamine is dominant, the SERS spectrum shows a strong band at 685 cm^{-1} (experimental Raman band 690 cm^{-1})²³. According to DFT calculations, it is assigned to an in-plane vibration due to the deformation of CNC angles in the triazine ring, with an important translational movement of the C-NH₂ groups. The corresponding calculated wavenumber is 683 cm^{-1} , in perfect agreement with the experiment. Its calculated Raman activity is also in excellent agreement with the experiment, being the most intense calculated Raman active mode in the region below 3000 cm^{-1} . This band suffers a quite significant blue-shift in basic solution, at pH=12, where neutral melamine molecules are expected, its corresponding experimental wavenumber being 700 cm^{-1} . According to calculations performed on neutral melamine, the theoretical wavenumber is 680 cm^{-1} , with the same assignment like for the protonated species. Thus, the experimentally observed blue shift is not reproduced by calculations. However, as it is also observed in the experimental spectrum, we can safely make the correspondence between the two bands from neutral and protonated melamine.

Another band which is clearly observed in SERS spectrum of the protonated form is that located at 978 cm^{-1} . It undergoes also a blue shift in the spectrum of neutral species, at 985 cm^{-1} . According to calculations, it corresponds to the δ (NCN) trigonal bendings and its theoretical position and protonated-neutral shift are very well reproduced. Thus, for the protonated form, the calculated wavenumber is 981 cm^{-1} (experimental 980 cm^{-1})²³, while for the neutral form is 990 cm^{-1} .

The band at 1228 cm^{-1} seen in the SERS spectrum at pH=12 is missing in acidic solution. Its broadening is an indicative of a mode involving the NH₂ groups which are available for hydrogen bonding. DFT calculations predict a theoretical wavenumber at 1267 cm^{-1} , corresponding to a $\nu(\text{CN}) + \rho(\text{NH}_2)$ vibrational mode.

The vibrational mode at 1431 cm^{-1} appears only in the alkaline solutions, being characteristic for the neutral molecular form of melamine²¹ and predicted by DFT the calculations at 1426 cm^{-1} , being assigned for the ring stretching deformation coupled to NH₂ bending vibrations. The experimental band at 1553 cm^{-1} at pH=3 corresponds to the calculated values of 1567 cm^{-1} which are assigned by the DFT calculations to the NH₂ bending vibration. This band shifts to higher wavenumbers going from acidic to neutral pH values.

It is important to mention here that hydrogen bonding interactions between melamine and water molecules can affect the geometry of the melamine molecule and its vibrational spectra²⁶. Consequently, minor discrepancies observed between theory and experiment can be safely explained considering such H-bonding interactions.

As shown in Fig.3, the SERS spectrum of melamine at pH 7 shows spectral features of both, neutral and protonated melamine.

CONCLUSIONS

SERS spectroscopy in conjunction with DFT calculations performed for the neutral and protonated molecular forms of melamine allowed to identify specific bands for the neutral and protonated species of melamine.

Thus, it is shown that the SERS bands at 685 cm^{-1} and 978 cm^{-1} in the spectrum of protonated melamine shift to 700 cm^{-1} and 985 cm^{-1} , respectively for the neutral form. Another clear evidence useful for the discrimination between the two forms is the band at 1228 cm^{-1} seen only in the case of neutral form.

Being able to detect the presence of melamine in water at a concentration of $32.4\text{ }\mu\text{g/ml}$, SERS spectroscopy was demonstrated to be a fast, reliable and a not-expensive method for melamine detection in liquid samples.

ACKNOWLEDGMENTS

This work was possible with the financial support of the Sectoral Operational Programme for Human Resources Development 2007-2013, co-financed by the European Social Fund, under the project number POSDRU/107/1.5/S/76841 with the title „Modern Doctoral Studies: Internationalization and Interdisciplinarity”. Financial support (PhD fellowship) from grant POSDRU/CPP107/1.5/S/76841 is highly acknowledged by N.E.M. and G.S.M. Financial support from CNCSIS-UEFISCSU, project number PN II-RU TE_323/2010 is highly acknowledged by N.L.

REFERENCES

1. O.J. Eur. Comm., EEC Council Regulation for the establishment of maximum residue limits of veterinary medicinal products. In No. 2377/1990, 1990; pp 1-8.
2. O.J. Eur. Comm., EC Council Directive to monitor certain substances and residues in live animals and animal product. In 1996/23/EC, 1996.; pp 10-32.
3. Commission Decision In 2008/798/EC.
4. A. Breidbach, K. Bouten, K. Kroger and F. Ulberth, *Anal. Bioanal. Chem.*, 396, 503 (2010).
5. S. Tittlemier, *Food Addit. Contam.*, 27, 129 (2010).
6. L. He. Application of Surface enhanced Raman Spectroscopy to food safety issues. University of Missouri, Missouri, 2009.
7. S.A. Tittlemier, B.P.Y. Lau, C. Menard, C. Corrigan, M. Sparling, D. Gaertner, K. Pepper and M. Feeley, *J. Agr. Food Chem.*, 57, 5340-5344 (2009).
8. L. Yongliang, *Appl. Spectrosc.*, 63, 477 (2009).
9. S. Okazaki, M. Hiramatsu, K. Gonmori, O. Suzuki and A.T. Tu, *Forensic Toxicol.*, 27, 94-97 (2009).
10. M. Lin, L. He, J. Awika, L. Yang, D.R. Ledoux, H. Li and A. Mustapha, *J. Food Sci.*, 73, T129-T134 (2008).

11. T. Lou, Y. Wang, J. Li, H. Peng, H. Xiong and L. Chen, *Anal. Bioanal. Chem.*, 1-6 (2011).
12. Z.Q. Wen, G. Li and D. Ren, *Appl. Spectrosc.*, 65, 514-521 (2011).
13. J. Zhang, S. Qu, L. Zhang, A. Tang and Z. Wang, *Spectrochim. Acta, Part A*, 79, 625-630 (2011).
14. X. Du, H. Chu, Y. Huang and Y. Zhao, *Appl. Spectrosc.*, 64, 781-785 (2010).
15. <http://www.cfsan.fda.gov/~frf/seadwpe.html> Questions and answers on FDA's import alert on farm-raised seafood from China (Accessed 6/28/2007).
16. N. Leopold and B. Lendl, *J. Phys. Chem. B*, 107, 5723-5727 (2003).
17. M.J. Frisch, G.W. Trucks, H.B. Schlegel, G.E. Scuseria, M.A. Robb, J.R. Cheeseman, V.G. Zakrzewski, J.A. Montgomery Jr, R.E. Stratmann, J.C. Burant, S. Dapprich, J.M. Millam, A.D. Daniels, K.N. Kudin, M.C. Strain, O. Farkas, J. Tomasi, V. Barone, M. Cossi, R. Cammi, B. Mennucci, C. Pomelli, C. Adamo, S. Clifford, J. Ochterski, G.A. Petersson, P.Y. Ayala, Q. Cui, K. Morokuma, D.K. Malick, A.D. Rabuck, K. Raghavachari, J.B. Foresman, J. Cioslowski, J.V. Ortiz, A.G. Baboul, B.B. Stefanov, G. Liu, A. Liashenko, P. Piskorz, I. Komaromi, R. Gomperts, R.L. Martin, D.J. Fox, T. Keith, M.A. Al-Laham, C.Y. Peng, A. Nanayakkara, C. Gonzalez, M. Challacombe, P.M.W. Gill, B. Johnson, W. Chen, M.W. Wong, J.L. Andres, C. Gonzalez, M. Head-Gordon, E.S. Replogle and J.A. Pople *Gaussian 03, Revision E.01-SMP*; Gaussian, Inc: Pittsburgh PA, 2003.
18. MarvinSketch 5.2; ChemAxon Ltd, www.chemaxon.com: Budapest, Hungary.
19. J.N. Varghese, A.M. O'Connell and E.N. Maslen, *Acta Crystallogr., Sect. B: Struct. Sci.*, 33, 2102-2108 (1977).
20. Y.H. Jang, S. Hwang, S.B. Chang, J. Ku and D.S. Chung, *J. Phys. Chem. A*, 113, 13036-13040 (2009).
21. M. Drozd and M.K. Marchewka, *J. Mol. Struct. Theochem*, 716, 175-192 (2005).
22. R.J. Meier, *J. Mol. Struct. Theochem*, 759, 249-250 (2006).
23. A. Pekparlak, D. Avci, H. Comert and Y. Atalay, *Spectrochim. Acta, Part A*, 77, 696-702 (2010).
24. E. Tarcan, O. Altindag, D. Avci and Y. Atalay, *Spectrochim. Acta, Part A*, 71, 169-174 (2008).
25. N. Leopold, "Surface-Enhanced Raman Spectroscopy. Selected Applications", Napoca Star: Cluj-Napoca, 2009.
26. C. Yang, Y. Liu, L. Li and F. Zhang, *Spectrochim. Acta, Part A*, 75, 1329-1332 (2010).

THE FERROMAGNETIC ONSET IN MnNi ALLOY SYSTEM

A. NEDELICU, V. CRISAN*

ABSTRACT. The magnetic properties as function of atomic volume and the environmental effect for Mn_xNi_{1-x} alloy system have been studied in the compositional range $0.20 < x < 0.3$. A strong effect of chemical ordering on the magnetic structure was found. The ferromagnetic ordering is favorite by chemical disorder while a magnetic and/or chemical ordering lead to a spin flip of Mn magnetic moment especially when the atoms forms a L_{12} symmetry for spins or chemical composition. The AF states are of the DLM form for $x < 0.20$.

Keywords: *alloys, ferromagnetism, KKR-CPA, short range order, disordered local moment model*

1. Introduction The interest in the NiMn system has been extended considerably and a reasonable amount of both experimental and theoretical effort has been devoted to the transitions between (or co-existence of) ferromagnetic and spin glass behavior [1]. As well as FeNi, the MnNi alloys have INVAR properties for $0.6 < x < 0.8$ [2,3]. For the magnetic recording sensors the MnNi-based spin valve is also interesting due to AF coupling which is maintaining at very high temperature, much higher than other AF materials.

In this report we have investigating the magnetic and chemical ordering for Mn_xNi_{1-x} alloys in the concentration range of $0.2 < x < 0.30$. There is a definite preference, in MnNi alloys, for Ni atoms to have more Mn atoms as first and third neighbors than is required for complete randomness whilst the preference at second- neighbor positions is for like Ni atoms [4]. The introduction of Ni into the Mn matrix induces a form of short-range order whereby the Ni atoms prefer a Mn-rich environment across the whole composition range of the phase diagram. This general trend is not valid at least for 35at%Mn. Introduction of Ni in the Mn matrix induces a charge perturbation via the conduction electrons. For small Ni concentration very little short range order is expected but further introduction of Ni atoms induces further charge density perturbations and the alloys will show further amounts of local ordering [4]

In the present calculation for chemical ordering only the first nearest neighbors was taken into account.

* Faculty of Physics, Babes-Bolyai University, Kogalniceanu 1, Cluj Napoca

2. Method of computation. The total energy and the magnetic moments were calculated by using the KKR-CPA method in conjunction with the disordered local moment(DLM) model as was introduced by Jo and Akai[5,6] .

Standard KKR band structure calculation is performed by finding the zero of the determinant of the KKR matrix for each \vec{k}

$$\det |\delta_{LL'} - t_L(E)g_{LL'}(\vec{k}; E)| = 0 \quad (1)$$

where g is the structural Green function. and the t matrix is denoted as usual.

The procedure gives the energy eigenvalues as a function of \vec{k} and hence determines an energy dispersion relation $E(k)$.

The relativistic effects are taken into account within the scalar relativistic approximation [7].

In the DLM model two distinct magnetic states are allowed for the same atomic species in the metallic system. In this paper we have extended the DLM model to many subtleties (MS). The fcc crystalline structure was described as a simple cubic with 4 atoms (A, B, C, D) and the structure is considered as described by two sublattices one formed by one atom situated at the corner of cube – (atoms A), denoted by I, and the other formed by 3 atoms (B, C and D) located at faces, denoted by II as is shown in Figure 1. In these two sublattices the atoms are allowed to have different magnetic properties. In other words the compound chemical formula is $Ni_{s\uparrow}Ni_{p\uparrow}Mn_{d\uparrow}Mn_{f\downarrow}$, with $s+p=1-x$ and $d+f=x$. for each lattice site. The atoms located in sites I and II can be considered as having identical or different properties such as to describe the $L1_0$, $L1_2$ or AuCu I structures.

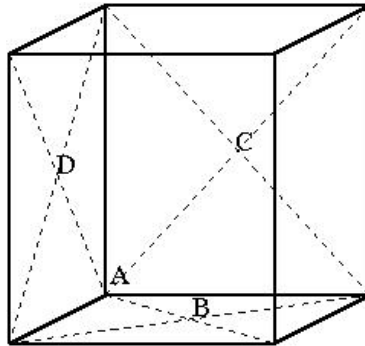


Figure 1. The fcc unit cell used for calculations is considered as a simple cubic with one atom located in origin and denoted by A and 3 atoms located on faces (B,C,D) forming the sublattice II. Imposing the constraint that the atoms in the sublattice II to be equivalents but different from those of sublattice I it is obtained the $L1_2$ structure. When the atoms from the two sublattices are equivalents the structure is of $L1_0$ type. The layered AuCu I structure is described by imposing the atoms in each layer perpendicular to Oz axis to have the same properties i.e. to contain the same CPA atoms.

For exchange and correlation the Moruzzi and Janak parameterization [8] was used.

3. Results and discussions. Neutron scattering measurements [9] show that when Mn is added dilutely to Ni the resulting magnetic disturbance occurs at the impurity atom sites. In pure metals the Mn atoms are very sensitive to the volume. Moreover the Mn atoms show the magnetovolume effect which is not present in the pure Ni crystal as is seen in Figure 2.

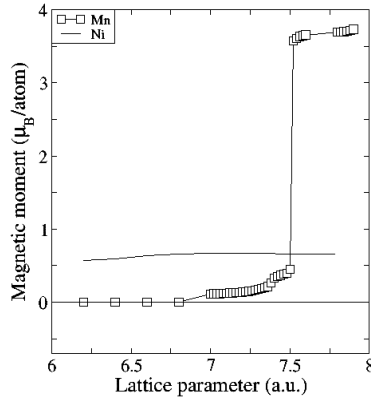


Figure 2. Magnetic moment of Mn and Ni pure crystals as function of fcc lattice parameter. The Ni magnetic moment remains constant in the region of the magnetovolume effect of Mn atom.

The computed density of states for diluted $x=0.01$ Mn alloy is shown in Figure 3.

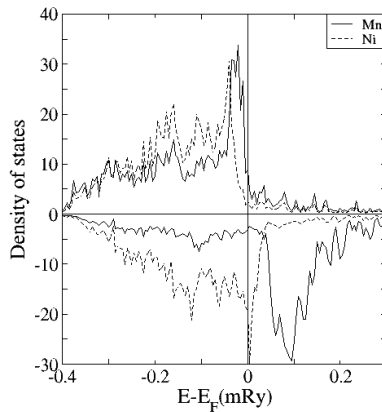


Figure 3. Density of states for 0.01at%Mn alloy. The upper curves are for spin up while the negative curves to the spin down. Vertical line at $E=E_F$ represent the Fermi level.

The density of states (DOS) in Figure 3. shows the DOS per atom for very small amount of Mn ($x=0.01$) which means also a very small contribution to the total magnetic moment of the alloy. It was shown [10] that by increasing Mn concentration, in the ferromagnetic region of the MnNi alloy system the relative position of the Mn and Ni bands are not changing. The only modifications will be the weight of each component in formula unit. It seems that the effect of adding more Mn atoms in the Ni matrix is completely additive [11] at list for $x < 0.2$. where the onset of FM ordering occur.

The total energy for $x=0.2$ is shown in Figure 4.

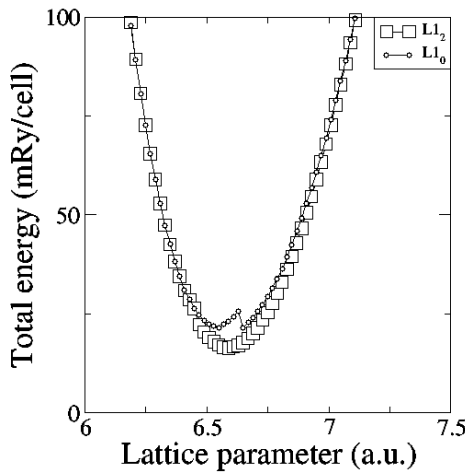


Figure 4. Total energy for $x=0.2$, $L1_0$ and $L1_2$ symmetries. The low moment low volume low moment to high moment high volume transition for $L1_0$ symmetry is close to the equilibrium volume corresponding to the $L1_2$ symmetry. The ordered $L1_2$ spin structure is more stable than the $L1_0$ one for the whole range of lattice parameter.

The $L1_0$ correspond to the completely disordered system which favor the FM ordering while $L1_2$ a DLM structure, (as is seen in Figure 5), represent the ground state of the system.

The magnetic moment for each atom and for the unit cell are shown in Figure 5.

It is seen that in the corner of the unit cell the spin Mn atoms are coupled AF to other Mn or Ni atom spins located in sublattice II. When the site is occupied by Ni atoms the coupling with atoms from sublattice II is still FM which is in agreement with the AF ordering tendency of Mn atoms. Also seen is the magnetovolume

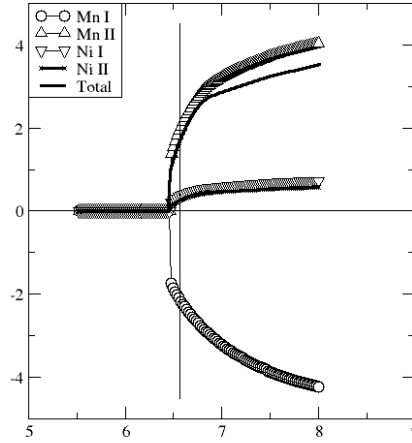


Figure 5. The total and atomic magnetic moments for $x=0.2$, $L1_2$ alloy. The vertical line correspond to the theoretical lattice parameter (minimum of the total energy, Fig.4).

effect on the Ni atom at the same volume as for Mn one. The lattice parameter for the magnetovolume effect is lower than in pure Mn crystal and appear also for Ni atoms. The low magnetic state correspond to vanishing atomic moments for both Mn and Ni atoms. No spin-glass like states were found.

Increasing the Mn content by a small value, to $x=0.25$ the magnetic ordering seems to remain unchanged. The total energy curves are shown in Figure 6.

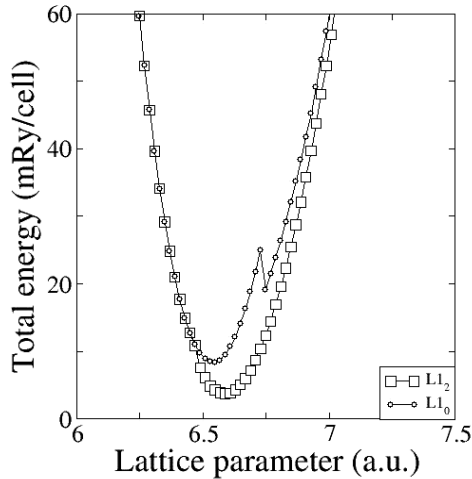


Figure 6. Total energy for $x=0.25$ and spin structure $L1_0$ and $L1_2$.

4. Conclusion. The results of calculations show that the onset of FM ordering appears at 0.2at%Mn. The alloys with lower concentration of Mn the magnetic ordering FM. The symmetry considered for calculations are both $L1_0$ and $L1_2$. Starting with 0.25at% Mn the $L1_2$ spin symmetry is lower in energy than the random spin structure. Using a chemical ordering parameter as was defined in ref.[12] by increasing the Ni concentration in sublattice II the total energy is further lowering. But different from FeNi case the minimum of the energy correspond to the same lattice parameter i.e. the dependence of equilibrium lattice parameter on chemical ordering doesn't exist. For lattice parameters lower than the equilibrium one the HS and LS states have the same energy. Starting from high lattice parameter the $L1_2$ is lower in energy than $L1_0$. Approaching the equilibrium state the symmetry of the spin system is changing from $L1_0$ to $L1_2$.

The theoretical lattice parameters are lower than the experimental ones because of LDA we have use for calculations. Moreover the half field orbitals of alloy atoms it was shown to further lowering the theoretical lattice parameter. The magnetic moment of Ni is larger than the experimental one because of scalar relativistic approximation.

ACKNOWLEDGEMENT

The author express thanks to H. Akai for providing the KKR-CPA code.

REFERENCES

1. O. Moze, E.J. Lindley, B.D. Rainford, J.M.M.M., 53 167 (1985)
2. M. Podgorny, Phys. Rev. 45, 797 (1992)
3. G. Hausch, Phys. Stat. Sol. (a) 41, K35 (1977)
4. O. Mozet and T J Hicks, J. Phys. F: Met. Phys. **14** (1984) 21 1-220.
5. T. Jo, J. Phys. Soc. Jpn, 51, 794 (1982)
6. H. Akai, P. H. Dederichs, Phys. Rev.,B47,8739(1993)
7. D. D. Koelling and B. N. Harmon, J. Phys. C 10, 3107 (1977)
8. V. L. Moruzzi, J. F. Janak, A. R. Williams, *Calculated electronic Properties of Metals* (Pergamon, New York, 1978)
9. G. G. E. Low, M. F. Collins, J. Appl. Phys. 34, 1195 (1963)
10. A.Nedelcu, V.Crisan to be published
11. O. Moze, T J Hicks, J. M. M. M., J. Phys. F: Met. Phys. 14 , 221(1984)
12. V. Crisan, P.Entel, H.Ebert, H.Akai, D.D. Johnson, J. B. Staunton Phys.Rev.,B 66, 014416 (2002)

XPS INVESTIGATION OF THE ATOMIC ENVIRONMENT IN BINARY BORON-BISMUTHATE GLASSES

B. OPREA*, T. RADU, S. SIMON

ABSTRACT. X-ray photoelectron spectroscopy (XPS) was employed to investigate B_2O_3 - Bi_2O_3 vitreous samples with different of B/Bi ratios, considering the large interest for heavy-metal glasses based on Bi_2O_3 oxide present in field of optical and electronic devices. The glass samples have been prepared by melting technique. From the analysis of the XPS spectra for the Bi 4*p*, B 1*s* and O 1*s* core levels, several changes are identified in terms of various structural units being present, reflected by the changes occurred in the atomic environments of bismuth and boron atoms. All O 1*s* spectra were deconvoluted into two Lorentzian-Gaussian peaks corresponding to bridging and non-bridging oxygen atoms and the variation in the ratio of their peak areas is discussed in terms of the local structure as well.

Keywords: borate glasses; heavy metal glasses; XPS.

1. Introduction

There is an increasing interest for heavy-metal glasses based on Bi_2O_3 oxide due to their properties that led to applications in field of optical and electronic devices, thermal and mechanical sensors and reflecting windows [1-4].

Because of the weak field strength of Bi^{3+} ions, bismuth oxide can not be considered as glass network former, however, in combination with B_2O_3 is possible to form glasses in a wide range of compositions. According to Krogh-Moe [5], B_2O_3 vitreous structure consists of a random network boroxol rings and BO_3 triangles connected by links B-O-B, and the addition of other oxides causes a progressive change of boron atoms coordination from 3 to 4 and result in the formation of cyclic variables units such as groups diborate, triborate or tetraborate. In the region of small amounts of modifier, units are grouped to form BO_4 triborate units, while by increasing the oxide content in borate glasses boron units are predominantly associated BO_4 diborate groups [6]. Although much work has been done on studying the structural properties of B_2O_3 - Bi_2O_3 glasses, there still remain many controversies and doubts about the atomic level structure and its correlation with the macroscopic properties [3, 7].

* Babeş-Bolyai University, Faculty of Physics & Institute of Interdisciplinary Research in Bio-Nano-Sciences, 400084 Cluj-Napoca, Romania

This paper reports XPS results reflecting atomic environment in B_2O_3 - Bi_2O_3 glasses with different of B/Bi ratios. It is worth to mention that the examined systems are very interesting because of the presence of two oxides formers glass network, one classical B_2O_3 and one unconventional Bi_2O_3 . From the analysis of the XPS spectra for the Bi 4*p*, B 1*s* and O 1*s* core levels, several changes are identified in terms of various structural units being present, reflected by the changes occurred in the atomic environments of bismuth and boron atoms.

2. Experimental Procedure

Glass samples belonging to $(1-x)B_2O_3 \cdot xBi_2O_3$ system ($0.1 \leq x \leq 0.875$) were prepared using as starting materials H_3BO_3 and $Bi(NO_3)_3 \cdot 5H_2O$ of reagent purity grade. The mixtures were melted in air, in sintered corundum crucibles introduced into an electric furnace at 1100°C for 15 minutes. The melts were quickly undercooled at room temperature by pouring and pressing between stainless steel plates. X-ray diffraction analysis did not reveal any crystalline phase.

The XPS measurements were performed using a SPECS PHOIBOS 150 MCD spectrometer with monochromatic AlK_{α} source (250 W, $h\nu=1486.6$ eV), and 10^{-9} - 10^{-10} mBar vacuum in the analysis chamber. A low energy (< 5 eV) electron beam delivered by a flood gun was used to achieve charge neutrality at the sample surface. The absolute binding energies of the photoelectron spectra were determined by referencing to the C 1*s* transition at 284.6 eV that results most probably during the measurements as adsorbed species. The position and full width at half maximum of photoelectron peaks were estimated using spectra simulation based on summation of Lorentzian and Gaussian functions.

3. Results and Discussion

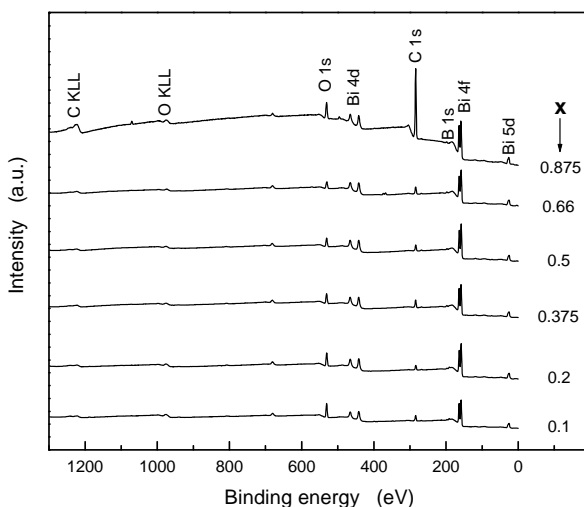
In the entire compositional range the samples were obtained in vitreous state, nevertheless the B/Bi ratio decreased from 9:1 to 1:7. Due to boron high field strength and bond strength with oxygen (Table 1), B_2O_3 is one of the most common glass former. The addition of other oxides changes the boron coordination that results in the formation of cyclic units like diborate, triborate or tetraborate groups [5]. The nonconventional glass forming oxide Bi_2O_3 can participate in the glass structure either with pyramidal or octahedral units. As the number of bismuth atoms exceeds the total number of cations in the glass network, a heavy metal glass is obtained, with properties that are mainly due to the high polarisability and the relatively low field strengths of heavy metal cations as compared to conventional glass formers (Table 1).

Table 1.

Ionic radius, coordination type, ionic field strength, single bond strength with oxygen and electronegativity of the cations entering in $(1-x)\text{B}_2\text{O}_3 \cdot x\text{Bi}_2\text{O}_3$ glasses.

Cation	Coordination number	Shannon ionic radius [9, 10] (Å)	Cation field strength (\AA^{-2})	Electronegativity (Pauling units)	Single bond strength M-O ($\text{kJ}\cdot\text{mol}^{-1}$) M-O bond strength [11] kJ/mol
Bi^{3+}	6	1.17	2.19	2.02	337.2 ± 12.6
	8	1.31	1.75		
B^{3+}	4	0.25	48	2.04	808.8 ± 20.9
	6	0.41	17.84		

Energy peaks in the survey scans allowed to identify the atomic species occurring in the uppermost ~ 10 nm layer of the analyzed samples. Detection limits are approximately 0.1 atom percent for most elements. The concentrations of the elements identified in the survey spectra (Fig. 1) were determined by integrating the area under the characteristic peak for each element and considering sensitivity factors to the photoelectron peaks. One observes a good linear dependence (Fig. 2) on bismuth content at surface of B_2O_3 - Bi_2O_3 glasses as B/Bi ratio takes values in the range between $9/1$ ($x=0.1$) and $1/7$ ($x=0.875$).

**Fig. 1.** XPS survey spectra of $(1-x)\text{B}_2\text{O}_3 \cdot x\text{Bi}_2\text{O}_3$ glasses

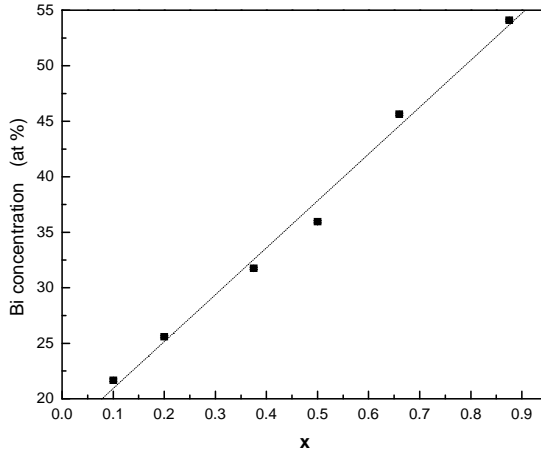


Fig. 2. Bismuth concentration on the surface of $(1-x)\text{B}_2\text{O}_3\text{-}x\text{Bi}_2\text{O}_3$ glasses

By using the high resolution multiple scan one can evaluate the chemical states of each element through its core electron binding energies. The core electrons feel an alteration in the chemical environment when a change in the potential (charge distribution) of the valence shell occurs.

The Bi 4f photoelectron core level spectra are shown in Fig. 3. The spin orbit splitting is very close to 5.3 eV. The binding energy of Bi 4f_{5/2} increases from 163.7 eV for x=0.1 to 164.05 eV for x=0.875, that may be related with an increasing polarisation of bismuth and implicitly of the covalence degree of Bi–O–B bonds [12]. The decrease in effective electronic charge density around the bismuth cations would be reflected in an increase in the binding energy of the remaining electrons [13].

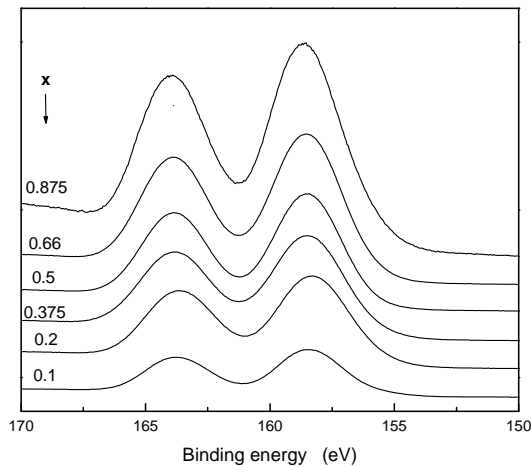


Fig. 3. High resolution Bi 4f core level photoelectron spectra for $(1-x)\text{B}_2\text{O}_3\text{-}x\text{Bi}_2\text{O}_3$ glasses.

Precise determination of binding energies is made through the use of curve fitting routines applied to the peaks. Shifts in the binding energy can result from the atom's oxidation state, chemical bonds, or crystal structure. By using an available database it is possible to identify the binding energies with specific compounds.

It is well known that the boron compounds have a number of remarkable properties originating from the small core size and the absence of *p* electrons in boron. In our compounds, because of the presence of O one would expect that the peak position of B (*1s*) may result in its shift. The peak at ~ 191.1 eV observed in the core level spectra (Fig. 4) could be ascribed to B in these compounds. It may be observed that B *1s* peak, for $x=0.1$, has a second structure at ~ 197.5 eV.

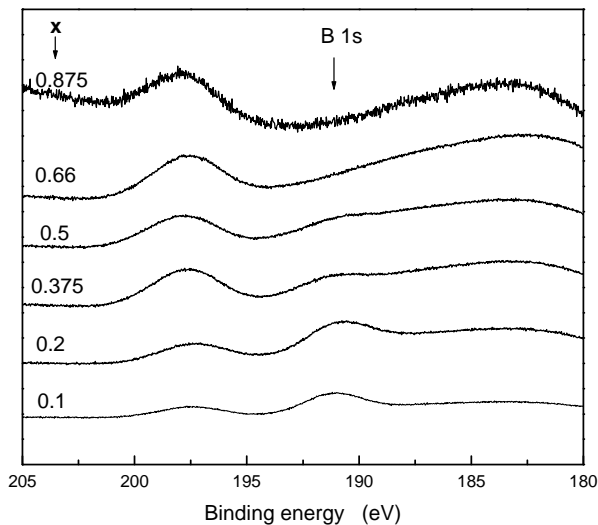


Fig. 4. High resolution B *1s* core level photoelectron spectra for for $(1-x)\text{B}_2\text{O}_3 \cdot x\text{Bi}_2\text{O}_3$ glasses

With increasing of the bismuth content, the peak observed at high energies increases, while B *1s* peak intensity decreases continuously and eventually for $x=0.875$ vanishes (Fig. 4). The peak for B *1s* may overlap with the inelastic scattering tail that occurs before the photoemission peak of Bi. Fig. 4 shows that this tail increases with increasing the Bi concentration up to the $x=0.875$ sample. Actually, for this particular concentration, the O *1s* peak is broadening (Fig. 5), and the FWHM has the maximum value among the studied samples (Fig. 6). This effect, cannot be associated with the charging effect, since during the measurement a charge neutralizer was used, in order to align the C peak position, therefore being awarded local structural effects produced by partial substitution of boron by bismuth. This is a suggestion that this substitution increases the degree of structural disorder around the oxygen.

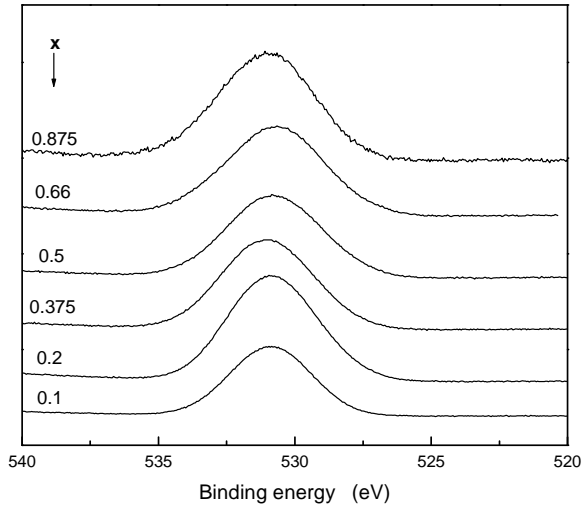


Fig. 5. High resolution O 1s core level photoelectron spectra for for $(1-x)\text{B}_2\text{O}_3 \cdot x\text{Bi}_2\text{O}_3$ glasses

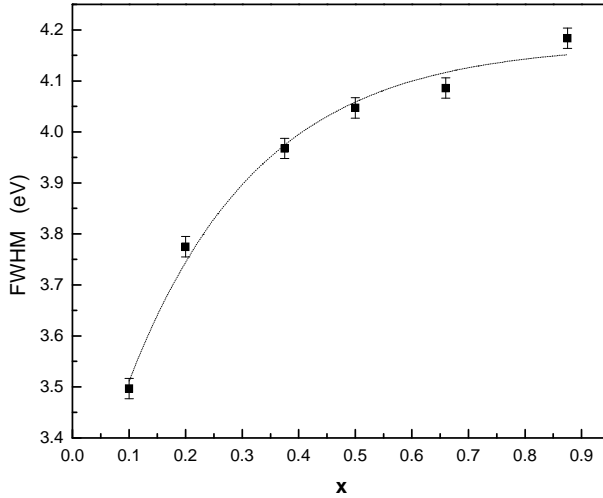


Fig. 6. Composition dependence of O 1s photoelectron peak full width at half maximum (FWHM) for $(1-x)\text{B}_2\text{O}_3 \cdot x\text{Bi}_2\text{O}_3$ glasses

All O 1s spectra were deconvoluted into two Lorentzian-Gaussian peaks (Fig. 7) corresponding to bridging and non-bridging oxygen atoms and the variation in

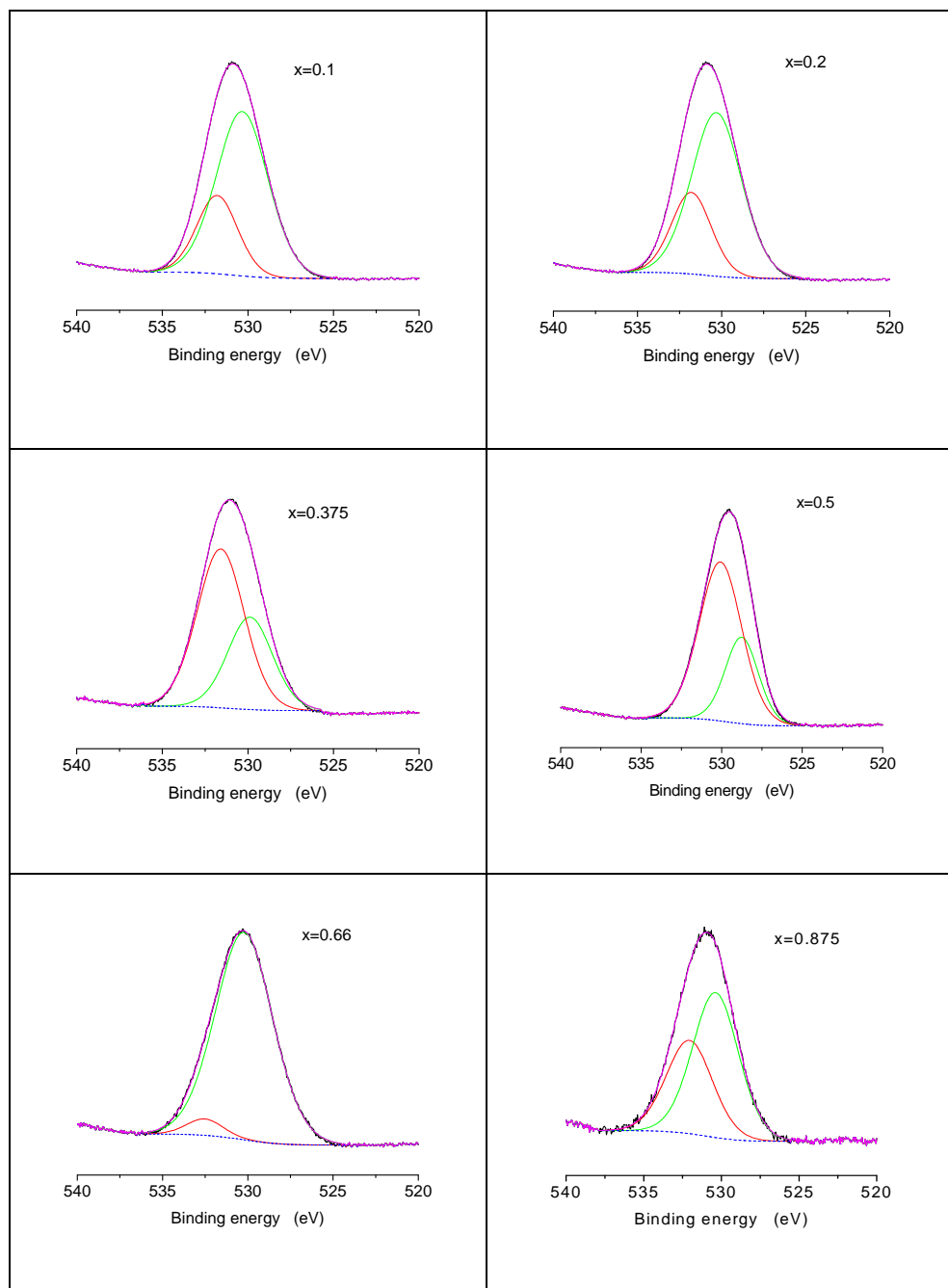


Fig. 7. Deconvolution of the O 1s photoelectron peak of the analysed samples

the ratio of their peak areas is discussed in terms of the local structure as well [8]. Specifically, the binding energy of the O 1s electrons inform on the measure of the extent to which electrons are localized on the oxygen or in the internuclear region, a direct consequence of the nature of the bonding between the oxygen and different cations. The percentage of bridging and non-bridging oxygen atoms, as determined from the deconvolution of the O 1s high resolution spectra is given in Table 2. The local structure of high borate sample (B/Bi = 9/1; 4/1) and of high bismuhate samples (B/Bi = 1/7) is realised with a large number of non-bridging oxygens, while in the middle composition range ($1/1 \leq \text{B/Bi} \leq 5/3$), the preponderance of bridging oxygens is noticed. The increase in electron density at the oxygen atoms means that the electron binding energies are reduced and this is reflected in the O 1s photoelectron spectrum, giving rise to non-bridging oxygen peak.

Table 2.

The percentage of bridging (BO) and non-bridging (NBO) oxygen atoms in $(1-x)\text{B}_2\text{O}_3 \cdot x\text{Bi}_2\text{O}_3$ glasses

x	0.1	0.2	0.375	0.5	0.66	0.875
O _{BO}	28.83	29.13	66.91	73.61	4.70	38.44
O _{NBO}	71.17	70.87	33.09	26.39	95.30	61.56

4. Conclusions

The analysis of XPS spectra of Bi 4f, B 1s and O 1s suggest several changes that consist in the presence of various structural units around B, Bi and O atoms. The deconvolution of the O 1s spectra provides the O_{BO}/O_{NBO} ratio as a function of the Bi₂O₃ content. The O_{BO}/O_{NBO} dependence on diminishing B/Bi ratio points out an increased polarisability of bismuth atoms and their role of glass network former.

For all the studied samples we observed an additional structure in the B high resolution spectra of the as prepared sample at high energy (~ 197.5 eV) attributed to B atoms located in defective regions, and surely out of its electronic sp¹ configuration. In order to clarify the origin of this experimental observation we have to check the behavior of this peak as a consequence of the sample mechanical and thermal treatment: creating or destroying the crystalline/molecular order. This imposes further XRD and XPS measurements on thermal treated and milled samples in order to complete the characterization of the structural order in both surface and bulk of the samples.

ACKNOWLEDGEMENT

This research was supported by the Romanian National University Research Council – CNCSIS under PNII Idei PCCE-129 /2008 grant.

REFERENCES

1. C. Stehle, C. Vira, D. Vira, D. Hogan, S. Feller, M. Affatigato, *Phys. Chem. Glasses*, **39**, 2 (1998) 83.
2. R. Stefan, S. Simion, *Mod. Phys. Lett. B*, **15**, 3 (2000) 111.
3. H. Fan, G. Gao, G. Wang, L. Hu, *Solid State Sci.*, **12** (2010) 541.
4. V. Simon, O. Ponta, S. Simon, M. Neumann, *J. Optoelectr. Adv. Mater.*, **10**, 9 (2008) 2325.
5. R.L. Mozzi, B.E. Warren, *J. Appl. Crystallogr.*, **3** (1970) 251.
6. L. Baia, R. Stefan, W. Kiefer, J. Popp, S. Simion, *J. Non-Cryst. Solids*, **303** (2002) 379.
7. V. Dimitrov, T. Komatsu, *J. Non-Cryst. Solids*, **356** (2010) 258.
8. G.D. Khattak, N. Tabet, L. E. Wenger, *Phys. Rev. B*, **72**, 10 (2005) 104203.
9. R.D. Shannon, *Acta Cryst.*, **A32** (1976) 751.
10. J.E. Huheey, E.A. Keiter, R.L. Keiter in *Inorganic Chemistry: Principles of Structure and Reactivity*, 4th edition, HarperCollins, New York, USA, 1993.
11. J.A. Kerr in *CRC Handbook of Chemistry and Physics*, D.R. Lide, (ed.) CRC Press, Boca Raton, Florida, USA, 81-st ed., 2000.
12. V. Simon, H. Bako-Szilagyi, M. Neumann, S.G. Chiuzbaian, S. Simon, *Mod. Phys. Lett. B*, **17**, 7 (2003) 291.
13. V. Simon, D. Eniu, A. Takacs, K. Magyari, M. Neumann, S. Simon, *J. Non-Cryst. Solids*, **351** (2005) 2365.

SYNTHESIS AND CHARACTERISATION OF THE 55SiO₂·41CaO·4P₂O₅ SOL-GEL DERIVED BIOGLASS

A. SILAGHI*, V. SIMON*

ABSTRACT. This article presents the synthesis process of samples derived from a sol gel prepared bioglass with the particular composition of 55SiO₂·41CaO·4P₂O₅ and the effects of heat treatment parameters on their structural properties. The samples were analyzed with respect to composition, cristallinity and morphology through SEM, EDX, XRD, DTA and FT-IR spectroscopy. Differences in the thermal treatment of the samples prove the importance of proper aging and slow temperature rise during drying.

Keywords: bioactive glass; sol-gel; heat treatment; structure; morphology.

INTRODUCTION

Biomaterials are generally tailored for specific applications. Therefore the selection of a certain material depends primarily on the requirements of its specific function. The first generation of biomaterials was aimed at achieving the most bioinert materials possible. Avoiding any interaction with the surrounding tissue helped prevent inflammation and subsequent cell necrosis at the interface of the material with the biological medium. The discovery of bioactive glasses has revolutionized the field of biomaterials by presenting the possibility to use the materials interaction with its medium to the advantage of the patient. The main feature of this material is its capacity to bind to the surrounding tissue without causing inflammation. Though some bioglasses are able to bind to soft tissues, their primary use remains targeted at applications involving hard tissues such as bones. After implantation, the surface of bioactive glass remodels to form hydroxy-carbonate apatite (HCA), the chemical and structural equivalent of bone mineral. Furthermore, bone growth markers and bone repair cells are increased in the presence of bioactive glass [1], thus accelerating the overall healing process.

The key composition features of Bioglass® [2] is that it contains less than 60 mol% SiO₂, high Na₂O and/or CaO contents, high CaO/P₂O₅ ratio, which are responsible in making Bioglass® highly reactive to aqueous medium and bioactive. It is important to mention that small changes in the composition can lead to very

* Babes-Bolyai University, Faculty of Physics & Institute of Interdisciplinary Research in Bio-Nano-Sciences, 400084 Cluj-Napoca, Romania

different properties. Therefore different compositions are continuously being tested in order to assess the properties of new bioactive glasses and based on these determine their possible applications.

The sol-gel method has become widely spread, partly due to its ease of use, but initially mostly because of its capacity to produce a large variety of inorganic networks and later hybrid structures using organic and inorganic precursors. It provides a new approach to preparation of glasses and ceramics with a series of advantages over conventional methods [3-5].

EXPERIMENTAL

Synthesis of the bioglass

The desired composition for this specific bioglass, obeying the general rules of bioactive glass formation, has been chosen to be $55 SiO_2 \cdot 41 CaO \cdot 4 P_2O_5$. The precursors were tetraethoxysilane $Si(OC_2H_5)_4$ (TEOS), diammonium phosphate $(NH_4)_2 HPO_4$ and calcium chloride $CaCl_2$. The bioglass was prepared using the standard sol-gel processing steps [4]. A schematization of the entire preparation process is shown in Fig. 1

Mixing. The needed amounts of precursors were dissolved as follows (every procedure was carried out over a hot plate). $CaCl_2$ and $(NH_4)_2 HPO_4$ were dissolved in distilled water. TEOS was mixed with distilled water at a ratio of 1:1. A few drops of HCl were subsequently added to the TEOS solution until it became clear. The $CaCl_2$ solution was added to this while stirring, followed by the $(NH_4)_2 HPO_4$ solution.

Gelation. The obtained mixture was stirred continuously. In order to promote its gelation a small quantity of NH_3 was added. The resulting gel showed a milky coloration.

Aging. From the obtained gel, a part was removed and denied the process of aging by directly drying and sintering, while the remaining material was allowed to age for one day.

Drying and Sintering. Part of the gel was inserted without aging into a pre-heated oven at $600^\circ C$ for a few seconds. The thermal shock proved to be very strong; the container holding cracked, but it did not brittle and therefore the sample was not contaminated.

The remaining material was divided into three parts after aging, and thermal treatment was induced gradually. The increase in temperature was carried out with $10^\circ C$ /minute. The first part was dried at $110^\circ C$ for 24h, the second at $300^\circ C$ for 30min and the third at $500^\circ C$ for 30min.

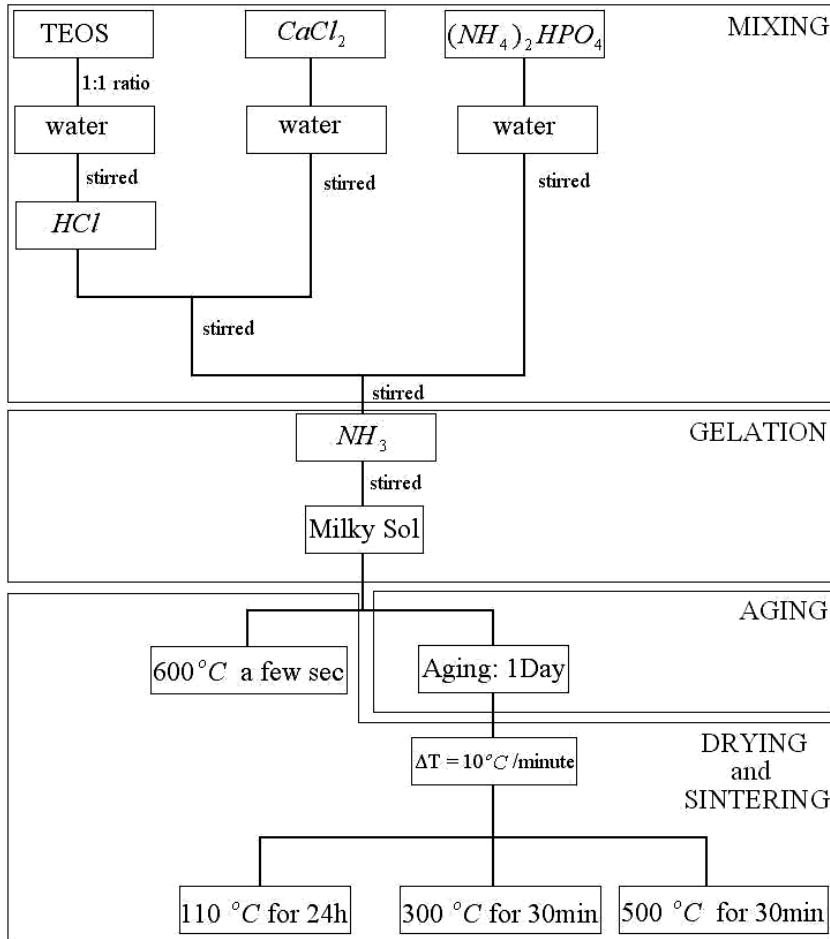


Fig. 1. Sol-gel processing steps of the prepared bioglass (mixing and gelation performed on a hot-plate).

Methods

The samples morphology, composition, crystallinity and structural units were analyzed through SEM, EDX, XRD, DTA and FT-IR spectroscopy.

SEM (Scanning Electron Microscopy) analysis followed the porosity of the bioglass after the applied heat treatment in order to determine the structural differences induced by this procedure. The dried bioglass was broken into small pieces. Coating was carried out without further action upon it (like grinding or compression) with a layer of Au and analyzed under the SEM. The apparatus used was a Quanta FEY 400

EDX (Energy Dispersive X-ray Spectroscopy) was applied to determine the elemental composition of the bioglass. The analysis was carried out with the help of an EDX module attached to the SEM. The analysis was carried out at the same time, upon the same sample sections as those shown above without any further intervention.

XRD (X-ray Diffraction) was used to analyse the structure of the obtained bioglass. The samples were grinded into fine powder before being analysed. The diffractometer used was Shimadzu XRD 6000.

DTA (Differential Thermal Analysis) thermoanalytic technique was applied in order to investigate endothermic or exothermic changes in the sample to gather data on the occurring transformations, such as desorption, decomposition, phase transitions, or cristallisation. A small amount of glass that was dried at 110°C was placed in the DTA apparatus and measured against the machines inert reference. A Shimadzu DTG 60h analyser was used.

FT-IR (Fourier Transform Infrared Spectroscopy) followed the identification of the structural units present in samples, based on the spectral locations of their IR absorptions.

Around 3mg of sample were grinded and mixed with KBr. The apparatus used was a Bruker Equinox 55 FTIR/FTNIR spectrometer.

RESULTS AND DISCUSSION

SEM (Scanning Electron Microscopy)

The differences noticed (Fig. 2) are that the porosity of the glass dried at 300°C for 30 min is greater than that of the same glass dried at 110°C for 24h. This is due to the fact that the 110°C dried sample still contained large amount of water. The increase in temperature to 500°C already shows that the material is beginning to compress. The larger porosity of the sample dried at 600°C is to be attributed to the facts that this sample has not been allowed to age and that its drying was not carried out in a step by step process but rather through a sudden thermal shock.

The greater magnification in Fig. 3 allows a closer observation at the cristallinity of the samples and the amount of residual glass present. We observe that with the increase of the thermal treatment temperature, there is a process of cristallisation and crystal growth in the bioglass. However the sample treated with a sudden thermal shock shows clearly an inferior structure to all others in terms of cristallisation. The samples show an apparently homogenous nucleation. The crystal growth seems to be non uniform lateral growth.

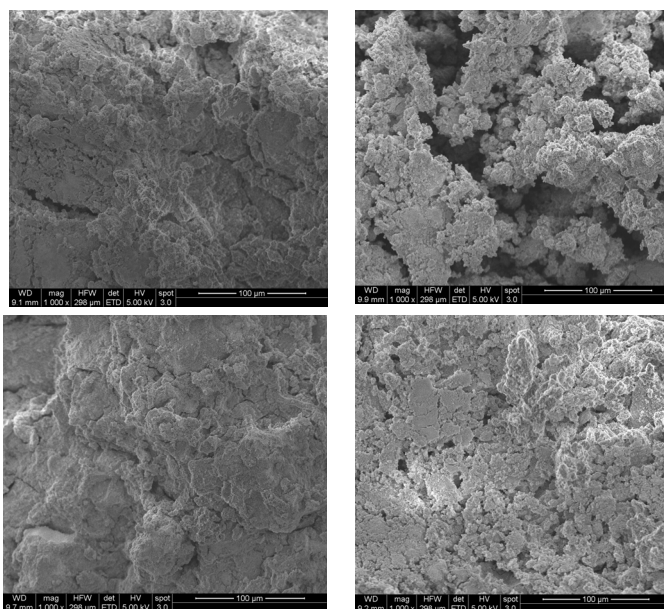


Fig. 2. SEM images of the bioglass; magnification 1000x; right to left, top to bottom: 110°C, 300°C, 500°C and 600°C.

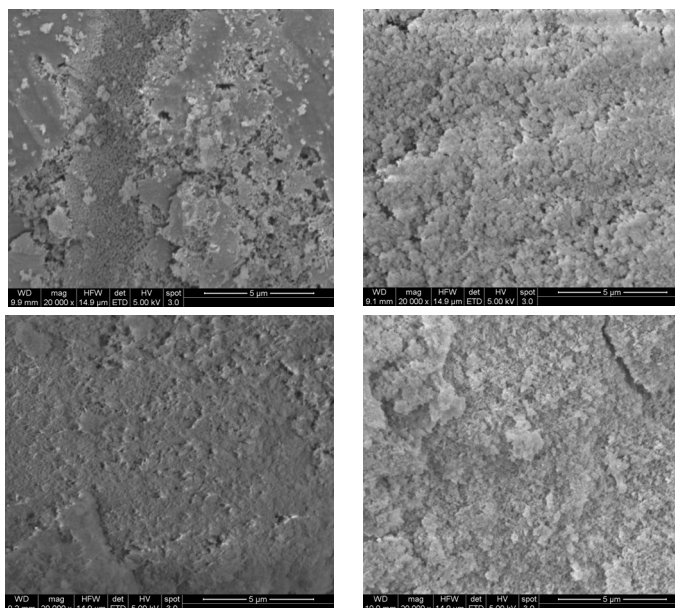


Fig. 3. SEM images of the bioglass; magnification 20.000x; right to left, top to bottom: 110°C, 300°C, 500°C and 600°C.

EDX (Energy Dispersive X-ray Spectroscopy)

Fig. 4 presents the elemental composition of the four samples. It can be noticed that no peaks indicate any impurity level and that all elements expected to be present are accordingly. By comparing the ratios between the elements present in every single analysis there is no deviation to be seen. The ratio between Cl and Ca tends to decrease with the rise of treatment temperature.

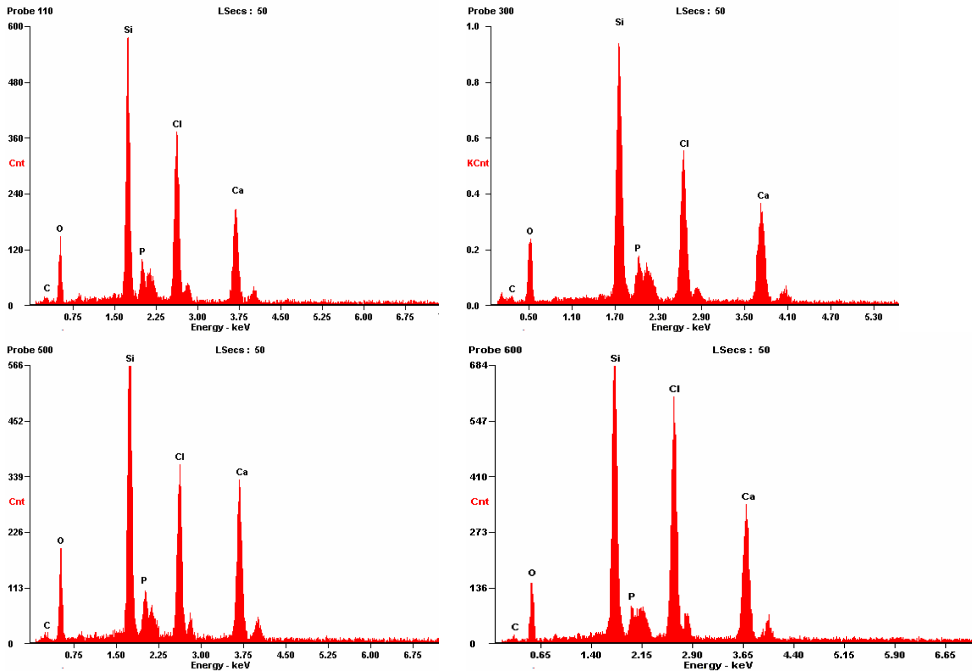


Fig. 4. EDX spectra of the samples. Left to right, top to bottom: 110°C , 300°C , 500°C and 600°C

XRD (X-ray Diffraction)

The XRD diffraction patterns (Fig. 5) show for all samples beside the amorphous phase the presence of a nanocrystalline structure. The nanostructure is significant for biomaterials because small crystallites are responsible for better protein absorption [6] and implicitly contribute to their biocompatibility. It can be noticed that the amorphous phase largely dominates the structure of the sample dried without aging at 600°C .

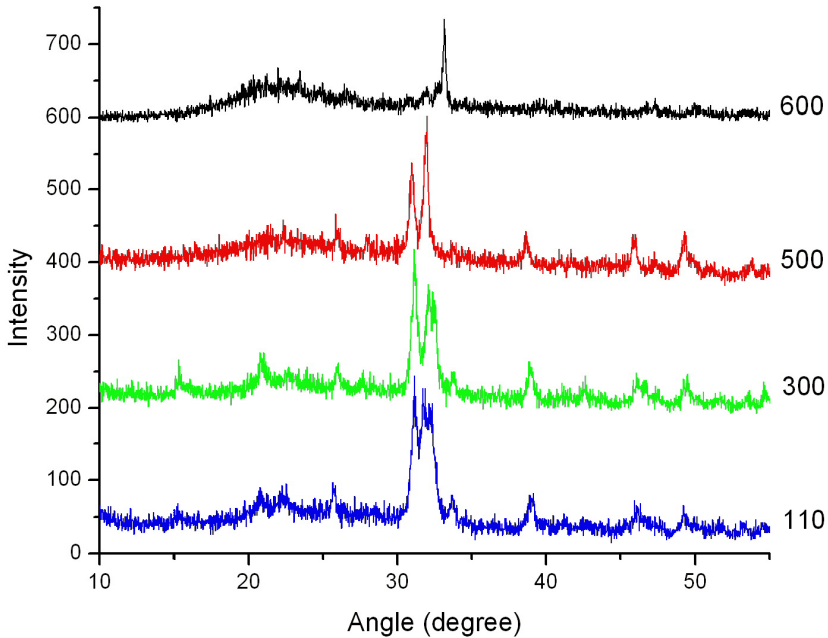


Fig. 5. XRD patterns of the bioglass samples.

The peaks recorded at 2θ angles close to 31, 32, 39, 46, 49 degrees in the samples treated up to 500 °C denote the presence of hydroxylapatite $Ca_5(PO_4)_3(OH)$ [7].

The sample dried at 600 °C presents a single outstanding peak at around 33°, which does not occur in the diffraction patterns of the other samples. Due to the fact that at such high temperatures the OH bonds have been removed, this peak is to be attributed to another type of apatite, like calcium chloride phosphate chlorapatite $Ca_5(PO_4)_3Cl$.

DTA (Differential Thermal Analysis)

The endothermic peak at 80.4 °C (Fig. 6) is accompanied by a loss of mass of 12 %. This can be attributed to the removal of free water that was still present at the surface of the sample. The endothermic peaks at 215 °C and 294.6 °C are related to mass losses of 6 % and 8 %, due to the removal of water molecules which were adsorbed or caged in the pores of the sample. The mass loss of about 12 % recorded at higher temperatures is assigned to the elimination of hydroxyl groups.

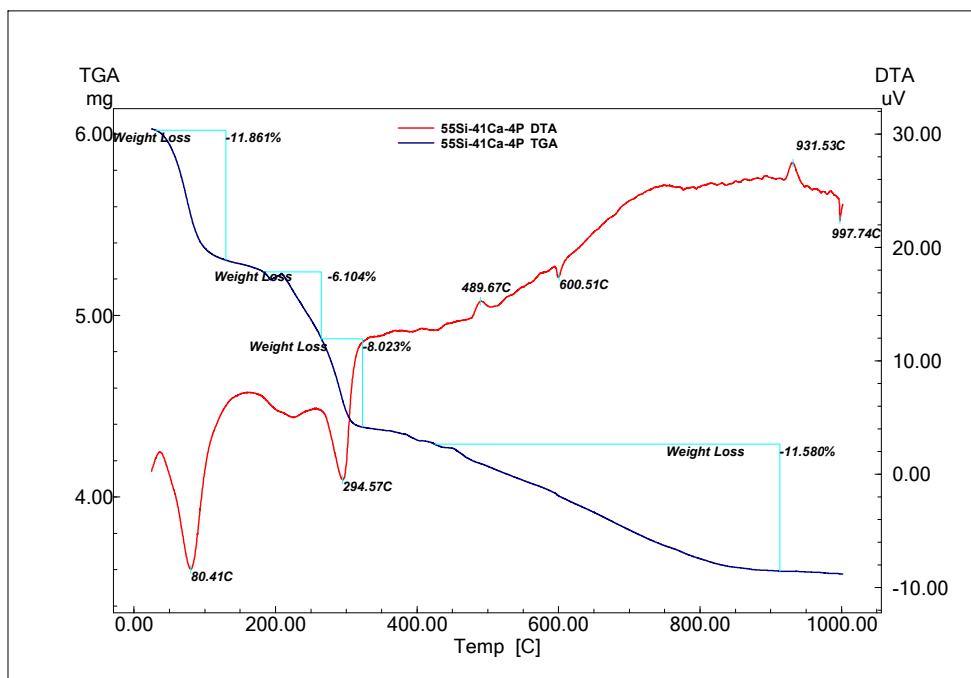


Fig. 6. DTA pattern of the bioglass sample dried at 110°C .

The pairs of exo-endo peaks at 489-600 °C and 931-997 °C are artefacts and bear no further significance.

FT-IR (Fourier Transform Infrared Spectroscopy)

The complex FT-IR spectra of the bioglass samples (Fig. 7) reveal that the bands in the region $1200\text{-}900\text{ cm}^{-1}$ include IR absorption due to both PO_4 and SiO_4 groups. These tetrahedra can be grouped together by ‘bridging’ oxygens (BO). In fact, some of the oxygen atoms, the ‘non-bridging’ oxygens (NBO), are not directly connected to other structural units in the glass network, because of the presence of network modifier cations. Non-bridging oxygens are also related to hydroxyl groups that break the silicate network. It is very difficult to distinguish between the frequency of IR absorptions of each of these groups, and in the literature different hypotheses have been proposed [8-10]. Usually, in the presence of some NBOs, Si-O frequency reflected by IR absorption falls in the range $1040\text{-}940\text{ cm}^{-1}$. The investigated sample does indeed show bands in this range that can be thus attributed to these silicone bonds (at 1034 and 953 cm^{-1}). We attribute the

peak at 1204 cm^{-1} to Si-O-Si stretching vibration and the peak at 799 and 465 cm^{-1} to Si-O-Si bending vibrations. The IR absorption recorded at 1092 cm^{-1} corresponds to P-O stretching vibration and that at 607 and 565 cm^{-1} to the P-O bending vibration in PO_4^{-3} tetrahedra.

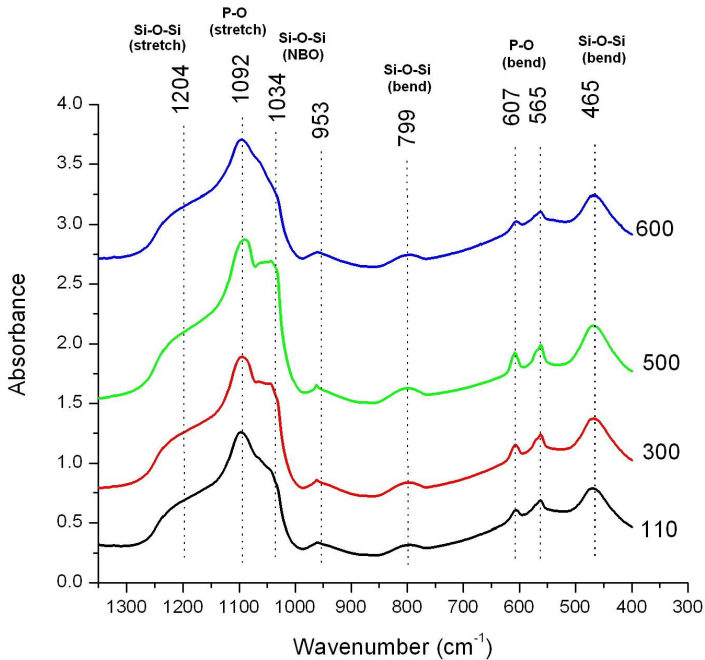


Fig. 7. FT-IR spectra of the bioglass samples.

CONCLUSIONS

The results regarding structural properties of the synthesised 55 SiO_2 · 41 CaO · 4 P_2O_5 bioglass samples show that they are promising in order to obtain biocompatibility. Differences in the thermal treatment of the samples prove the importance of proper aging and slow temperature increase rate during heat treatment. The sample treated at 500 °C exhibits better properties in terms of compactness, the sample treated at 300 °C shows the highest porosity, while the sample dried at 110 °C contains the highest amount of OH groups. Further research will focus on the bioactivity properties of this system.

ACKNOWLEDGEMENTS

A.S. author would like to thank E. Eitenberger from TU-Wien, Austria for support in SEM and EDX measurements, and Dr. M. Tamasan from ICIBNS of Babes Bolyai University for support in DTA and XRD measurements. This study was performed in the framework of PN II project PCCE 248/2008.

REFERENCES

1. J. Isaac, J. Nohra, J. Lao, E. Jallot, J.-M. Nedelec, A. Berdal, J.-M. Sautier, *Effects of strontium-doped bioactive glass on the differentiation of cultured osteogenic cells*, Eur. Cells Mater. 21, 130-143 (2011).
2. L.L. Hench, *The story of Bioglass®*, J. Mater. Sci. Mater. Med. 17 (11) 967-978 (2006).
3. P. Sepulveda, J. R. Jones, L. L. Hench, *In vitro dissolution of melt-derived 45S5 and sol-gel derived 58S bioactive glasses*, J. Biomed. Mater. Res.61(2) 301-311 (2002).
4. N. de la Rosa-Fox, M. Piñero, L. Esquivias, *Organic-Inorganic Hybrid Materials from Sonogels*, in Handbook of Organic-Inorganic Hybrid Materials and Nanocomposites. Stevenson Ranch, California, EE.UU. American Scientific Publishers, 2003, Vol. 2, pp. 241-270.
5. L.L. Hench, D.E. Day, W. Holand, V.M. Rheinberger, *Glass and Medicine*, Int. J. Appl. Glass Sci.1 (1) 104–117 (2010).
6. E. Fujii, M. Ohkubo, K. Tsuru, S.Hayakawa, A. Osaka, K. Kawabata, C. Bonhomme, F. Babonneau, *Selective protein adsorption property and characterization of nanocrystalline zinc-containing hydroxyapatite*, Acta Biomaterialia 2 (1) 69–74 (2006).
7. A.C. Tas, *X-ray diffraction data for flux-grown calcium hydroxyapatite whiskers*, Powder Diffr. 16 (2) 102-106 (2001).
8. I. Lebecq, F. Desanglois, A. Leriche, C. Follet-Houttemane, *Compositional dependence on the in vitro bioactivity of invert or conventional bioglasses in the Si-Ca-Na-P system*, J. Biomed. Mater. Res. A 3 (1) 156-168 (2007).
9. A. Balamurugan, G. Sockalingum, J. Michel, J. Fauré, V. Banchet, L. Wortham, S. Bouthors, D. Laurent-Maquin, G. Balossier, *Synthesis and characterisation of sol gel derived bioactive glass for biomedical applications*, Mater. Lett. 60, 3752–3757 (2006).
10. M. Sitarz, M. Handke, W. Mozgawa, *Identification of silicoxygen rings in SiO₂ based on IR spectra*, Spectrochim. Acta A 56 (9) 1819–1823 (2000).

XRD AND FTIR INVESTIGATION OF ZIRCONIA-TOUGHENED ALUMINA COMPOSITES

V. SIMON¹, S. CAVALU², I. AKIN³,
O. YUCEL³, G. GOLLER³

ABSTRACT. Structural effects induced by progressive addition of zirconia to monolithic $(100-x)\text{Al}_2\text{O}_3 \cdot x\text{ZrO}_2$ ($x \leq 30$ vol%) composites prepared by spark plasma sintering were investigated by X-ray diffraction (XRD) and Fourier Transform Infrared (FTIR) spectroscopy. The relative intensities of XRD peaks corresponding to alumina and zirconia are proportional to $\text{Al}_2\text{O}_3/\text{ZrO}_2$ ratio of the composite samples. FTIR results inform additionally on the changes occurred in the short range order structure of aluminum atoms in these alumina-zirconia composites.

Keywords: *zirconia-toughened alumina; XRD; FTIR.*

INTRODUCTION

Nowadays, an increasing interest in ceramics with potential applications in field of bone restoration is registered because they represent the newest generation of ceramic biomaterials for replacing metallic bearing parts in arthroplastic applications [1, 2]. This attracted investigation and development of new, strong and tough bioceramics using modern processing technologies [3, 4]. Ceramic composites are of great interest due to the fact that they yield better performance than their individual components. The most efficient toughening mechanism for ceramic materials involves a phase transformation; and on that account this toughen method is referred to as transformation toughening. Although alumina can be transformation-toughened, zirconia is however the prototype material for this process [5].

¹ Babes-Bolyai University, Faculty of Physics & Institute of Interdisciplinary Research in Bio-Nano-Sciences, 400084 Cluj-Napoca, Romania

Corresponding author e-mail: viosimon@phys.ubbcluj.ro

² University of Oradea, Faculty of Medicine and Pharmacy, 410068 Oradea, Romania

³ Istanbul Technical University, Metallurgical and Materials Engineering Department, 34469 Istanbul, Turkey

Alumina-zirconia composite ceramics with high alumina content are called ZTA (zirconia-toughened alumina) ceramics. In form of dense, fully sintered materials without porosity, they are widely used mainly because of their high biocompatibility and wear resistance, especially high fracture toughness [6]. The toughening mechanism in ZTA ceramics is related to structural properties of these materials [7] conferred especially by zirconia due to its versatile structural properties.

The aim of this study is focussed on X-ray diffraction and infrared spectroscopic investigation of the structural changes determined by ZrO_2 addition to Al_2O_3 in ZTA ceramics obtained by spark plasma sintering.

EXPERIMENTAL

Monolithic $(100-x)Al_2O_3 \cdot xZrO_2$ composites with $x = 0; 10; 20$ and 30 vol% were prepared by spark plasma sintering (SPS) at temperatures between $1300^\circ C$ and $1460^\circ C$, for 300 s under a pressure of 40 MPa, respectively. Shrinkage of the specimens during SPS process was continuously monitored. Fully dense samples, with a relative density of 99% , were obtained.

X-ray diffraction analysis was carried out with a Shimadzu XRD- 6000 diffractometer, using $CuK\alpha$ radiation ($\lambda = 1.5418 \text{ \AA}$), with Ni-filter. The FTIR spectra were recorded at a resolution of 2 cm^{-1} with a Bruker Equinox 55 spectrometer, at room temperature, using the KBr disk technique.

RESULTS AND DISCUSSION

The X-ray diffraction (XRD) analysis evidences reflection lines (Fig. 1) occurring from crystallographic planes related to alpha Al_2O_3 – corundum, at $2\theta = 25.6; 35.2; 37.9; 43.4; 52.6; 57.5; 61.3; 66.4; 68.2; 76.9$ and 80.7° , and tetragonal ZrO_2 , at $2\theta = 29.9; 49.9; 59.1; 59.7$ and 62 [8-10]. Corundum is extremely hard, the second hardest mineral known, with diamond being the only harder mineral. On the other hand, corundum has a brittle behaviour, but this can be improved by dispersion of zirconia particles in a composite system. The evolution of the diffraction line intensities for both Al_2O_3 and ZrO_2 crystalline phases was followed. A progressive decrease of Al_2O_3 lines intensity accompanied by increase in intensity of ZrO_2 lines is noticed as ZrO_2 content increases from 10 to 30 vol%. The ratio between the main peaks recorded at $2\theta = 35.2$ for alumina and at $2\theta = 29.9$ for zirconia are very close to $1.1, 2.2$ and 3.3 for the sample with $x = 10, 20$ and 30 vol%, respectively, that is completely in agreement with the ZrO_2 content ($1:2:3$) of the composite samples.

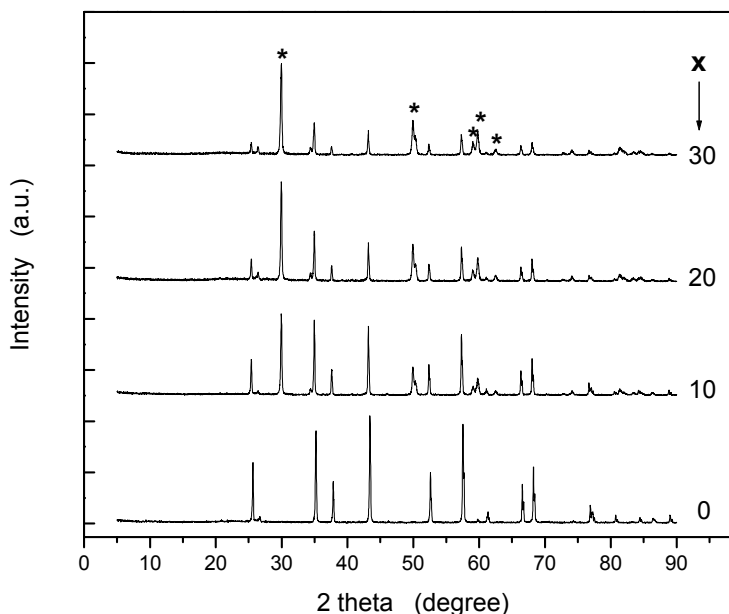


Fig. 1. XRD patterns of $(100-x)\text{Al}_2\text{O}_3 \cdot x\text{ZrO}_2$ ceramic composites (* marks ZrO_2 phase).

A different behaviour with respect to the evolution of the structural units entering these samples was observed from the analysis of the FTIR spectra between 400 and 1400 cm^{-1} (Fig. 2). For the ceramic sample containing only Al_2O_3 phase, this spectral region encompasses IR absorption bands and shoulders around 465 ; 485 ; 515 ; 560 ; 617 ; 648 ; 780 ; 797 ; 1088 and 1168 cm^{-1} , which are assigned to vibrations of Al-O bonds in AlO_n groups wherein aluminum atoms are differently coordinated, usually by four or six oxygen atoms, and less likely by five oxygens. The absorption bands and shoulders recorded in the spectral region between 465 and 650 cm^{-1} are assigned to six-coordinated aluminium which are associated with stretching modes of AlO_6 octahedra [11].

The Al-O stretching vibrations of tetrahedral AlO_4 groups are related to the broad band at 1088 cm^{-1} and shoulder at 1168 cm^{-1} , and to the doublet at 780 and 797 cm^{-1} [12-14]. In fact, for alpha alumina – corundum phase only AlO_6 units are expected [15] and, implicitly only IR absorption bands corresponding to six-coordinated aluminium atoms [RRUFF ID:R060020.1]. The presence of very large absorption bands related to tetrahedral AlO_4 groups, could suggest that during the synthesis process a part of alumina would be vitrified at grains boundaries.

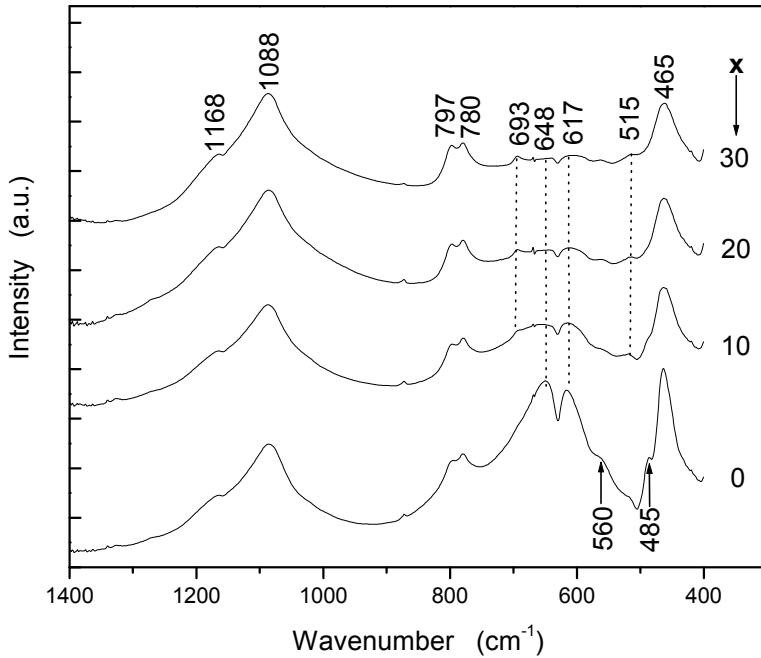


Fig. 2. FTIR spectra of $(100-x)\text{Al}_2\text{O}_3 \cdot x\text{ZrO}_2$ ceramic composites.

In earlier IR studies on zirconia are mentioned absorption bands at 410, 445, 500, 572, 740, 1104 and 1187 cm^{-1} [16]. Other authors [17] reported on FTIR bands at 740 cm^{-1} corresponding to Zr-O vibrations in monoclinic ZrO_2 , and bands at 510 cm^{-1} and 590 cm^{-1} corresponding to Zr-O vibrations in tetragonal ZrO_2 .

Anyway, the measurements carried out in this study evidenced structural reorganizations in aluminum structural units in ZTA composites. By addition of ZrO_2 , the weak absorption band at 515 cm^{-1} increases in intensity because the Zr-O vibrations in tetragonal ZrO_2 phase, evidenced by XRD analysis, contributes to this IR band [9, 18]. At the same time, the 485 cm^{-1} shoulder disappears as $x \geq 20\text{ ZrO}_2$ vol%. The most pronounced effect is observed on the 617 and 648 cm^{-1} absorption bands which nearby disappear. The sole new IR absorption band recorded from ZTA composites is at 693 cm^{-1} , and it is typical for penta-coordinated aluminium atoms [11]. The increasing content of zirconia diminishes the intensity of 465 cm^{-1} band that denotes that this band occurs from vibrations of aluminium bonds. At the same time the shoulder at 485 cm^{-1} disappears. No changes are observed with respect to Al-O stretching vibrations of tetrahedral AlO_4 groups, or if there were any, they could be compensated by the contribution introduced in the same spectral range by the vibration bands of zirconia.

As mentioned, one of the most important features that define the mechanical properties of zirconia is the change of the toughening, enabled by the fact that at ambient pressure zirconia has three polymorphs: cubic, tetragonal and monoclinic with different atomic densities [19]. The monoclinic phase has an atomic density only 96 % of that of the cubic phase and 97 % of that of the tetragonal phase, and this property makes transformation toughening possible. Several phase transformations in zirconia occur under hydrostatic pressure, and examples are given for transitions from monoclinic phase to different orthorhombic phases upon compression [19, 20]. In the case of alumina-zirconia composites investigated in this study, as a result of spark plasma sintering at high temperatures under a pressure of 40 MPa, zirconia undergoes a transition to tetragonal ZrO_2 phase.

CONCLUSIONS

The crystalline phases identified by X-ray diffraction in the investigated zirconia-toughened alumina composites are alpha Al_2O_3 (corundum) and tetragonal ZrO_2 . A linear composition dependence of the relative intensities corresponding to the two phases is noticed. The pronounced attenuation up to suppression of 617 and 648 cm^{-1} IR absorption bands recorded from pure alumina sample, caused by increasing content of zirconia in spark plasma sintered ZTA composites, is attributed to structural changes that affect bond vibrations of the six-coordinated aluminium atoms. The presence of four-coordinated aluminium atoms is assumed to be the result of a partial vitrification of alumina grain boundaries during the synthesis process. At the same time, the weak IR absorption line at 693 cm^{-1} , that is not present in the spectrum of pure alumina sample, denotes the occurrence of penta-coordinated aluminium species only in alumina-zirconia composite samples.

ACKNOWLEDGEMENT

This study was accomplished in the framework of Romanian-Turkey Bilateral Cooperation project 385/2010.

REFERENCES

1. O. Roualdes, M.-E. Duclos, D. Gutknecht, L. Frappart, J. Chevalier, D.J. Hartmann, *Biomaterials*, 31, 2043 (2010).
2. G. Pezzotti, M.C. Munisso, A.A. Porporati, K. Lessnau, *Biomaterials*, 31, 6901 (2010).
3. S.F. Yang, L.Q. Yang, Z.H. Jin, T.W. Guo, L. Wang, H. C. Liu, *Nanomed. Nanotechnol.*, 5, 232 (2009).

4. M. Guazzato, M. Albakry, L. Quach, M. V. Swain, *Biomaterials*, 25, 2153 (2004).
5. F.F. Lange, *J. Mater. Sci.*, 17, 255 (1982).
6. W. Pabst, E. Gregorova, I. Sedlarova, M. Cerny, *J. Eur. Ceram. Soc.*, (2011) article in press.
7. K. Tahmasebi, M.H. Paydar, *J. Alloy Compd.*, 509, 1192 (2011).
8. A. Taavoni-Gilan, E. Taheri-Nassaj, H. Akhondi, *J. Non-Cryst. Solids*, 355 311 (2009).
9. D. Sarkar, D. Mohapatra, S. Ray, S. Bhattacharyya, S. Adak, N. Mitra, *Ceram. Int.*, 33 1275 (2007).
10. K. Tahmasebi, M.H. Paydar, *J. Alloy Compd.*, 509, 1192 (2011).
11. S. Simon, R. Grecu, V. Simon, *Mod. Phys. Lett. B*, 16, 291 (2002).
12. M. Del Nero, C. Galindo, R. Barillon, E. Halter, B. Made, *J. Colloid. Interf. Sci.*, 342, 437 (2010).
13. S. Cavalu, V. Simon, F. Banica, C. Deleanu, *Rom. J. Biophys.*, 17, 237(2007).
14. A. Gritco, M. Moldovan, R. Grecu, V. Simon, *J. Optoelectron. Adv. Mater.*, 7, 2845 (2005).
15. S. Simon, G.J.M.P. van Moorsel, A.P.M. Kentgens, E. de Boer, *Solid State Nucl. Magn. Reson.*, 5, 163 (1995).
16. D.A. Powers, H.B. Gray, *Inorg. Chem.*, 12, 2721 (1973).
17. C.M. Philippi, K.S. Mazdiyasi, *J. Am. Ceram. Soc.*, 54, 254 (1971).
18. M. Low, R. McPherson, *J. Mater. Sci.*, 24, 892 (1989).
19. V. Milman, A. Perlov, K. Refson, S.J. Clark, J. Gavartin, B. Winkler, *J. Phys. Condens. Matter.*, 21, 485404 (2009)
20. P. Bouvier, G. Lucazeau, *J. Phys. Chem. Solids*, 61, 569 (2000).

EPR STUDY OF MOLECULAR OXYGEN EFFECT UPON NITROXIDE RADICALS

I. M. TAKACS^{1*}, M. DRAGOTA¹, CRISTINA BISCHIN²,
LAURA BOLOJAN¹ AND G. DAMIAN¹

ABSTRACT. In this paper, we have studied the effect of molecular oxygen from aqueous solution with different oxygen concentrations, on nitroxide radical Tempo (2, 2, 6, 6-tetramethyl-piperidine-1-oxyl) used in a free state and encapsulated on liposomes by EPR spectroscopy. The dependence of the EPR spectra on partial oxygen pressure, pO_2 was obtained by measuring the line width as a function of pO_2 . It was found that EPR line width of the paramagnetic probe and oxygen concentration surrounding the probe is given by a linear relation.

Keywords: EPR spectroscopy, nitroxide radicals, oxymetry, liposomes, spin label.

INTRODUCTION

In the biological systems, the amount of oxygen plays an important role in a lot of physiological and pathological processes, which are especially, associated with reactive intermediates.

Based on its nature as a gas and its physical and chemical properties; there are several analytical tools for monitoring the evolution and the consumption of molecular oxygen in biological systems. [1]. One of these techniques is represented by the study carried out through the Electron Paramagnetic Spectroscopy (EPR).

Although molecular oxygen is paramagnetic (molecular oxygen is a triplet radical that possesses two unpaired electrons, responsible for its paramagnetism), direct detection of oxygen in biological systems using EPR is not possible.

However, an indirect method exist and is based on the interaction of paramagnetic oxygen with spin probes, thus giving rise to changes of the relaxation times of these species, mainly by a mechanism due to the Heisenberg exchange

* Corresponding author e-mail: itakacs86@gmail.com

¹ Babeş-Bolyai University, Faculty of Physics, 1 Kogălniceanu str., 400084 Cluj-Napoca, Romania

² Babeş-Bolyai University, Faculty of Chemistry and Chemical Engineering, 11 Arany Janos str., 400028 Cluj-Napoca, Romania

effect [2]. This technique is usually named *EPR oxymetry*. The EPR oxymetry is based on the line broadening study of the infused spin probe EPR signal which is related to the concentration of the triplet oxygen [3].

The spin label oxymetry studies are widely used and they are quantitative studies, they present a great role in the analysis of collision rates of the molecular oxygen with the nitroxide moiety of spin labels, local oxygen diffusion and concentration studies.

In practice two classes of stable spin probes are used for EPR oxymetry: insoluble particulate materials and soluble materials. The most used insoluble spin probe is lithium phthalocyanine (LiPc), but there are a number of very fine-grained coals used as spin probes. Soluble paramagnetic oxymetry probes are especially nitroxide radicals, used in free state or encapsulated in different biological structures, for metabolic protection.

In our paper, we have studied the effect of molecular oxygen on nitroxide radical Tempo (2, 2, 6, 6-tetramethyl-piperidine-1-oxyl) used in a free state and encapsulated on liposomes, infused in aqueous solution with different oxygen concentrations.

An important attribute of phospholipids is their ability to form sphere shaped molecular structures called liposomes. Phospholipids have a molecular shape formed from a hydrophilic head and two hydrophobic tails. These phospholipids placed in a large number into a limited space will self arrange to match their heads and tails forming membranes. Under certain physical effects the phospholipid membranes will spontaneously form microscopic spheres with the size on the nanometric scale called liposomes [4]. Because of the small size, liposomes can reach to the individual targeted cells and can act as carriers for substances enclosed inside them, like nitroxide radicals, forming spin labeled liposomes.

MATERIALS AND METHODS

In this study liposomes were prepared from lecithin 5 mg/ml in a 10mM phosphate solution with 7.4 pH. The resulted emulsion was sonified for 5 minutes in ultrasound bath than mixed with the 5 mM TEMPO solution. The mixture was kept in incubation (30C) and was shaken overnight. After 20 hours of incubation the solution was centrifuged at 10krpm for 20 minutes.

To study the effect of the molecular oxygen on the line shape of the nitroxide spectrum we prepared three samples of free spin label TEMPO (2, 2, 6, 6-tetramethyl-piperidine-1-oxyl) with a concentration of 5mM in 10mM phosphate solution. We measured the first sample in low oxygen concentration by bubbling it with Ar₂ for 15 minutes until saturation; this reduced the concentration of the molecular oxygen in the solution, and then sealed the avoid contact with air and increase of oxygen concentration. The second sample was prepared in normal atmospheric condition; the solution had normal concentration of molecular oxygen.

For the third sample the solution was bubbled with O₂ for 15 minutes to reach its saturation and then sealed to avoid contact with the environment and to avoid oxygen concentration losses.

The liposomes were prepared also in a tree sample format similar to the free spin label sample. The first sample was prepared in low oxygen concentration by preparing the liposomes in phosphate tampon solution bubbled with Ar₂ for 15 minutes until saturation; this reduced the concentration of the molecular oxygen in the solution, and then sealed the avoid contact with air and increase of oxygen concentration. The second sample was prepared in normal atmospheric condition; the solution had normal concentration of molecular oxygen. For the third sample we prepare the liposomes in high concentration of molecular oxygen; the phosphate tampon solution was bubbled with O₂ for 15 minutes to reach its saturation and then sealed to avoid contact with the environment and to avoid oxygen concentration losses.

The homogenized solution was injected with a Hamilton microsyringe into a quartz capillary of about 10 cm length and an interior diameter about 1 mm. EPR measurements were performed on a Bruker EMX spectrometer operating at 9.4554 GHz with 100 kHz modulation frequency, at room temperature. The reaction mixture was transferred to a 20 µl capillary, which was then positioned in the high sensitivity (HS) cavity (Bruker Instrments, ER 4102ST). The sample was scanned using the following parameters: center field, 3360 G; sweep width, 60 G; power, 2 mW; receiver gain, 1×10³; modulation amplitude, 0.5 G; time of conversion, 30 ms; time constant, 61.4 ms; number of scans, 10.

RESULTS AND DISCUSSION

The spin label oxymetry studies and applications on biological systems have a wide range and date back a long time [5]. The spin label oxymetry study is based on the hyperfine structure changes on the EPR signal, these changes are related to the oxygen concentration in the sample. This is also why it is used to study tumor cells [6].

The oxymetry studies using nitroxide spin labels are based on EPR line broadening. These line broadenings are caused by the Heisenberg exchange between the paramagnetic molecular oxygen, having two unpaired electrons, and the nitroxide spin label with the unpaired electron on the N-O bond [2, 7].

The relationship between EPR line exchange broadening and radical-radical collision rate was defined by [8] as the following equation:

$$B = k p \omega + N \quad (1)$$

where B represents the EPR line width, k being a constant, p represents the probability of the exchange with each collision, ω the collision rate and to N is assigned the other

contributions to the line width being independent of ω . The line width changes can be written as:

$$\Delta B = k_p(\Delta\omega) \quad (2)$$

The collision rate can be given from the Smoluchowski equation

$$\omega = 4\pi R\{D(O_2) + D(SL)\}[O_2] \quad (3)$$

where R is the interaction distance, $D(O_2)$ and $D(SL)$ are the diffusion constants of O_2 , the nitroxide and $[O_2]$ is the oxygen concentration in the solution. If changes occur in the $[O_2]$ the collision rate is changed also, the collision rate changes are linearly proportional to the change of $[O_2]$:

$$\Delta\omega = 4\pi R\{D(O_2) + D(SL)\}(\Delta O_2) \quad (4)$$

From equation 4 combined with 2 we deduce

$$\Delta B = 4\pi R k_p\{D(O_2) + D(SL)\}(\Delta O_2) \quad (5)$$

From the equations above it can be seen that oxygen dependent EPR line width changes are dependent and proportional with the oxygen concentration variations in the solvent.

The oxygen concentration in solvents is influenced by the solubility of oxygen in the solvent, which can be variable up to two orders of magnitude in different solvents [9], leading us to exploit to maximum the line width changes EPR oxymetry.

The hyperfine line broadening study was done at room temperature and the obtained EPR signals are represented in the following images. The Fig.1 represents the signal of free spin label TEMPO in different solutions. The first spectrum on Fig. 1 represents the signal of TEMPO in deoxygenated solution; we measured the line width of the hyperfine structure, represented as ΔB . The obtained value for ΔB in this case was 1.20 G. The second spectrum is the signal obtained for the air saturated TEMPO, with a line width of 1.31 G. The third spectrum is the signal acquisitioned for the O_2 saturated TEMPO. The obtained value for the line width here is 1.52 G. Figure 2 represent the EPR spectra of liposomes containing the spin label TEMPO in different solutions. The first spectrum is the signal of liposomes in deoxygenated solution. The measured line width in this case is 1.25 G. The second spectrum is the signal obtained for the air saturated liposomes labeled with TEMPO. In this case the obtained value for ΔB is 1.35 G. The third spectrum is the obtained signal for the O_2 saturated liposomes. In this case we obtained a line width of 1.62 G.

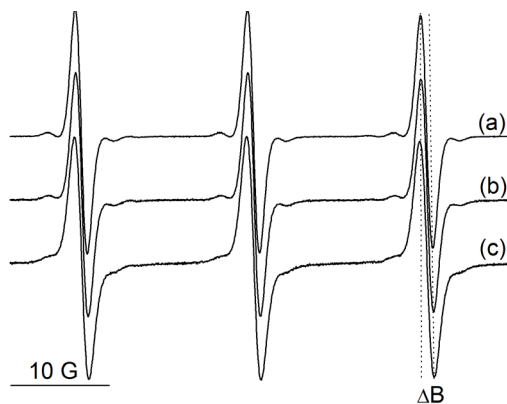


Fig. 1. EPR spectra of TEMPO

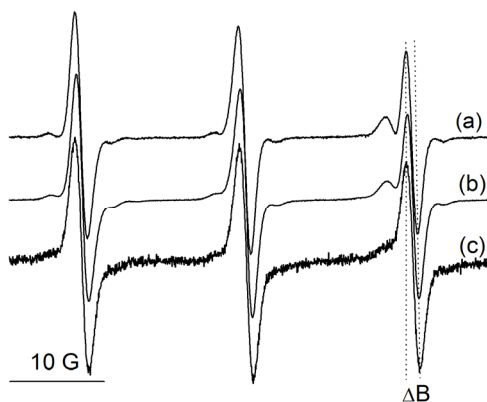


Fig. 2. EPR spectra of Liposomes labeled with TEMPO

The concentration of oxygen in the oxygen saturated samples at room temperature is $220 \mu\text{M}$. Knowing this and the line widths from the spectra we used the previously mentioned equations we calculated the oxygen concentrations in the samples. We represented the oxygen concentration variations in function of the line width changes on Fig.3.

As we mentioned before we can see the changes in the spectrum shape as well as the changes in the line width with the variation of the oxygen concentration in the solutions. By comparing the measured ΔB values for the deoxygenated and the air saturated sample we see that the oxygen concentration difference is relatively small but noticeable. But if we take a look to the line width values for the oxygen

saturated samples we can observe that there is almost a 0.2 G broadening in the spectrum compared to the air saturated samples and almost 0.3 G change compared to the Ar₂ saturated samples.

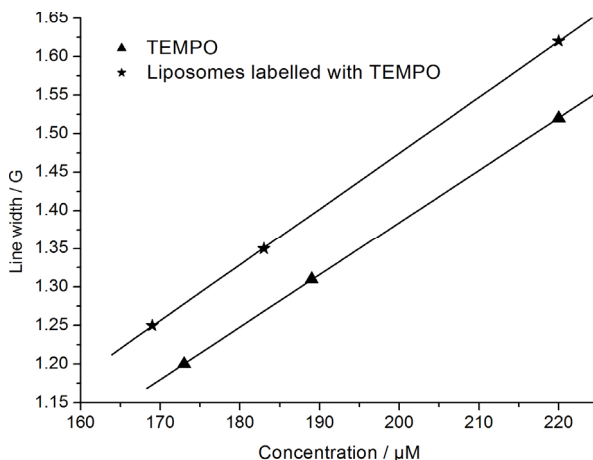


Fig. 3. Line width variation according to the oxygen concentration changes

For the line width variation of the two samples we made a linear fitting in a form of:

$$Y = A + B * x.$$

The obtained values for A in the case of TEMPO was 0.02339 with an error of 4.93E-3, respectively for B the fitting result was 0.0068 with an error of 2.5278E-5.

In the case of liposomes we obtained a value of 0.02175 with an error of 6.38E-3 for A and a value of 0.00726 with an error of 3.32607E-5 for the B .

Usually the oxygen solubility in organic solvents is higher than in non organic solvents like water [10]. This results to the line width of the dynamic range of the EPR signal to be higher which is also noticeable in our results having 0.1 G difference between the organic samples and non organic samples.

CONCLUSIONS

Our results have demonstrated that the hyperfine line width broadenings are proportional with the oxygen concentration and will influence the shape of the spectrum according to that.

The oxygen concentrations are one of the most important variables in many physiological and therapeutic processes. The combination of liposomes with spin markers leads to a greater oxygen sensitivity for in vivo EPR oxymetry.

ACKNOWLEDGMENTS

This work was possible with the financial support of the Sectoral Operational Programme for Human Resources Development 2007-2013, co-financed by the European Social Fund, under the project number POSDRU/107/1.5/S/76841 with the title „Modern Doctoral Studies: Internationalization and Interdisciplinarity”.

REFERENCES

1. G. Renger, B. Hanssum, Oxygen detection in biological systems, *Photosynth Res*, 2009, 102:487–498.
2. J.S. Hyde, W.K. Subczynski, Spin label oxymetry In Biological Magnetic resonance. Vol. 8. Spin labeling: Theory and application. L.J. Berliner and J. Reubens, editors. Plenum Press, New York, 1989, 399-425.
3. J. Seelig, I.C.P. Smith, K.W. Butler, O.H. Griffith, P.C. Jost, H.M. McConnell, In Spin labeling: Theory and Applications; L.J. Berliner, Ed. Academic Press, New York, 1976, Chapters 10-13.
4. D. Pentak, W.W. Sulkowski, A. Sulkowska, In Calorimetric and EPR Studies of the Thermotropic Phase Behavior of Phospholipid Membranes, *Journal of Thermal Analysis and Calorimetry*, Vol. 93, (2008), 2:471-477.
5. S. Pajak, K. Cieszka, R. Gurbiel, W.K. Subczynski, S.J. Lukiewicz, EPR measurements of oxygen consumption by tumor cells, Third meeting of the Polish Biophysical Society, Wroclaw-Olesnica, Book of Abstracts, p.70.
6. A. Moscatelli, T.K. Chen, S. Jockusch, M.D.E. Forbes, N.J. Turro, M.F. Ottaviani, In Oxygen Supersaturated Solutions Using Nitroxides as EPR Probe, *J. Phys. Chem. B*, (2006), 110:7574-7578.
7. W.K. Subczynski, H.M. Swartz, EPR Oximetry in Biological and Model Samples, In Biomedical EPR, Part A: Free Radicals, Metals, Medicine, and Physiology, Ed. Springer, (2006), Chapter 10.
8. G.E. Pake, T.R. Tuttle, Anomalous loss of resolution of paramagnetic resonance hyperfine structure in lipids, *Phys. Rev. Lett.*, (1959), 3:423-425.
9. K.J. Liu, M.W. Grinstaff, J. Jiang, K.S. Suslick, H.M. Swartz, W. Wang, In Vivo Measurement of Oxygen Concentration Using Sonochemically Synthesized Microspheres, *Biophysical Journal*, Vol. 67 (1994), 896-901.
10. W.F. Linke, Solubilities of Inorganic and Metal-Organic Compounds, *American Chemical Society*, (1958), Washington, DC.

OBSERVATION OF THE EFFECTS OF UV EXPOSURE OF SOME PVA MEMBRANES

L. UDRESCU¹, C. V. POP¹, T. STEFAN¹ AND M. TODICA^{1*}

ABSTRACT. The effect of UV exposure on the Poly vinyl alcohol membranes was observed by UV VIS spectroscopy. After few hours of moderate UV exposure the absorption coefficient is modified. After few weeks of relaxation, after UV irradiation was stopped, a partially recovery of the amplitude of the absorption peak is observed. This behavior suggest a reversible process of rearrangement of polymeric segments after irradiation.

Keywords: PVA, UV VIS spectroscopy, absorption properties.

INTRODUCTION

Since its discovery in 1924 the Poly vinyl alcohol (PVA) is one of the most popular polymers with applications in different domains of activity, becoming with the industry, and finishing with the medicine [1, 2, 3]. We can cite several such applications, e.g. in optics and photography it is used as a polarizing filter [4]. In medicine it is used as matrix for drug controlled release, in making artificial blood vessels, or contact lenses [5, 6]. More recently, PVA membranes doped with silver or gold nanoparticles were synthesized to produce high efficiency optical filters. Doped with semiconductors or magnetic materials PVA became an efficient support for the storage of data information. The nanoparticles doped in polymer matrices have long stability, novel optical and electrical properties [7, 8]. Recently, in combination with other polymers and different doping materials, PVA was used to achieve direct conversion fuel cells [9]. Other promising applications are based on the acoustic-optical properties effects of PVA subsystem [10]. During these applications the polymeric matrix may be deliberately or accidentally exposed to UV radiation, which can have destructive effects on the microscopic structure of the polymer. The aim of our study is the investigation of the properties of PVA membranes exposed long time to such radiations.

* E-mail: mihai.todica@phys.ubbcluj.ro

¹ "Babes-Bolyai" University, Faculty of Physics, M. Kogalniceanu No 1, 400084 Cluj-Napoca, Romania

EXPERIMENTAL

For our studies we used PVA membranes with different polymeric concentrations, 15%, 20% and 30%. In pure state PVA is a powder material with a great affinity towards the water. The polymer was mixed with distilled water, at constant temperature 25° C, during many hours, until a homogeneous dispersion of polymer is obtained. Then the gel was displayed on a glass plate and kept 24 hours in dark, at room temperature, until all the water evaporates. These samples were analyzed in their original state and after UV irradiation at different intervals of time. The UV irradiation was realized with VL 215 G lamp, at wavelength 254 nm and intensity 76 mW/cm². The UV VIS investigation was done with Jasco V-670 system with scan speed 200 nm/min, UV VIS bandwidth 2 nm, and NIR bandwidth 8 nm.

RESULTS AND DISCUSSION

Situated in the upper part of the visible spectrum of the light the UV radiations have sufficient energy to produce excitations or ionization of atoms and molecules when interact with their electronic structure. Also modification of vibrational state of the chemical bonds can occur. In a molecule, the atoms can rotate and vibrate with respect to each other. These vibrations and rotations are characterised by discrete energy levels, which can be considered as being packed on top of each electronic level [11, 12]. When an atom or molecule absorbs energy, electrons are promoted from their ground state to an excited state. The transition is possible only if the quanta energy of the photon corresponds to the energy difference between the electronic levels of the atom or molecule. The transition is possible from a bonding or non-bonding orbital into one of the empty anti-bonding orbital. In each possible case, an electron is excited from a full orbital into an empty anti-bonding orbital. The important jumps are:

from (π) or (σ) bonding orbitals to (π^*) or sigma (σ^*) anti-bonding orbitals, ($\pi \rightarrow \pi^*$), ($\sigma \rightarrow \sigma^*$), ($\pi \rightarrow \sigma^*$), ($\sigma \rightarrow \pi^*$);

from non-bonding orbitals (n) to (π^*) anti-bonding orbitals, ($n \rightarrow \pi^*$);

from non-bonding orbitals (n) to (σ^*) anti-bonding orbitals, ($n \rightarrow \sigma^*$).

Bigger jumps need more energy and so absorb light with a shorter wavelength. For example, the transitions $\sigma \rightarrow \sigma^*$ of C-H bonds in methane shows an absorbance maximum at 125 nm. Absorption maxima due to $\sigma \rightarrow \sigma^*$ transitions are not seen in typical UV-Vis. spectra (200 - 700 nm). Saturated compounds containing atoms with lone pairs (non-bonding electrons) are capable of $n \rightarrow \sigma^*$ transitions. These transitions usually need less energy than $\sigma \rightarrow \sigma^*$ transitions. They can be initiated by light whose wavelength is in the range 150 - 250 nm. The number of organic functional groups with $n \rightarrow \sigma^*$ peaks in the UV region is small. Usually the transitions of n or π

electrons to the π^* excited state are the most studied because the absorption peaks for these transitions fall in an experimentally convenient region of the spectrum (200 - 700 nm). These transitions need an unsaturated group in the molecule to provide the π electrons. That means that in order to absorb light in the region from 200 - 700 nm, the molecule must contain either π bonds or atoms with non-bonding orbitals. Theoretically the UV absorption spectrum of a given molecule should contain only well defined narrow lines, because the energy levels of the electrons are quantified. However in the majority of organic compounds the spectrum appears as a continuous broad band. This behavior is determined by the fact that rotations and vibrations in the molecule are continually changing the energies of the orbital, and as consequence the gaps between them are continually changing as well. The transition is not observed for a well defined wavelength but for a distribution of frequencies corresponding to the difference of energy between the levels affected by movement. The resulting spectrum is a combination of overlapping lines, described by a distribution function, often Gaussian or Lorentzian, with a maximum corresponding to most probable transition. The area under the graph of the function is proportional with the concentration of absorbents. Quantitative description of the absorption is given

by the Beer-Lambert law: $A = \log_{10} \frac{I_0}{I} = \varepsilon \cdot L \cdot c$ where A is the measured

absorbance, I_0 is the intensity of the incident light at a given wavelength, I is the transmitted intensity, L the path length through the sample, and c the concentration of the absorbing species. For each species and wavelength ε is a constant known as the molar absorptivity or extinction coefficient. This constant is a fundamental molecular property in a given solvent, at a particular temperature and pressure.

Usually the exposure of materials to UV radiation should not induce modifications on the molecular structure. However at high intensity of radiation modifications on the vibrational modes of molecules can occurs, having as effect the modification of the absorbance spectrum. We watched this behavior on all ours samples in function of polymeric concentration and UV time exposure. Figure 1 shows the absorption spectra for the sample with concentration 15% for different time exposure, from 1 hour to 4 hours. In the initial state, (non irradiated), the sample is characterized by a large spectrum with an important absorption peak in the domain 250-350 nm. The width of the spectrum suggests a large distribution of the energetic transitions, determined by rotation and vibration of molecules. For this sample the maximum absorption peak is observed at 282 nm. After 1 hour of UV exposure the amplitude of the peak decreases and shift slowly at 288 nm. Also the area under graphic decreases correspondingly. As the time of exposure increases, the amplitude of the peak as well as the area under graphic decrease continuously. For example, at 15% concentration the amplitude of non irradiated samples is $A_{0,15}=0.32$ a.u. This amplitude decreases continuously when the time of exposure increases, so

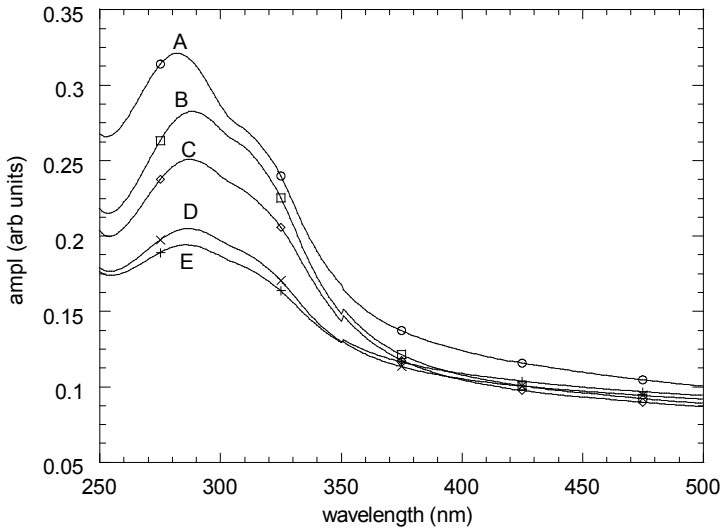


Fig. 1. The UV VIS absorption spectra for the sample with concentration 15% in initial state and after different time intervals of UV irradiation. A the sample in initial state; B after 1 hour irradiation; C after 2 hours irradiation; D after 3 hours irradiation; E after 4 hours irradiation

that after 4 hours of exposure the amplitude is $A_{4\ 15}=0.126$ a.u. The same behavior is observed for all the concentrations, but the amplitude of the maximum absorption peak, measured in the same experimental conditions, decreases when the polymeric concentration increases. For the sample with polymeric concentration 20%, the peak of non irradiated samples appears at 281 nm and its amplitude is $A_{0\ 20}=0.156$ a.u. After 4 hours of irradiation the peak shift slowly at 285 nm and its amplitude is $A_{4\ 20}=0.11$ a.u., (Fig. 2). In figures 1 and 2 we utilized the same scale for coordinate axis in order to observe this diminution of the amplitude. At 30% the peak of non irradiated sample appears at 288 nm with the amplitude $A_{0\ 30}=0.11$ a.u. and after 4 hours of irradiation its amplitude decreases at $A_{4\ 30}=0.09$ a.u. The absorption spectra for all the concentrations after 1 hour exposure are presented in figure 3. The amplitude of the absorption peaks for all the samples and for all the time exposure times are presented in figure 4.

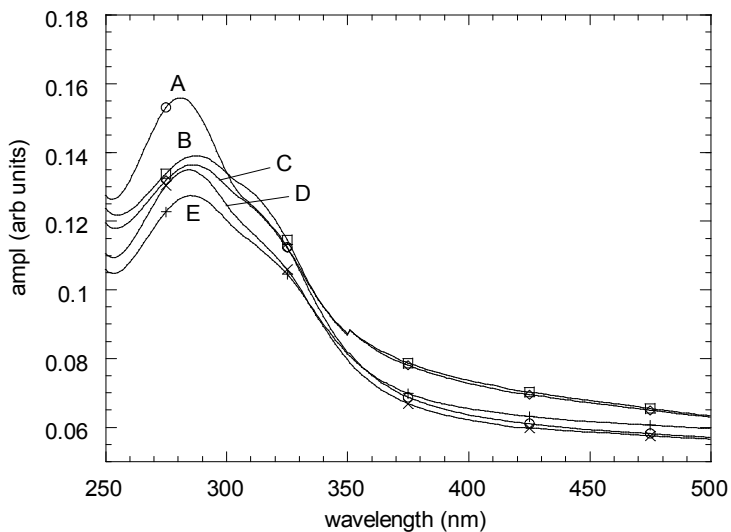


Fig. 2. The UV VIS absorption spectra for the sample with concentration 20% in initial state and after different time intervals of UV irradiation. A the sample in initial state; B after 1 hour irradiation; C after 2 hours irradiation; D after 3 hours irradiation; E after 4 hours irradiation

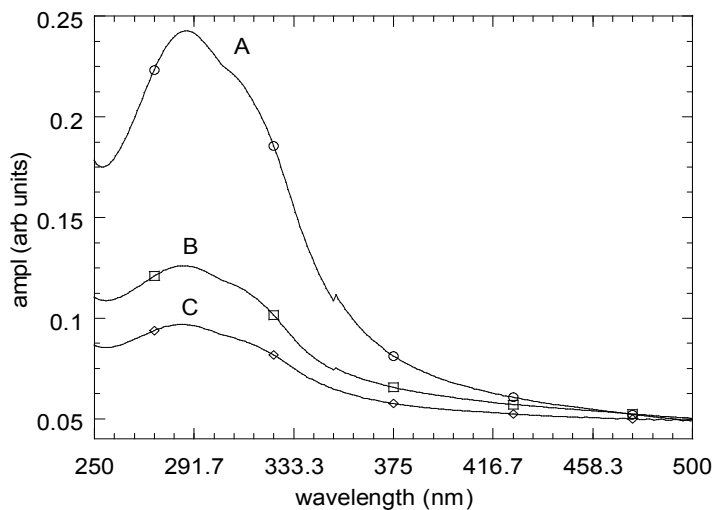


Fig. 3. The UV VIS absorption spectra for all the concentrations after 1 hour exposure. A the sample with concentration 15%; B the sample with concentration 20%; C the sample with concentration 30%

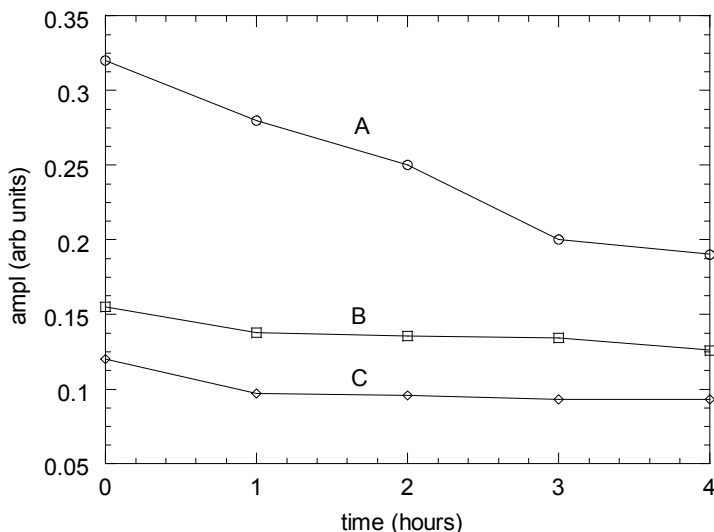


Fig. 4. Amplitude depending on UV exposure time. A the sample with concentration 15%; B the sample with concentration 20%; C the sample with concentration 30%

The smallest amplitude $A_{4\ 15}$ of sample with concentration 15% (after 4 hours of irradiation), is situated above the amplitude $A_{0\ 20}$ of the non irradiated sample 20%. Also the smaller amplitude $A_{4\ 20}$ of this sample (after 4 hours of irradiation) is greater than the amplitude $A_{0\ 30}$ of non irradiated sample 30%. This behavior suggests that long time exposure of samples with low polymeric concentration is equivalent with the increasing of polymeric concentration. The gel with low polymeric concentration is characterized by weak degree of crystallinity or local molecular order. The polymeric segments are free to move allowing a large distribution of vibrational modes of molecular bonds. The absorption of light appears in a large domain of frequencies, also in the UV region. We can explain thus the important absorption peak observed in the non exposed PVA gel with low polymeric concentration. As the polymeric concentration increases, the degree of order in the polymeric network increases, the local mobility of the polymeric segments is reduced, the polymeric network become more rigid and the distribution of vibrational modes of molecular bonds is modified. As consequent the absorption spectrum is affected. So we can explain the modification of the absorbance of the non irradiated samples when the polymeric concentration increases. It is well known that the intense irradiation of the polymeric materials with UV radiation facilitates the apparition of local order and the crystalline phase in polymeric materials [13]. The polymeric network became more rigid and the absorption spectrum

is modified compared to the initial one. We can see that UV exposure has the same effect as the increase of polymeric concentration. We can explain thus the reduction of the amplitude of the absorption peak after long time UV exposure. In the next stage of our work we investigated the behavior of absorption properties of these systems during the relaxation process. For this purpose, after the longest time of UV exposure, 4 hours, the samples were kept different time intervals, until 3 weeks, in dark at room temperature, and the UV VIS absorption spectra were recorded at different intervals of time. During the relaxation process the absorption peak is observed at the same wavelength, but its amplitude increases monotonically with the time of relaxation. This effect is shown in figure 5 for the sample with 15% concentration.

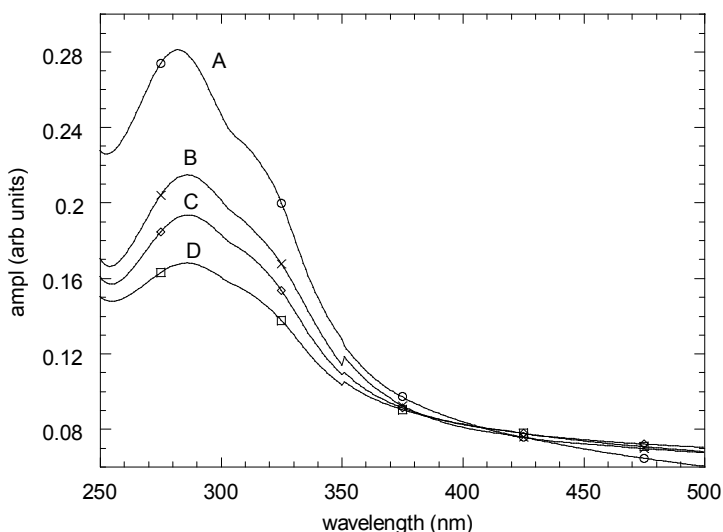


Fig. 5. Relaxation process of sample with concentration 15%. A the sample in initial state; B the sample after 4 hours irradiation UV and 4 weeks relaxation; C the sample after 4 hours irradiation UV and 3 weeks relaxation; D the sample after 4 hours irradiation UV

Similar behavior is observed for all the concentrations, but the variation of the amplitude is more important at low polymeric concentrations. The variation of the amplitude of the absorption peak during the relaxation is shown in figure 6. This behavior suggests a reversible process of the rearrangement of polymeric chains during the relaxation period. The UV irradiation, at these doses of radiation, induced an effect of local order of the polymeric segments without cross-linking. When the irradiation is stopped the segments are subject only to thermal agitation, the entropy of system increases, and the local order is destroyed. The system evolves toward their

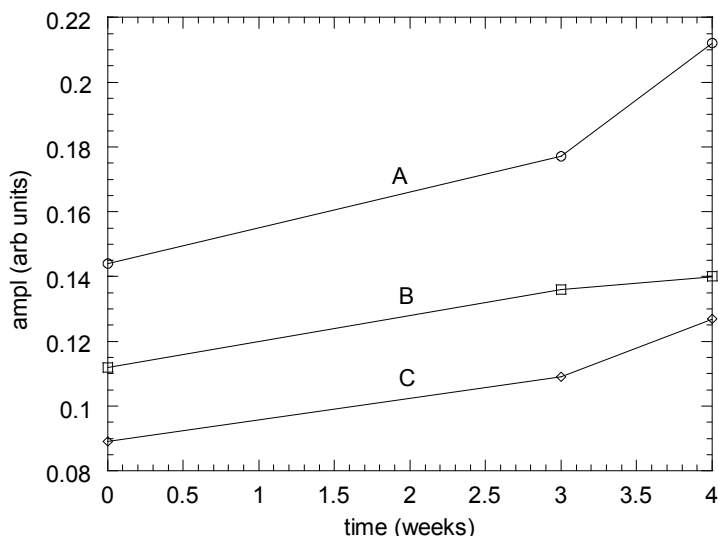


Fig. 6. Amplitude dependence of the absorption peak on the relaxation time. A the sample with concentration 15%; B the sample with concentration 20%; C the sample with concentration 30%

initial state, (as before the irradiation). This process is more important in the system with low polymeric concentrations, where the mobility of the chains is important and the rearrangement of polymeric chains is more probable [14]. Thus we can explain the important effect of relaxation on samples with low polymeric concentrations and the weak variation of the amplitude of the absorption peak at high polymeric concentrations.

CONCLUSIONS

The effect of moderate UV exposure on the absorption properties of PVA was observed by UV spectroscopy. The amplitude of the absorption peak of PVA diminishes continuously with the time of UV exposure. This effect indicates a modification of local order of polymeric chains, eventually an effect of crystallization induced by radiation. Similar effect was observed for samples with high polymeric concentration, but the variation of the amplitude of the absorption peak is less important compared with the samples with small concentration. This behavior can be correlated with the dynamics of polymeric chains, which is more reduced at high concentration. An effect of relaxation is observed for all the samples after the UV exposure is stopped. The amplitude of absorption peak increases with the duration of relaxation and the systems evolve towards its initial state before the

exposure. This effect is determined by the destruction of local order after the irradiation was stopped. This reversible process indicates no stable modification of the structure of the system at these doses of UV radiation.

ACKNOWLEDGMENTS

The author Luciana Udrescu wish to thank for the financial support provided from programs co-financed by The SECTORAL OPERATIONAL PROGRAMME HUMAN RESOURCES DEVELOPMENT, Contract **POSDRU 6/1.5/S/3** – „Doctoral studies: through science towards society”.

REFERENCES

1. D. Lopez, I.F. Cendoya, J. Torres, C. Tejada, J. Mijanagos, *Appl. Polym.*, 82, 3215 (2001).
2. M. Krumova, D. Lopez, R. Benavente, C. Mijanagos, J.M. Perea, *Polymer*, 42, 591 (2002).
3. Y. Badr, K.M. Abd El-Kader, R.M. Khafagy, *J. appli. Poly*, 92, 1984 (2004).
4. C.A. Finch, “Pol vinyl alcohol properties and applications”, Wiley, New York, **1973**, 508.
5. S. Horike, S. Matsuzawa, K. Yamaura, *J. Appl. Polymer*, 84, 117 (2002).
6. I. Kaetsu, “Drug Delivery system”, CMC, Tokyo, **1986**.
7. D.Y. Godovsky, *Adv. Polymer*, 119, 79 (1995).
8. L.L. Beecroft, C. K. Ober, *Chem. Mater*, 9, 1302 (1997).
9. C.C. Yang, *Journal of Membrane Science*, 288, 51 (2007).
10. Y. Badr, M.A. Mahmoud, *J Mater.*, 41, 3947 (2006).
11. M. Baia, S. Astilean, T. Iliescu, “Raman and SERS Investigations of Pharmaceuticals”, Berlin Springer, **2008**, p. 214, ISBN: 978-3-540-78282-7.
12. T. Iliescu, S. Pînzaru, “Spectroscopia Raman și SERS cu aplicații în biologie și medicină”, Cluj-Napoca, Casa Cărții de Știință, **2011**, p. 228, ISBN: 978-973-133-887-3.
13. Barbara Stuart, “Polymer analysis”, John Wiley and Sons, Chicester, **2002**.
14. M. Todica, “Proprietati fizice ale polimerilor”, Presa Universitara Clujeana, **2005**.

SYNTHESIS AND CHARACTERIZATION OF ZINC CONTAINING PHOSPHOSILICATE GLASS-CERAMICS

R. VERES¹, C. CIUCE², V. SIMON¹

ABSTRACT. Zinc plays an important role in bone regeneration. The addition of zinc is associated not only with the stimulation of bone formation but also with an increased biocompatibility of the host matrix. Sol-gel derived phosphosilicate glass-based materials were prepared by including different amounts of ZnO, up to 40 mol %. The structural and surface properties of the prepared samples were investigated using X-ray diffraction (XRD), thermal analysis, X-ray photoelectron spectroscopy (XPS) and Fourier transform infrared (FT-IR) spectroscopy. XRD results showed that the samples have a prevalent amorphous character. The XPS analysis pointed out that after thermal treatment the atomic concentrations on the surface of the samples are modified as a result of the structural changes accompanied by rearrangement of atomic environments. The FT-IR analysis indicated the effect of the heat treatment on the silicate and phosphate structural units.

Keywords: *sol-gel, DTA/TGA, XRD, XPS, FT-IR, bio-glass-ceramics.*

INTRODUCTION

Bioactive glasses have attracted significant attention in recent years, especially for their insertion in composite biomaterials to serve as support in tissue engineering. These biomaterials have clinical applications also as a coating for implants, bone filling, and in a porous form they are used for bone regeneration [1-5]. Synthetic scaffolds designed to regenerate bone tissue must satisfy requirements similar to the natural hard tissues, providing specific environments and architectures to promote cellular attachment, growth and differentiation.

Bioactive glasses can be obtained by melting of starting materials at high temperatures or by a low temperature process offered by sol-gel method [6]. The sol-gel route leads to high purity glasses with higher homogeneity, higher surface area and porosity, and increased bioactivity in comparison with melt-derived glasses [7].

¹ Babeş-Bolyai University, Faculty of Physics & Institute of Interdisciplinary Research in Bio-Nano-Sciences, 400084 Cluj-Napoca, Romania

² Iuliu Hatieganu University of Medicine and Pharmacy, Faculty of Medicine, 400012 Cluj-Napoca, Romania

Furthermore, bioactivity in melt-derived glasses is limited to a compositional range and SiO_2 content must be lower than 60 mol%, while a bioactive glass prepared by sol-gel method may consist of 100% SiO_2 [8].

Recently reported results on mesoporous materials in the SiO_2 - P_2O_5 binary system recommend them as promising bioglasses due to their improved biocompatible response by inducing less cellular damage than pure silica materials [9]. It has been also reported that mesoporous silica materials incorporating at least 1% P_2O_5 into the silica network exhibit an accelerated bioactive response compared to pure silica matrices [10].

Many researchers have focused their studies on preparation and characterization of bioceramic-based biomaterials incorporating ions such as Zn, Mg and Sr because of their unique effect on osteoblastic cell proliferation, differentiation and bone mineralization [11–14]. Zinc is known to reduce bone resorption and accelerate bone healing processes, by stimulating cell proliferation, as demonstrated *in vitro* and *in vivo* tests [15].

The aim of this work was to obtain and characterize the structure of a new bioglass system, SiO_2 -ZnO- P_2O_5 , that to our best knowledge was not studied as far.

EXPERIMENTAL

The new $(95-x)\text{SiO}_2 \cdot x\text{ZnO} \cdot 5\text{P}_2\text{O}_5$ bioglass system, $20 \leq x \leq 40$ mol%, with three different SiO_2/ZnO molar ratios (Table 1), was prepared following the sol-gel route.

Table 1.

Compositions and codes of investigated samples

Sample code	SiO_2 (mol %)	ZnO (mol %)	P_2O_5 (mol %)
S1-Zn	75	20	5
S2-Zn	65	30	5
S3-Zn	55	40	5

The precursors were TEOS ($\text{Si}(\text{OC}_2\text{H}_5)_4$), zinc acetate dihydrate ($\text{Zn}(\text{CH}_3\text{CO}_2)_2 \cdot 2\text{H}_2\text{O}$) and dibasic ammonium phosphate ($(\text{NH}_4)_2\text{HPO}_4$). Nitric acid (HNO_3) was used as catalyst. The precursors were separately stirred with distilled water, for 30 min. Then both zinc and phosphorous containing solutions were added to TEOS solution under continuous stirring. The obtained solution was left overnight for gelation at room temperature. After 30 days of aging at room temperature, the samples were heat treated for 24 h at 110° C.

Differential thermal analysis (DTA) and thermogravimetric analysis (TGA) were performed on Shimadzu type derivatograph DTG-60H, with a heating rate of 5°C/min using alumina open crucibles, in order to investigate the thermal behaviour of the dried samples, and to assess the heat treatment temperatures.

The structure of the samples was characterized by X-ray diffraction (XRD) analysis using X-ray Shimadzu XRD-6000 diffractometer with Ni-filter, and CuK α radiation ($\lambda = 1.5418 \text{ \AA}$). The operation voltage and current were 40 kV and 30 mA, respectively. The measurements were performed at a scan speed of 2°/min in 2 θ scan range from 10° to 80°. The average crystallite size of the 550° C treated samples were estimated based on the Scherrer equation:

$$D = \frac{k\lambda}{\beta \cos \theta}$$

where D is the crystallite size, in \AA , λ of 1.5418 \AA is the wavelength of CuK α , k is the shape factor equal to 0.9, θ – is the diffraction angle $\beta = \sqrt{B^2 - b^2}$, B – is defined as the full width at half maximum intensity, and b is the resolution function of the diffractometer (in our case 0.12 calculated for the quartz calibration sample).

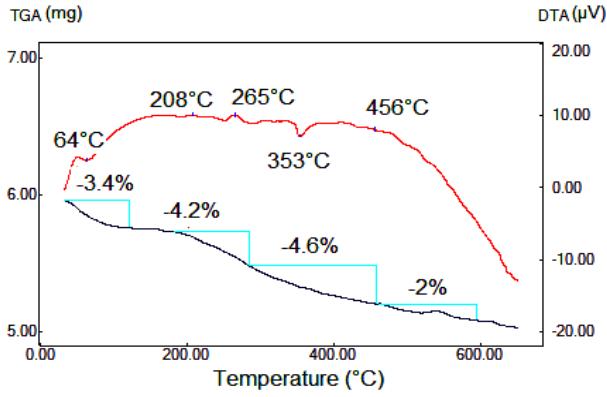
After 110 °C drying the samples were ground in an agate ball mixer mill Retsch MM300, and then they were thermal treated at 300 °C and 550 °C.

Elemental analysis on samples surface was performed with a PHI 5600ci Multi Technique system with monochromatized AlK α radiation from a 250 W X-ray source ($h\nu = 1486.6 \text{ eV}$), with pressure in the analysis chamber kept in the 10⁻⁹ mbar range.

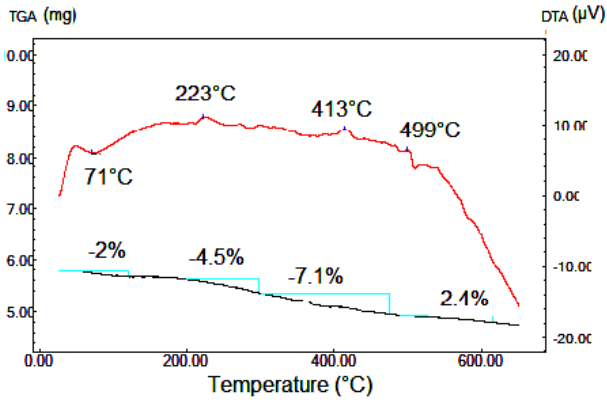
FT-IR spectra were recorded in the range of 4000-400 cm⁻¹ in transmission mode on a FT/IR-6200 Spectrometer by Jasco using the KBr pellet technique. Samples were prepared by mixing 1 mg of powder with 250 mg of KBr and pressing into pellets.

RESULTS AND DISCUSSION

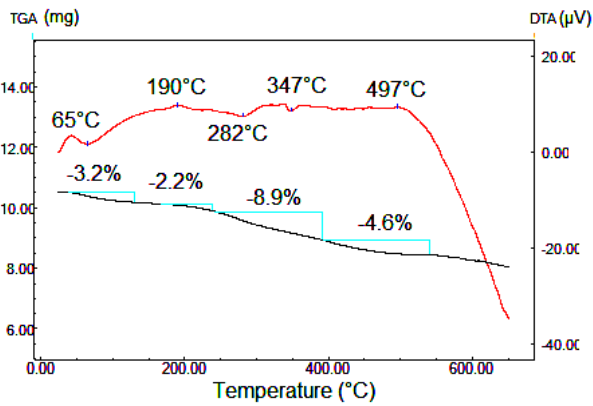
The TGA curves for all the samples present more regions of weight loss (Fig. 1). In Table 2 are presented the temperatures at which events occur. The first weight loss that occurs around 70 °C coincides with an endothermic peak in DTA signal and it can be associated with the removal of free water molecules. A second weight loss with more corresponding peaks in the DTA curve can be observed until 300 °C. This loss can be associated with the decomposition of ammonium nitrate and the elimination of water caged in the pores. Further weight losses are observed until 550 °C and correspond to the elimination of the organic residual groups from the precursors used in the samples synthesis. Thermal analysis indicates that the removal of organic residues takes place up to about 550 °C, which can be considered as thermal treatment temperature.



(a)



(b)



(c)

Fig. 1. DTA and TGA runs of sol-gel derived bioglasses: (a) S1-Zn; (b) S2-Zn; (c) S3-Zn

Table 2.

Events temperature and weight losses for glass samples

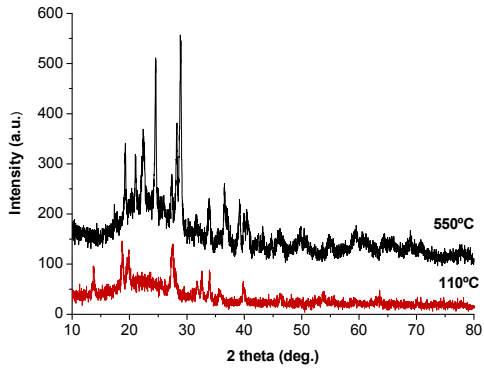
Sample code	Endothermic events temperature (°C)	Exothermic events temperature (°C)	Weight losses (%)
S1-Zn	64, 353, 456	208, 265	3.4, 6.8, 2.3
S2-Zn	71, 499	223, 413	1.9, 9.7, 3.2
S3-Zn	65, 282, 347	190, 497	3.2, 10.8, 4.6

Figure 2 shows the XRD patterns for all investigated samples. The patterns of the 110°C dried samples indicate a prevalent amorphous state in all samples. Beside the large diffraction peak that dominates the XRD patterns, there are peaks indicating the presence of minor crystalline phases, that could be assigned to hydrated zinc silicate and ammonium zinc phosphate crystals formed during the samples synthesis [16, 17]. After thermal treatment at 300 °C the peaks corresponding to ammonium zinc phosphate crystals are still present. The XRD patterns of 550 °C heat treated samples indicate beside the dominant amorphous phase nanocrystals that correspond to zinc phosphate. The crystallites size calculated with the Scherrer equation for the samples treated at 550 °C are given in Table 3.

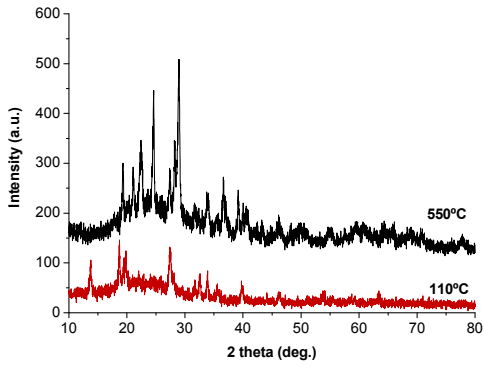
Table 3.

The size of crystallites in the samples heat treated at 550 °C

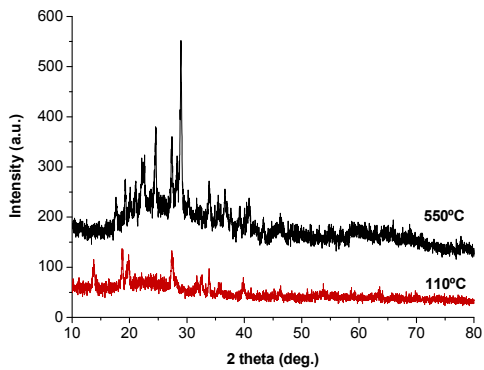
Sample code	Crystallites size (nm)
S1-Zn	30.7
S2-Zn	28.3
S3-Zn	24.8



(a)



(b)



(c)

Fig. 2. XRD patterns of (a) S1-Zn, (b) S2-Zn and (c) S3-Zn samples treated at different temperatures

The analysis of XPS survey spectra (Fig. 3) was carried out to determine the surface composition for thermal treated S1Zn sample at 110 °C and 550 °C. After thermal treatment, the changes due to relaxation of the network structure imply changes in the atoms concentration on sample surface, as shown by data summarized in Table 4. After thermal treatment at 550°C one can observe an increase of oxygen and silicon content and a decrease of carbon, zinc and phosphorus content.

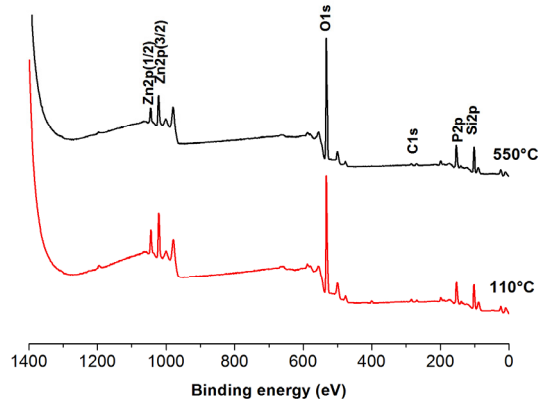


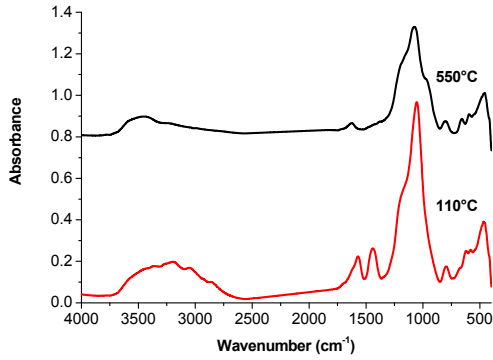
Fig. 3. XPS survey spectra of S1Zn sample

Table 4.

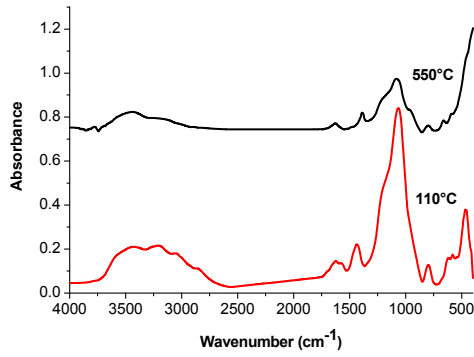
The relative atomic concentrations on surface of S1Zn heat treated samples

Sample code	Elemental composition (at %)				
	C	O	Zn	P	Si
S1Zn / 110 °C	3.7	53.8	2.6	3.9	34.4
S1Zn / 550 °C	2.8	55.3	1.8	3.2	37.0

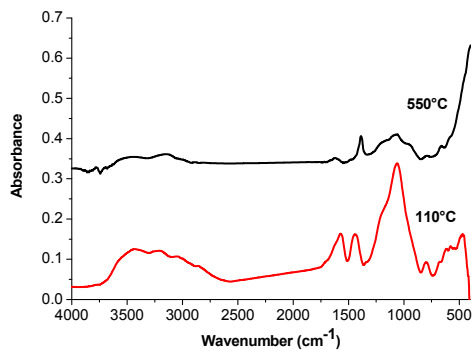
FT-IR spectra are presented in Figure 4. A broad absorption band, situated between 3750-2800 cm^{-1} is mainly due to vibrations of Si-OH bonds, molecular water and organic residues [18-22]. The peak at 3740 cm^{-1} is due to free Si-OH groups on the surface of the glass. The peak at 3540 cm^{-1} is associated to silanol groups linked to molecular water through hydrogen bonds. The large absorption band at 3500-3000 cm^{-1} is assigned to molecular water. The bands at 3000-2800 cm^{-1} correspond to the symmetric and asymmetric fundamental stretching vibration of CH_2 and CH_3 groups belonging to residues from the precursors used in the sol-gel



(a)



(b)



(c)

Fig. 4. FT-IR spectra of (a) S1-Zn, (b) S2-Zn and (c) S3-Zn samples treated at different temperatures

process. After thermal treatment the broad band from 3750-2800 cm^{-1} decreased in intensity by eliminating of water and organic residues. The peak at 1620 cm^{-1} corresponds to vibration of molecular water. The absorption band recorded around 1400 cm^{-1} is assigned to vibrations of CH bonds. An increase in the intensity of this band is observed with increase of ZnO content, and a decrease after thermal treatment. The band at 1200-1000 cm^{-1} is due to the Si-O-Si and P-O stretching mode [23, 24]. The shoulder at 953 cm^{-1} recorded from the samples treated at 550 °C corresponds to silanol species stretching vibrations [25, 26]. For both dry and heat-treated samples is noticed a decrease in intensity with increasing amount of ZnO due to lower SiO₂ content. The bands at 800 and 460 cm^{-1} are assigned to Si-O-Si bonds [27], and that at 650 cm^{-1} to Si-H wag-rocking mode [28]. The peak at 572 cm^{-1} ascribes to the absorption of Zn-O-Si vibration [29, 30] and the absorption peak around 420 cm^{-1} corresponds to bending of Zn-O [31, 32].

CONCLUSIONS

Sol-gel derived samples of the new ZnO-P₂O₅-SiO₂ glass system thermally treated at 550°C have a prevailing amorphous structure in which nano-crystallites of zinc phosphate are developed. In the glass-ceramic samples the size of the nanocrystals decreases with the increase of Zn content. After thermal treatment, not only network relaxation but also atomic composition changes take place on glass-ceramics surface. The nanostructured samples can be considered for further investigation with respect to their bioactivity required for biomaterials used as scaffolds in bone tissue regeneration.

ACKNOWLEDGMENTS

R.V. author wishes to thank for the financial support provided from programs co-financed by The Sectoral Operational Programme Human Resources Development, Contract POSDRU 88/1.5/S/56949 – „Doctoral and postdoctoral programs to support research". This study was performed in the framework of PN II project PCCE 312/2008.

REFERENCES

1. E. Verne, M. Bosetti, C. Vitale-Brovarone, C. Moisescu, M. Cannas, *Biomaterials*, 23 (2002) 3395.
2. E. Verne, R. Defilippi, G. Carl, C. Vitale-Brovarone, P. Appendino, *J. Eur. Cer. Soc.*, 23 (2003) 675.
3. C. Vitale-Brovarone, S. Di Nunzio, O. Bretcanu, E. Verne, *J. Mat. Sci. Mater. Med.*, 15 (2004) 209.
4. E. Verne, F. Valles, C. Vitale-Brovarone, S. Spriano, C. Moisescu, *J. Eur. Cer. Soc.*, 24 (2004) 2699.

5. C. Vitale-Brovarone, E. Verne, *J. Mat. Sci. Mat. Med.*, 16 (2005) 863.
6. P. Saravanapavan, J.R. Jones, S. Verrier, L.L. Hench, *Biomed. Mater. Eng.*, 14 (2004) 467.
7. L.L. Hench, *J. Mater. Sci. Mater. Med.*, 17 (2006) 967.
8. S.M. Best, A.E. Porter, E.S. Thian, G. Huang, *J. Eur. Cer. Soc.*, 28 (2008) 1319.
9. A. Garcia, M. Colilla, I. Izquierdo-Barba, M. Vallet-Regi, *Chem. Mater.*, 21 (2009) 4135.
10. M. Colilla, I. Izquierdo-Barba, M. Vallet-Regi, *Micropor. Mesopor. Mater.*, 135 (2010) 51.
11. A.Oki, B. Parveen, S. Hossain, S. Adeniji, H. Donahue. *J. Biomed. Mater. Res. A*, 69 (2004) 216.
12. A. Saboori, M. Sheikhi, F. Moztarzadeh, M. Rabiee, *Adv. Appl. Ceram.*, 108 (2009) 155.
13. A. Balamurugan, A.H. Rebelo, A.F. Lemos, J.H. Rocha, *Dent. Mater.*, 24 (2008) 1374.
14. A. Balamurugan, G. Balossier, S. Kannan, J. Michel, J.M. Ferreira, *Acta Biomater.*, 3 (2007) 255.
15. M. Yamaguchi, H. Oishi, Y. Suketa, *Biochem. Pharmacol.*, 364 (1987) 007–4012.
16. A. Ferrari, A. Braibanti, A.M.M. Lanfredi, A. Tiripicchio, *Acta Crystallogr.*, 22 (1967) 240.
17. A.A. Khan, J.P. Roux, W.J. James, *Acta Crystallogr. B*, 28 (1972) 2065.
18. G. Orcel, J. Phalippou, L.L. Hench, *J. Non-Cryst. Solids*, 88 (1986) 114.
19. R.F. Bartholomeu, B.L. Butler, H.L. Hoover, C.K. Wu, *J. Am. Ceram. Soc.*, 63 (1980) 481.
20. R.M. Almeida, G.C. Pantano, *J. Appl. Phys.*, 68 (1990) 4225.
21. R.S. McDonald, *J. Am. Ceram. Soc.*, 62 (1958) 1168.
22. D.L. Wood, E.M. Rabinovich, D.W. Johnson, J.B. Mac-Chesney, E.M. Vogel, *J. Am. Ceram. Soc.*, 66 (1983) 693.
23. M. Sitarz, M. Handke, W. Mozgawa, *Spectrochim. Acta A*, 56 (2000) 1819.
24. V. Aina, G. Malavasi, A. Fiorio Pla, L. Munaron, C. Morterra, *Acta Biomater.*, 5 (2009) 1211.
25. U. Lavrencic-Stangar, M. Puchberger, N. Husing, *Mater. Res. Soc. Symp. Proc.*, 726 (2002) 111.
26. G. Gnana Kumar, S. Senthilarasu, D.N. Lee, A.R. Kim, P. Kim, K.S. Nahm, S.-H. Lee, R.N. Elizabeth, *Synthetic Met.*, 158 (2008) 684.
27. T. Kokubo, H. Kushitani, S. Sakka, T. Kitsugi, T. Yamamuro, *J. Biomed. Mater. Res.*, 24 (1990) 721.
28. G. Scardera, E. Bellet-Amalric, D. Bellet, T. Puzzer, E. Pink, G. Conibeer, *J. Cryst. Growth*, 310 (2008) 3685.
29. A. Roy, S. Polarz, S. Rabe, B. Rellinghaus, H. Zahres, F.E. Kruijs, M. Driess, *Chem. Eur. J.*, 10 (2004) 1565.
30. M.G. Fonseca, E.C. Silva Filho, R.S.A. Machado Jr., L.N.H. Arakaki, J.G.P. Espinola, C. Airoidi, *J. Solid State Chem.*, 177 (2004) 2316.
31. S.G. Motke, S.R. Yawale, S.S. Yawl, *Bull. Mater. Sci.*, 25 (2002) 75.
32. A.M. Hofmeister, E. Keppel, A.K. Speck, *Mon. Not. R. Astron. Soc.*, 34 (2003) 16.